Washington University in St. Louis
Washington University Open Scholarship

Engineering and Applied Science Theses & Dissertations | McKelvey School of Engineering

Winter 12-15-2017

Development of in vitro Drug Screening Platforms Using Human Induced Pluripotent Stem Cell-Derived Cardiovascular Cells

Yosuke Kurokawa
Washington University in St. Louis

Follow this and additional works at: https://openscholarship.wustl.edu/eng_etds

 Part of the Biomedical Engineering and Bioengineering Commons

Recommended Citation

Kurokawa, Yosuke, "Development of in vitro Drug Screening Platforms Using Human Induced Pluripotent Stem Cell-Derived Cardiovascular Cells" (2017). *Engineering and Applied Science Theses & Dissertations*. 284.
https://openscholarship.wustl.edu/eng_etds/284

This Dissertation is brought to you for free and open access by the McKelvey School of Engineering at Washington University Open Scholarship. It has been accepted for inclusion in Engineering and Applied Science Theses & Dissertations by an authorized administrator of Washington University Open Scholarship. For more information, please contact digital@wumail.wustl.edu.

WASHINGTON UNIVERSITY IN ST. LOUIS

School of Engineering & Applied Sciences
Department of Biomedical Engineering

Dissertation Examination Committee:
Steven George, Chair
Jonathan Silva, Co-Chair
Stacey Rentschler
Lilianna Solnica-Krezel
Jessica Wagenseil

Development of *in vitro* Drug Screening Platforms Using Human Induced Pluripotent Stem Cell-Derived Cardiovascular Cells

by
Yosuke Kurokawa

A dissertation presented to
The Graduate School
of Washington University in
partial fulfillment of the
requirements for the degree
of Doctor of Philosophy

December 2017
St. Louis, Missouri

© 2017, Yosuke Kurokawa

Table of Contents

List of Figures v

List of Tables vi

Acknowledgments vii

Abstract ix

Chapter 1: Background and Motivation 1

Chapter 2: Tissue Engineering the Cardiac Microenvironment: Multicellular Microphysiological Systems for Drug Screening 4

2.1 Introduction 4

2.2 Anatomical Considerations 6

2.3 2D Models 7

2.4 3D Models 9

2.5 Co-Culture Models 12

2.5.1 Endothelial cells 12

2.5.2 Fibroblasts 16

2.5.3 Non-cardiac cells and blood 18

2.6 Concluding Remarks and Future Outlook 20

Chapter 3: Machine Learning Plus Optical Flow: A Simple and Sensitive Method to Detect Cardioactive Drugs 22

3.1 Introduction 22

3.2 Materials and Methods 24

3.2.1 Cell culture 24

3.2.2 Drug treatment 25

3.2.3 Time lapse imaging of cardiomyocyte motion 25

3.2.4 Intracellular calcium from the GCaMP6 fluorescence 26

3.2.5 Optical flow & machine learning 26

3.2.6 Statistical analysis 28

3.3 Results 29

3.3.1 Brightfield and fluorescence signal processing 29

3.3.2 Control experiments 31

3.3.3 Response to E-4031 32

3.3.4 Response to verapamil 34
3.3.5 Response to blebbistatin 35
3.4 Discussion 36
Chapter 4: Modeling Trastuzumab-Related Cardiotoxicity in vitro Using Human Stem Cell-Derived Cardiomyocytes 44
4.1 Introduction 44
4.2 Materials and Methods 46
4.2.1 Cell culture 46
4.2.2 Cardiomyocyte differentiation 46
4.2.4 Drug exposure 47
4.2.5 Lactate dehydrogenase (LDH) measurement 47
4.2.6 CM-EC co-culture 48
4.2.7 Quantitative real-time PCR 48
4.2.8 Statistical analysis 48
4.3 Results 49
4.3.1 Differentiation and isolation of iPS-CMs 49
4.3.2 Cardioprotective effects of NRG-1 49
4.3.3 Trastuzumab-related cardiotoxicity 50
4.3.4 Cardioprotective effect of HB-EGF 51
4.3.5 CM-EC co-culture platform 53
4.4 Discussion 54
Chapter 5: Human Induced Pluripotent Stem Cell-Derived Endothelial Cells for Three-Dimensional Microphysiological Systems 59
5.1 Introduction 59
5.2 Materials and Methods 61
5.2.1 Cell culture 61
5.2.2 CDH5-mCherry iPSC line 61
5.2.3 Derivation and isolation of iPS-EC 62
5.2.4 Flow cytometry 63
5.2.5 Immunofluorescent staining 63
5.2.6 Quantitative real-time PCR 64
5.2.7 Tube formation assay 64
5.2.8 Permeability assay 65

5.2.9 mCherry-VE-cadherin response to thrombin 65
5.2.10 Microfluidic device fabrication and culture 66
5.2.11 Shear stress response 66
5.2.12 Vasculogenesis device analysis 67
5.2.13 Statistical analysis 67
5.3 Results 68
5.3.1 Physiological characterization of iPS-EC 68
5.3.2 Phenotypic characterization of iPS-ECs 69
5.3.3 CDH5-mCherry iPSC line 71
5.3.4 iPS-EC response to shear stress 73
5.3.5 3D iPS-EC vascular networks 73
5.3.6 Supplementation of small molecule TGF-β inhibitor 75
5.3.7 Vessel response to anti-angiogenic drug 75
5.4 Discussion 76
Chapter 6: Challenges and Opportunities 82
6.1 Integration of Organ Systems 82
6.2 Disease Modeling 83
6.3 Patient-Specific Drug Screening 84
6.4 Conclusion 85
References 86
Appendix 109

List of Figures

Figure 2.1: The cardiac microenvironment 6

Figure 2.2: 3D cardiac tissue derived from hPSC-CM 10

Figure 2.3: The influence of non-cardiomyocytes and other factors present in the native cardiac microenvironment 13

Figure 3.1: Data acquisition and analysis for GCaMP6 and bright-field signal 30

Figure 3.2: Analysis of control experiments: longitudinal and placebo experiment 32

Figure 3.3: Analysis of E-4031 33

Figure 3.4: Analysis of verapamil 34

Figure 3.5: Analysis of blebbistatin 36

Figure 4.1: Cardioprotective effects of NRG-1 50

Figure 4.2: Cardiotoxicity of trastuzumab 51

Figure 4.3: Cardioprotective effects of HB-EGF 52

Figure 4.4: Co-culture of iPS-CM and ECFC-EC 53

Figure 5.1: Differentiation, isolation, and basic characterization of the iPS-EC 68

Figure 5.2: Phenotype characterization of iPS-EC 70

Figure 5.3: The use of CDH5-mCherry iPSC-derived EC (CDH5-iPS-EC) 72

Figure 5.4: 3D culture of iPS-EC in microfluidic devices 74

Figure 5.5: Response of iPS-EC vasculature to small molecule inhibitors 76

List of Tables

Table 3.1: Summary of the SVM accuracies calculated for the concentrations of each drug compound with the bright-field method 38

Acknowledgments

First, I would like to acknowledge my adviser Dr. Steven George for his support and mentorship throughout my Ph.D. The research contained in this dissertation was made possible by Dr. George's strong guidance, and I am thankful for how he has helped my development as a researcher.

Second, I would like to acknowledge my thesis committee members who provided new insights into my research. I would like to specifically acknowledge Dr. Jonathan Silva who has taken the co-chair position after Dr. George's departure to University of California, Davis.

Third, I would like to acknowledge all my collaborators who assisted in my research. I would like to thank Dr. Michelle Khine for her contribution in the optical flow and machine learning project. I would like to thank Dr. Bruce Conklin for generously sharing multiple human stem cell lines, including the GCaMP6 expressing iPSC line. He also gave meaningful insights into the UH2/UH3 research progress at our meetings. I would like to thank Dr. Christopher Hughes, Dr. Abraham Lee, Dr. Leslie Lock, and Christina Tu for their contribution in the UH2/UH3 project.

Fourth, I would like to acknowledge my family and friends who have supported me through my Ph.D. I am thankful for my parents and my brother who have helped my journey through graduate school. I am grateful for all the people with whom I have interacted both at University of California, Irvine, and Washington University in St. Louis; it has been a truly rewarding experience. I especially want to thank the George Lab members who have made a positive impact on my graduate school experience both in and out of the lab. I would like to thank Eugene Lee for his contribution in the optical flow and machine learning project as well as his broad support throughout my Ph.D. research.

Fifth, I would like to acknowledge Michael Shang and Rose Yin for their assistance in my research. I am very fortunate to have had two exceptional undergraduate researchers working for me, and I appreciate their help in performing various research experiments and data analysis.

Finally, I would like to acknowledge funding sources that have funded my Ph.D. studies, specifically the National Science Foundation (NSF) Integrative Graduate Education and Research Traineeship (DGE-1144901) and the American Heart Association (AHA) Predoctoral Fellowship (16PRE30480019). I would also like to acknowledge funding sources that have supported the lab, specifically the National Institutes of Health (NIH) UH2/UH3 grant (UH2/UH3-TR-000481).

Yosuke Kurokawa

Washington University in St. Louis

December 2017

ABSTRACT OF THE DISSERTATION

Development of *in vitro* Drug Screening Platforms Using Human Induced Pluripotent Stem Cell-Derived Cardiovascular Cells

by

Yosuke Kurokawa

Doctor of Philosophy in Biomedical Engineering

Washington University in St. Louis, 2017

Professor Steven George, Chair

Professor Jonathan Silva, Co-Chair

Drug-induced cardiotoxicity is a critical challenge in the development of new drugs. Since the advent of human pluripotent stem cell-derived cardiomyocytes (CMs), researchers have explored ways to utilize these cells for *in vitro* preclinical drug screening applications. One area of interest is microphysiological systems (i.e. organ-on-a-chip), which aims to create more complex *in vitro* models of human organ systems, thus improving drug response predictions. In this dissertation, we investigated novel analysis methods and model platforms for detecting drug-induced cardiotoxicity using human induced pluripotent stem cell (iPSC)-derived cardiovascular cells.

First, we utilized human iPSC-derived CMs (iPS-CMs) to establish optical methods of detecting cardioactive compounds. We utilized optical flow to assess the iPS-CM contractions captured using brightfield microscopy. The parameters were then analyzed using a machine learning algorithm to determine the accuracy of detection that can be obtained by the model for a given drug concentration. This result was compared to the analysis of the calcium transients measured using a genetically encoded calcium indicator (GCaMP6). The brightfield contraction analysis

matched the detection sensitivity of fluorescent calcium transient analysis, while also being able to detect the effects of excitation-contraction decoupler (blebbistatin), which was not detected using calcium transient analysis.

Second, we utilize iPS-CMs to model trastuzumab-related cardiotoxicity. Trastuzumab, a monoclonal antibody against ErbB2 (Her2), is used to treat $Her2^+$ breast cancer and has known clinical cardiotoxicity. We demonstrated that an active ErbB2 signaling via binding of neuregulin-1 (NRG-1) to ErbB4 is necessary to detect the cardiotoxic effects of trastuzumab. Activation of ErbB2/4 pathway via NRG-1 is cardioprotective, and we also demonstrated that heparin-binding epidermal growth factor-like growth factor (HB-EGF) similarly activates the ErbB2/4 pathway. Finally, we established a co-culture platform of iPS-CMs and endothelial cells (ECs), which recapitulated the physiological phenomenon of EC-secreted NRG-1 activating the ErbB2/4 pathway on the CMs.

Third, we demonstrated the use of human iPSC-derived ECs (iPS-ECs) for creating 3-dimensionial vascular networks inside microfluidic devices. The iPS-ECs were characterized for EC markers and physiological functions. We utilized a CDH5-mCherry iPSC line to create iPS-ECs that expressed VE-cadherin fused to mCherry. The vascular networks formed by the iPS-ECs were patent and perfusable, retaining 70 kDa dextran within the lumen of the vessels. The vasculature responded to small molecule inhibitors, showing increased vessel formation in response to TGF-β inhibitor SB431542 and decreased vessel formation in response to multi-targeted receptor tyrosine kinase inhibitor sunitinib.

Taken together, our findings advance the current understanding and utility of iPS-CMs for drug screening applications, while establishing platforms for creating microphysiological systems that

incorporate iPS-EC co-culture. The use of iPSC-derived cells opens possibilities for disease-specific and patient-specific drug screening applications in the future.

Chapter 1: Background and Motivation

The development of new drugs has played a critical role in reducing disease-related mortality and improving quality of life in the current era of modern medicine. However, a significant problem has started to disrupt the pharmaceutical industry and its ability to continue producing new drugs: the rising cost of drug development. Current estimates of drug development costs are between $1.3 to $2.6 billion for a single drug to be approved by the US Food and Drugs Administration (FDA).[1,2] While some dispute the exact costs and reasoning,[3] pharmaceutical companies have used the figure to justify high drug prices as a necessity in order to fund the research and development of future drugs.[4] The exact effects that high drug prices have on the US are difficult to gauge, but researchers agree that high drug prices have negative clinical and socioeconomic impacts and must be properly addressed.[4]

The drug development process can be broadly broken down into the preclinical and clinical phases. In most cases, the preclinical phase of drug development starts by identifying compounds of interest using a target-based approach, where a molecular target for a specific disease is preidentified.[5] This process is performed in high-throughput fashion using *in vitro* assays that test for target binding. These compounds then undergo optimization to improve sensitivity and specificity to the target. The lead compounds are then tested for safety and efficacy using appropriate *in vitro* models and *in vivo* animal models. The compound of interest then undergoes the three phases of clinical trials, where the compound must demonstrate safety and efficacy among a large patient population. Phase I clinical trial tests for safety, while Phase II and Phase III must show both safety and efficacy in the patient population in order to gain FDA approval of the new compound for public use.

There are many reasons for the rise in the cost of drug development (reviewed extensively in Scannell et al.[6]). First, an FDA-approved treatment option already exists for most prevalent diseases. For a new drug to enter the market, the drug must show improved efficacy (or equal efficacy with improved safety) over the current standard to care, which is more challenging than showing efficacy compared to the placebo control. Second, the regulatory standards for drug safety has become more rigorous, especially in areas with existing treatment options that have been deemed safe. Third, the target-based drug screening paradigm may overestimate the understanding of the disease mechanism. A drug that binds to a single molecular target may not have the predicted therapeutic effect once delivered to a human patient due to a lack of causal link between the target and the disease. An emerging theory also adds that the widespread practice of mergers and acquisitions in the pharmaceutical industry has reduced innovation due to decrease in market competition.[7]

One potential path to reducing the drug development costs is to improve the predictive power of the preclinical drug development program, especially in the area of *in vitro* models, so that drugs that enter clinical trials have a higher rate of success. The success rate of clinical trials is low, with more than 80% of Phase II clinical trials between 2009 and 2011 failing.[8] Improvements in the success rate of drugs that enter human clinical trials would dramatically reduce the cost of drug development, as clinical trials account for an estimated 57% of the total drug development costs.[1] The lack of predictive power in *in vitro* models have been long recognized, mostly attributed to the lack of physiological relevance of the *in vitro* model compared to the human body.[9] Stakeholders have taken note of this opportunity, investing research capital on methods to improve the available preclinical drug screening tools. One such funding mechanism is the National Institutes of Health (NIH) Microphysiological Systems Program which, in coordination

with the Defense Advanced Research Projects Agency (DARPA) and the FDA, aimed to develop advanced *in vitro* platforms that can be utilized for improved preclinical drug screening.[10] With this goal in mind, my dissertation focuses on the development of novel platforms and analysis tools to improve our preclinical drug screening capabilities. The research specifically focuses on using cardiomyocytes and endothelial cells derived from human induced pluripotent stem cells (iPSCs) for drug screening applications.

The dissertation contains 5 subsequent chapters. Chapter 2 reviews the current state of cardiac microphysiological systems, with an emphasis on the roles of non-myocytes in the heart and their significance in preclinical drug screening applications. Chapter 3 focuses on the use of optical methods combined with machine learning as a novel analysis tool to aid in the identification of cardioactive compounds. Chapter 4 examines the significance of neuregulin in modeling trastuzumab-related cardiotoxicity using iPSC-derived cardiomyocytes (iPS-CMs). Chapter 5 explores the use of iPSC-derived endothelial cells (iPS-ECs) in creating 3-dimensional (3D) vascularized microphysiological systems. Finally, chapter 6 concludes the dissertation by remarking on future advances that can significantly advance the current state of preclinical drug screening.

Chapter 2: Tissue Engineering the Cardiac Microenvironment: Multicellular Microphysiological Systems for Drug Screening

2.1 Introduction

The heart, like most other organs, is a complex and heterocellular system that has evolved to perform specific functions. The most critical function of the heart is to pump blood to the rest of the body, which is necessary for the transport of oxygen and nutrients to maintain viability. Dysregulation of the cardiovascular system is a major concern in modern society; while the development of new drugs and therapies have helped alleviate this problem, cardiovascular disease remains the leading cause of deaths worldwide.[11] Compounding this problem is the observation that some FDA approved drugs for cardiovascular disease as well as a host of other diseases (e.g., diabetes, inflammation) have subsequently exhibited cardiotoxic side effects, leading to the withdrawal of numerous drugs from the market.[12] New anticancer drugs are among those that have shown unexpected negative cardiac side effects, further prompting the need to improve current methods to screen drugs for possible cardiotoxicity.[13,14]

The current standard for preclinical drug screening is animal models, primarily mouse and rat models, which have failed to fully recapitulate the human heart's response to drugs. Compared to humans, mice show profound differences in beating rate (500-724 bpm compared to 60-90 bpm) as well as electrophysiological properties (e.g. electrocardiogram duration, repolarization currents, and ion channel expression levels).[15] The hERG binding assay has been developed and implemented to screen for drugs that cause hERG-mediated QT-prolongation, but this method does not address any other ion channels involved in cardiomyocyte electrophysiology and fails to capture drug-induced cardiotoxicity.[16] The inability to predict human cardiac physiological

response to drugs has contributed to higher rates of failure in clinical trials, putting patients at unnecessary risk and raising the overall cost of drug development. A potential solution to the current limitations of screening for cardiac drug toxicity is to develop *in vitro* models of human cardiac physiology, which could provide better predictive power of potential cardiac toxicity and thus improve the efficiency of drug discovery.

While intriguing, developing *in vitro* human models of cardiac function is not without significant challenges. Given the complex mechanisms involved in various pathophysiological conditions of the heart, an appropriately complex model will be necessary to study such events.[17] Nonetheless, researchers have put forth significant effort toward creating microphysiological models of the heart, focusing on creating biomimetic cardiac tissue that recapitulates some of the key electrical and mechanical properties of the heart, and thus an accurate pharmacological response. Over the past five years, significant targeted funding from the National Institutes of Health (NIH), Defense Advanced Research Projects Agency (DARPA), and the US Food and Drug Administration (FDA) has stimulated interest in engineering microphysiological systems of not only the heart, but other physiological systems (e.g., gastrointestinal tract, brain, kidney) that will also potentially improve drug efficacy and toxicity.[10]

This review will present the recent progress in creating microphysiological models of the heart, with an emphasis on drug screening applications. Starting with an overview of cardiac anatomy, we will explore tissue engineering strategies that consider the choice of cellular and extracellular components, as well as how to integrate these components temporally and spatially to recover the most important features of cardiac function. Finally, we will discuss the most significant remaining hurdles, and the future outlook for ultimate success.

2.2 Anatomical Considerations

The heart consists of several distinct anatomical units.[18] The four heart chambers and associated valves control the flow of blood in a unidirectional fashion through the heart. The spiral arrangement of ventricular cardiac muscle fibers allows coordinated force generation adequate to pump blood to the rest of the body. Action potentials are generated at the sinoatrial node, and the frequency is modulated by the nervous system. Recreating the complexities of an entire heart is currently intractable – and would likely be cost-prohibitive and unnecessary for drug screening applications. Instead, microphysiological models of the heart have targeted the myocardium, the source of electrical propagation and force generation in the ventricle, as the minimal functional unit that could model drug responses and disease states (Fig. 2.1). Cardiomyocytes comprise the largest volume of space in the myocardium, and demonstrate a highly ordered structure that

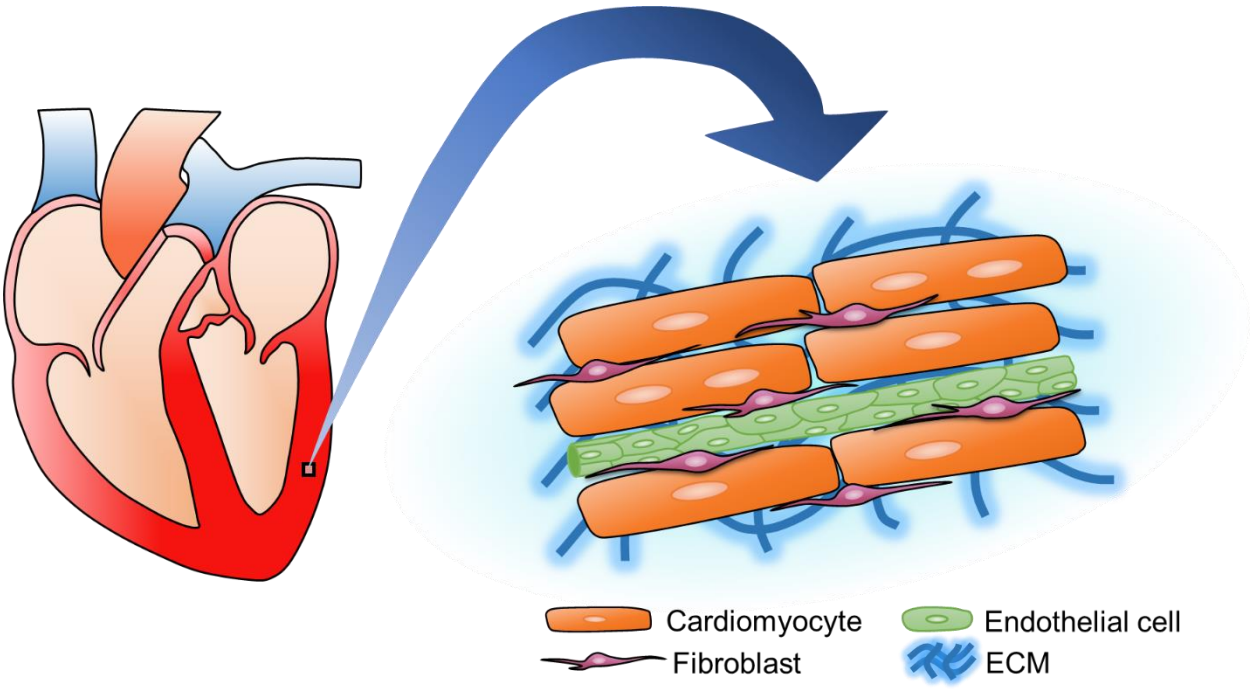

Figure 2.1: The cardiac microenvironment. Microphysiological models of the heart have focused mostly on recapitulating the structures within the myocardium. Within a single section of the myocardium (approximately 100 μm), several important cell types are present (cardiomyocytes, endothelial cells, fibroblasts) in a specific structural arrangement to actively modulate the microenvironment.

coordinates action potential propagation and force generation. Adjacent cardiomyocytes form intercalated disks, whereby intercellular junctions promote synchronous contractions via electrical coupling.[19] Connexins, and specifically connexin-43 (Cx43), are the predominant gap junction proteins found between cardiomyocytes and is often utilized as a marker of electrical coupling. The myocardium requires these coordinated electrical and mechanical activities in order to perform its function, and dysregulation can lead to pathological conditions such as re-entry ventricular arrhythmia. Single cell cardiomyocytes cannot model many of these conditions and has led to the development of more advanced models of the myocardium that better mimic physiologically relevant cardiac tissue.

2.3 2D Models

Since the advent of human pluripotent stem cell-derived cardiomyocytes (hPSC-CM), researchers have explored their potential use in drug screening.[20,21] Cardiomyocyte differentiation has significantly increased in efficiency and reproducibility within the last decade, helping to develop an accessible source of human cardiomyocytes. As the simplest model, a 2D monolayer of hPSC-CM has been used to establish the basic response to cardioactive drugs using techniques such as patch clamping,[22,23] microelectrode arrays (MEAs),[24] calcium-sensitive dyes,[25] voltage-sensitive dyes,[26] and impedance measurements.[27,28] Using induced pluripotent stem cell-derived cardiomyocytes (iPS-CM), researchers have also been able to recapitulate genetically-linked disease phenotypes such as long QT syndrome, which has created the possibility of patient-specific and disease-specific drug screening.[24,29–31] The FDA has already started to outline plans to incorporate the use of hPSC-CM for screening proarrhythmic drugs, and the use of hPSC-CM will likely be integrated as a part of the preclinical drug screening process in the near future.[32]

One of the significant drawbacks in using hPSC-CM is the immature or "fetal-like" phenotype of the cells.[33] The electrophysiological properties and force of contraction vary significantly from adult cardiomyocytes, raising questions on the validity of the drug response observed using hPSC-CM.[21,34] While a 2D monolayer of hPSC-CM expresses most of the ion channels that are of interest for drug screening,[24] hPSC-CM change ion channel expression levels and develop subcellular structures such as sarcoplasmic reticulum over long culture periods (~100 days).[35–37] The concern over hPSC-CM immaturity has further contributed to the development of microphysiological systems, as many strategies to mature hPSC-CM involve mimicking the native cardiac microenvironment, as recently reviewed.[38]

One strategy to improve 2D culture is cellular alignment. Native cardiomyocytes are rod-like in structure and strongly align in the direction of contraction.[39] Cardiomyocytes grown in 2D do not spontaneously organize in such a manner, and hPSC-CM display a disorganized, circular morphology.[35] Many techniques have been developed to induce alignment in cardiomyocytes in 2D. Micropatterned ECM causes cardiomyocytes to take on an anisotropic morphology, and increased conduction velocity in the longitudinal direction attributed to the formation of intercalated disks.[40,41] Using cardiomyocytes grown on micropatterned thin films, Grosberg et al.[42] formed strips of aligned cardiomyocytes that deformed in the direction of alignment. The deformation can then be used to calculate the stress produced during contraction. Both normal and abnormal conditions of the heart have been explored using this platform.[43–45] Topographical cues such as nanogrooves, nanofibers, or shrink-induced wrinkles also induce cardiomyocyte alignment.[46–49] Aligned cardiomyocytes have been utilized to study physiological action potential propagation and have also shown varied response to isoprenaline compared to non-aligned cardiomyocytes.[50,51] While 2D models lack many of the physiological features of the

myocardium, they offer a simple, robust, and potentially useful *in vitro* platform for drug screening and disease modeling.

2.4 3D Models

In order to more fully replicate normal physiology and anatomical structure, cells must be grown in a 3D microenvironment.[52] Advances in tissue engineering methods, particularly in the areas of synthetic biomaterials and microfabrication, have provided unprecedented opportunities to culture cells in 3D, leading to the growing interest in creating 3D microphysiological systems. The use of 3D culture has resulted in improved drug screening capabilities in many systems such as tumor and liver models.[53–57] 3D models can more accurately recapitulate physiological features of an organ system compared to 2D, and these methods have been applied to creating 3D microphysiological cardiac tissues.

Most tissue engineering approaches make use of scaffolding materials to create a 3D structure, including native ECM components and synthetic polymers. The earliest attempts to create 3D cardiac tissue employed neonatal rat cardiomyocytes and resulted in synchronously contractile constructs.[58] Lee et al.[59] used a catheter balloon to create a 3D cardiac organoid with pumping capacity. Embedding hPSC-CM into 3D constructs also results in synchronously contractile tissue, demonstrating formation of gap junctions and responsiveness to cardioactive drugs.[60] However, much like 2D monolayer cultures, these tissues lack structural organization at the mesoscopic level (Fig. 2.2), as cardiomyocytes randomly orient within the 3D matrix. Researchers have since developed several techniques using mechanical and electrical stimuli to induce structural alignment of 3D cardiac tissues.

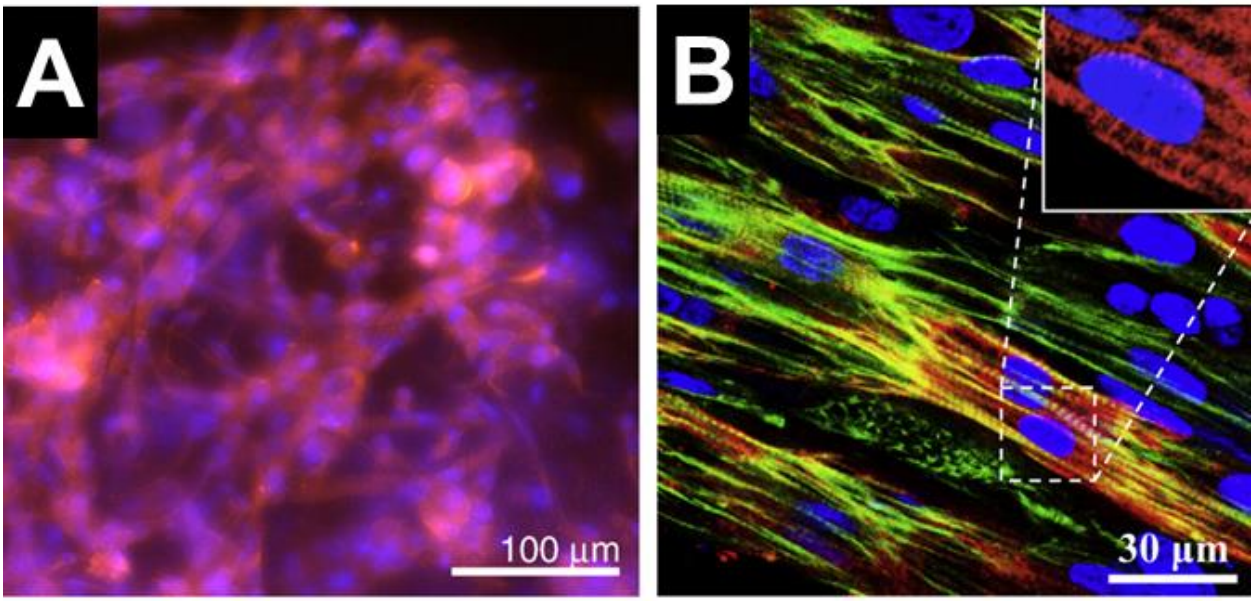

Figure 2.2: 3D cardiac tissue derived from hPSC-CM. (A) Embedding cardiomyocytes in 3D scaffolds result in disorganized structures, as the cardiomyocytes show random sarcomere orientation within the tissue (red = α-sarcomeric actin, blue = DAPI). (B) Using Velcro as an anchor along the edges, the 3D cardiac tissue displays mesoscopic organization and alignment (red = myosin heavy chain, green = sarcomeric α-actinin, blue = DAPI). Adapted and reprinted and with permission from Elsevier.[60,68]

Eschenhagen et al.[61] pioneered the use of load-bearing anchoring points to induce alignment of cardiomyocytes embedded in a gel. Velcro was used to anchor two sides of a collagen gel, and cellular compaction of the gel induced alignment of embryonic chick cardiomyocytes perpendicular to the sides. The concept of load-bearing anchors have resulted in numerous designs using various ECM compositions that have helped engineer aligned cardiac tissue that range from a few hundred microns to several millimeters.[62,63] The deflection of posts can be used to calculate contractile force, and the ease of tissue formation make these platforms amenable to high-throughput drug screening. While early works utilized animal-derived cardiomyocytes, similar structures have been created using hPSC-CM.[64–67] These cardiac tissues show advanced electrophysiological properties (e.g. increased conduction velocity, intercalated disk formation) and recapitulate many of the physiological contractile properties seen *in vivo*.[68]

Electrical stimulation has also been utilized to induce alignment of cardiomyocytes. Using electrical pulses that mimic that of the native myocardium, Radisic et al.[69] created aligned cardiac tissues that showed enhanced electrical and contractile properties. Using a platform termed the "biowire", electrical stimulation at a superphysiological rate induced advanced electrophysiological maturation in cardiac tissues derived from hPSC-CM.[70] Electrical stimulation plays a significant role in the maturation of 3D cardiac tissues, and there is growing evidence that providing electrical stimulation in combination with mechanical load or stimulation can further mature these tissues.[71,72]

Researchers have also explored the use of scaffold-free 3D culture systems. Cardiomyocyte differentiation protocols that employ embryoid bodies (EBs) result in contractile 3D constructs in suspension.[73] Due to the presence of non-myocytes in the differentiated EBs, most researchers dissect and replate the cardiomyocytes onto 2D substrates; however, recent efforts have focused on recreating cardiomyocyte spheroids that can be grown in suspension, making use of techniques such as forced aggregation and hanging-drop culture.[74,75] These scaffold-free systems lack structural organization, but offer a synchronous, cell-dense tissue with the expected response to adrenergic receptor agonists. These small aggregates can also be used as building blocks to efficiently create larger scale tissues, which can potentially reduce the time of culture necessary to form syncytium compared to enzymatically disaggregated cardiomyocytes.[66,76] While these tissues initially lack cellular alignment, load-bearing anchors can be utilized to create aligned, synchronous cardiac tissues. Singularized cardiomyocytes also self-aggregate in suspension to form a cell-dense cardiac tissue. Mathur et al.[77] recently reported the formation of organized cardiac tissue by loading single-cell hPSC-CM in a microfabricated device, which demonstrated a physiological response to cardioactive drugs.

2.5 Co-Culture Models

While researchers have succeeded in constructing cardiac tissues with advanced physiological form and function, most of the work has used an incompletely-defined population of cells obtained through cardiomyocyte differentiation. As cardiomyocyte differentiation efficiency increases and new purification techniques develop, future studies may have the opportunity to use a pure population of hPSC-CM.[78–80] Interestingly, a pure population of cardiomyocytes is not necessarily the desired starting point. Many other cell types exist within the heart, are abundant in number, and play key roles in the physiological function of the myocardium.[81] Early studies have shown that the presence of non-cardiomyocytes help mature hPSC-CM compared to a pure cardiomyocyte population.[82] The inclusion of more than one cell type complicates the methodology, but should result in more physiologically relevant models, making co-culture systems a critical part of developing microphysiological models.[83] While many functions of non-cardiomyocytes in the heart have been elucidated *in vivo,* the role of co-culture systems in creating physiologically relevant cardiac tissues remains largely unexplored. This section will describe some of the early efforts in creating co-culture models of the heart, and explore the significance of non-myocytes in microphysiological systems of the myocardium for drug screening (summarized in Fig. 2.3).

2.5.1 Endothelial cells

Endothelial cells serve many critical functions in the heart. For example, endothelial cells line the interior surfaces of the myocardium (the endocardium) and blood vessels, providing a barrier function that controls communication between the myocardium and blood.[18] A high density capillary network also exists in the myocardium to meet the large metabolic requirements of the contracting myocardium resulting in a very intimate association between cardiomyocytes and

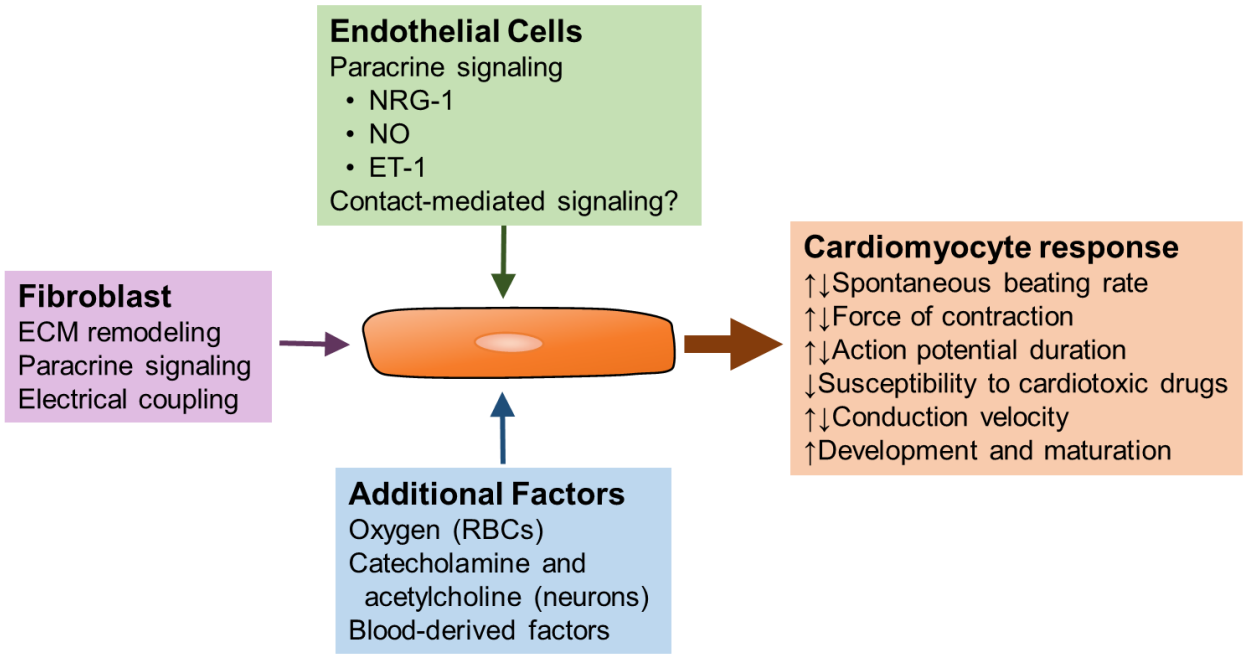

Figure 2.3: The influence of non-cardiomyocytes and other factors present in the native cardiac microenvironment. Using various modes of communication, cardiomyocyte functions are strongly affected by the presence of endothelial cells, fibroblasts, and other cells and secreted factors. Many of the responses that the cardiomyocytes undergo in the presence of these signals are closely tied to parameters that are commonly used as a readout for detecting cardiotoxic effect, highlighting the significance of a complex microphysiological model for capturing a more physiological response to drugs.

endothelial cells. In fact, every cardiomyocyte is no more than 2-3 µm from a microvascular endothelial cell.[84,85]

In addition to their barrier function, endothelial cells extensively communicate with cardiomyocytes in both developing and adult hearts.[86] Many modes of interaction between endothelial cells and cardiomyocytes have been discovered to play critical roles in cardiomyocyte contractility and survival, and may be critical in developing microphysiological systems that model cardiomyocyte response to drugs *in vitro*. Neuregulin-1 (NRG-1) is one of several growth factors produced by cardiac endothelial cells.[87] NRG-1 binds to the epidermal growth factor receptor (EGFR) family of receptors, one of which is ErbB4, expressed by ventricular cardiomyocytes. The binding of NRG-1 to ErbB4 and the signaling cascade through

heterodimerization of ErbB4 with ErbB2 is essential for early cardiac development, as knocking out NRG-1, ErbB4, or ErbB2 in mice models results in developmental failure at embryonic day 10.5 with heart malformation.[88–90] NRG-1 signaling has also been shown to improve differentiation of hPSC towards a atrial/ventricular cardiomyocyte rather than a nodal cell, which is generally desirable for recapitulating the myocardium.[91] A recent study has also shown that the addition of NRG-1β peptides induce maturation of mouse iPS-CM.[92]

The development of the drug trastuzumab (Herceptin®), a monoclonal antibody against human ErbB2, helped formulate our understanding and clinical relevance of NRG-1 signaling. Trastuzumab was developed as a chemotherapeutic drug that works by blocking ErbB2, which is overexpressed in some tumor types (e.g. breast cancer), and showed improved efficacy when combined with other chemotherapeutics such as anthracyclines (e.g., doxorubicin).[93] Due to the cardiotoxic nature of anthracyclines, combinatory chemotherapeutic treatment using trastuzumab raised serious concerns regarding the off-target effects of blocking the NRG-1/ErbB signaling in the heart.[94] It was soon discovered that blocking ErbB2 in rat cardiomyocytes significantly increased myofilament injury and contractile dysfunction caused by doxorubicin treatment.[95] Many researchers have since confirmed the critical role of NRG-1/ErbB signaling in the adult heart, including functions of growth, survival, proliferation, and repair of cardiomyocytes in both homeostatic and maladaptive conditions.[96–98]

Human stem cell-derived cardiomyocytes express ErbB receptors, and the addition of NRG-1 influences the response to doxorubicin exposure as measured by cardiomyocyte impedance and intracellular ATP.[99] While the mechanism behind upregulation and downregulation of NRG-1 varies with different physiological and pathophysiological models, NRG-1 signaling from

microvascular endothelial cells in the heart plays a critical role in cardiomyocyte response to drug-induced cardiomyopathy.[87,100]

Several other paracrine factors are known to modulate cardiomyocyte function.[84,86] Nitric oxide (NO) released by endothelial cells not only controls vascular tone of blood vessels, but also induces positive inotropic effects on cardiomyocytes.[101] Importantly, endothelial-derived NO has been shown to cause a change in cardiomyocyte contractile response to β-adrenergic stimulation, signifying its importance in drug screening applications.[102] NRG-1 signaling on cardiomyocytes upregulates NO synthesis, further influencing cardiomyocyte contractility in the presence of endothelial cells.[103] Finally, endothelin-1 (ET-1) is another positive inotrope released by endothelial cells.[104] ET-1 also increases release of NO and NRG-1 from endothelial cells, demonstrating the complex mechanisms involved in regulating cardiomyocyte functions.[105,106]

Most efforts surrounding endothelial-cardiomyocyte co-culture have centered on the goals of creating vascularized cardiac tissue for cell therapy in repairing damaged myocardium.[67,107,108] Transwells have been widely used to study the paracrine effects of endothelial-cardiomyocyte co-culture; however, such systems are mostly limited to 2D monolayers. Additionally, Transwells only capture the paracrine effects of the cells, while evidence exists that contact-mediated signaling may be important for endothelial-cardiomyocyte communication.[109] Using 3D scaffolds that are used in tissue engineering applications, future microphysiological systems will look to scale down these tissues while maintaining the key effects of endothelial-cardiomyocyte co-culture. Co-culturing hPSC-CM with endothelial cells and mesenchymal stem cells improved the contractility and cardiac ion channel expression of the 3D cardiac tissue.[110] Scaffold-free vascularized cardiac tissue can be created, but requires a tri-culture with stromal cells in order to prevent endothelial cell death.[111] Recent work by Vollert et al.[112] successfully

introduced an endothelial-coated channel through a 3D cardiac tissue. Endothelial co-culture has proven to be valuable in other microphysiological organ systems,[113,114] and we believe the same will hold true for cardiac tissues.

The source and phenotype of the endothelial cells used in culture may also play an important role in their function, as endothelial cells differ in function between different organs, but also within different parts of the heart (e.g. microvascular, endocardial, aortic).[115] For example, aortic endothelial cells do not express NRG-1 and thus may result in a poor *in vitro* model when predicting drug-induced cardiotoxicity.[106] While human neonatal and adult endothelial cell sources are readily available, the use of stem cell-derived endothelial cells is also a viable option given the differentiation protocols that have been recently developed.[116,117] Further characterization may be necessary to assess the functional phenotypes of endothelial cells in the context of the cardiac microenvironment.

2.5.2 Fibroblasts

Fibroblasts are commonly defined as mesenchymal cells that have an elongated morphology and lack a basement membrane.[118] While the exact numbers vary by species, cardiac fibroblasts make up a significant portion of adult mammalian hearts in terms of total number of cells (45 to 70%), exceeding in number that of cardiomyocytes.[118–121] Present throughout the heart, fibroblasts occupy the connective tissue space between cardiomyocytes.[121,122] Cardiac fibroblasts play several key roles in cardiac development and physiology, including ECM remodeling, paracrine signaling, mechanosensing, and electrical coupling.

Cardiac fibroblasts regulate ECM synthesis and degradation, which has been shown to be critical for cardiomyocyte function. The cardiac ECM composition changes throughout development,

and further changes in the ECM can be induced in many pathological conditions, as recently reviewed.[123] Collagens provide tensile strength within the heart, and is critical for hypertrophic growth in the neonatal heart.[124] Cardiac fibroblasts also produce periostin, which is highly expressed in the developing heart, and has been shown to induce cardiomyocyte proliferation *in vitro* and *in vivo.*[125] Fibronectin, fibrillin, elastin, proteoglycans, and glycoproteins are also present in the cardiac ECM, deposited mainly by cardiac fibroblasts.[126,127] Fibroblasts also secrete matrix metalloproteinases (MMPs) in order to remodel the cardiac ECM. The balance between ECM proteins and MMPs is critical for ECM homeostasis, which can be affected by external factors such as mechanical stimulation.[118,128] A number of pathological conditions such as myocardial infarction and pressure overload induce cardiac fibroblasts to undergo a phenotypic change into myofibroblasts, increasing proliferation and deposition of collagen via a TGFβ mediated pathway.[120,126]

Cardiac fibroblasts also directly couple with cardiomyocytes, utilizing connexins to allow propagation of electrical signals.[129] Fibroblasts are able to electrically couple cardiomyocytes separated by up to 300 μm in distance *in vitro*, although there is considerable debate on the extent of electrical coupling that occurs *in vivo* between fibroblasts and cardiomyocytes.[130,131] Fibroblast-cardiomyocyte coupling significantly alters electrophysiological properties of cardiomyocytes, affecting conduction speed, resting membrane potential, repolarization, and excitability.[132] The large number of cardiac fibroblasts in the SA node suggests that they also modulate the function of nodal cells. In contrast, fibroblast-cardiomyocyte coupling in the myocardium may be more pathological, and has been shown to induce abnormal depolarization and reentry *in vitro.*[133,134] Further studies must be performed to elucidate the exact role of fibroblast-cardiomyocyte coupling *in vivo*, such that this function can be recapitulated *in vitro*.

The role of including cardiac fibroblasts in cardiac microphysiological systems remains unclear. Co-culture of cardiomyocytes with mouse-derived cardiac fibroblasts improved the contractility of engineered cardiac tissues.[135] Adding cardiomyocytes to pre-cultured, adherent fibroblasts and endothelial cells results in improved cardiac tissue formation with elongated morphology and increased electrical coupling via Cx43 expression.[136,137] Studies have reported a population of vimentin-positive cells that are dispersed in the periphery of 3D cardiac tissues created using hPSC-CM, indicating that these fibroblast-like cells play a role in the formation of these tissues.[64,138] While increasing numbers of fibroblasts reduced electrophysiological maturation of cardiac tissues, complete removal of non-myocytes led to decreased cell spreading and gel compaction in 3D cardiac tissues.[139] A recent study showed that adding 25% CD90+ cells to hPSC-CM resulted in improved cardiac tissue formation and increased cardiomyocyte maturation compared to cardiomyocyte only control.[140]

One of the challenges in using fibroblast co-culture models is the heterogeneity of fibroblasts within the body, showing significant variation in function even within a single organ system.[127,131,141] Most researchers have used fibroblast sources that are not of cardiac origin, which may be a concern for recapitulating the physiological microenvironment of the heart. Identifying fibroblasts also poses a challenge; while anti-vimentin antibodies have been widely used to label fibroblasts, endothelial cells also stain positively for such antibodies.[142] Discoidin domain receptor 2 (DDR2) has been established as a fibroblast marker, and may be useful for future studies that incorporate cardiac fibroblasts in co-culture models.[121]

2.5.3 Non-cardiac cells and blood

Red blood cells (RBCs) account for the majority of cells present in blood, serving as oxygen carriers to help deliver oxygen throughout the body. For tissue culture *in vitro*, most systems rely

on diffusion of nutrients, including oxygen, using static exposure to cell culture medium. Due to the low solubility of oxygen in medium lacking oxygen carriers, oxygen depletion is a serious concern in microphysiological systems that employ 3D cardiac tissue, and may contribute to abnormal tissue function.[52] Perfusion of medium containing oxygen-carriers such as perfluorocarbon can improve contractility of cardiac tissues cultured *in vitro.*[143] Simple perfusion of media also increases cell survival within 3D cardiac tissues compared to static controls.[112,144] Implementation of other strategies to increase oxygen delivery such as vascularization may be necessary to create and maintain cell-dense cardiac tissues.[145,146] Nonetheless, it remains to be seen whether implementation of such strategies are necessary for microphysiological systems, whose size is at or near the limit of diffusion (~200-250 μm). The inclusion of vascular networks may enable physiological delivery of drugs through blood vessels, which may facilitate our understanding of pharmacokinetics (e.g. how readily drugs diffuse out of blood vessels) as well as potential drug interaction with the endothelial lining of the vessel.

The choice of medium is significant, especially for co-culture systems where different cell types require different nutrients and growth factors. While RPMI 1640 supplemented with B-27 is commonly used to differentiate and maintain hPSC-CM, it is a very simple medium that may lack important signaling molecules found in blood. The addition of serum in the media may result in a more physiological media; however, the content of serum is undefined with inherent batch to batch variability, and exposure to serum-containing media can alter hPSC-CM phenotype and drug response to adrenergic receptor agonists.[147] The determination of media composition that promotes physiological behavior of cardiomyocytes grown *in vitro* will be an essential step in improving the applicability of cardiac microphysiological systems for drug screening.

Finally, no co-culture model has successfully incorporated neuronal cells, which release catecholamines and acetylcholine that directly regulate cardiomyocyte function.[148,149] The ventricles have high sympathetic innervation, and the release of catecholamines (e.g. epinephrine, norepinephrine) result in positive inotropic and chronotropic effects.[150] While the physiological functions of these secreted factors in the heart are established, their significance in creating cardiac microphysiological models remain unclear. Beauchamp et al.[75] reported a decrease in beating rate of cardiomyocyte spheroids over 30 days, while long-term stimulation using phenylephrine (α-adrenergic receptor agonist) resulted in sustained beating rate over the same period of time. Supplementation of phenylephrine and/or angiotensin-II have also been shown to induce hypertrophic growth of cardiomyocytes both in 2D and 3D.[151,152] Many other factors found in blood may also improve tissue formation and maturation *in vitro.*[153,154] For example, the thyroid hormone tri-iodo-L-thyronine (T3) has been shown to induce maturation of hPSC-CM [155–157].

2.6 Concluding Remarks and Future Outlook

Cardiac microphysiological models have made significant advancements over the last decade. Through the use of hPSC-CM, we are closer to using human *in vitro* models of the heart as a tool to augment drug screening assays. While it is not yet feasible to move away from animal models, microphysiological systems offer a complementary platform to further improve detection of drug-induced cardiotoxicity using human-derived cells. Many of the current models are amenable to high-throughput screening and may soon be an integral part of the preclinical drug screening process. The use of iPS-CM from patients who have genetic cardiac disorders can also be utilized to recapitulate and develop treatment options for specific disease phenotypes. While 2D platforms are efficient and robust, technical difficulties, reproducibility, and physiological

relevance are remaining challenges for the adaptation of 3D platforms for drug screening applications. Without a method to standardize and compare drug responses across different drug screening models, it is difficult to determine which platforms are the most relevant. Widely-applicable functional readouts will need to be developed for validating drug responses obtained using these microphysiological models.

Advances in tissue engineering have been critical in the development of cardiac microphysiological systems. Using various strategies to control the cellular and extracellular components of the tissue, researchers have successfully created relatively mature and functional models of the myocardium. There is also an increasing interest in utilizing organogenesis strategies to recreate the *in vivo* microenvironment, relying on pluripotent cells to self-assemble and reconstruct both the structure and function of the organ or organ parts.[158] With the emergence of cardiac progenitor cells that can differentiate into various cell types that make up the heart, it may be feasible to form cardiac organoids that recapitulate many of the features found in the myocardium or even the whole heart. As more advanced microphysiological models of the heart become a reality, the predictive power of these models in drug screening as well as disease modeling applications will continue to develop.

Chapter Authors

Yosuke Kurokawa, Steven C. George

Final publication is available through Elsevier, http://dx.doi.org/10.1016/j.addr.2015.07.004

Chapter 3: Machine Learning Plus Optical Flow: A Simple and Sensitive Method to Detect Cardioactive Drugs

3.1 Introduction

The current state of drug development is costly and inefficient: only 1 out of 5,000 compounds available at the drug discovery stage will achieve Food & Drug Administration (FDA) approval, and the process takes approximately 14 years at a cost of 1.5 billion U.S. dollars.[159] A significant portion of this cost is attributed to withdrawal of drugs in clinical phases or post-FDA approval, 30% of which is from cardiotoxicity.[160] For example, the diuretic drug Cisapride's undetected cardiotoxic effects resulted in 175 deaths and 386 cases of serious ventricular arrhythmia before it was removed from the market in 2000.[161]

Clearly current preclinical screening methods do not adequately detect cardiotoxicity. The advent of human induced pluripotent stem cell-derived cardiomyocytes (iPS-CMs) creates the possibility of a better *in vitro* model of the human myocardium for various applications including drug screening.[29,162,163] While current protocols result in iPS-CMs that are immature,[33] they do express several important phenotypic characteristics including key contractile and channel proteins.[23] However, a persistent challenge for developing a high-throughput drug screening platform using iPS-CMs is the need for a simple and reliable method to measure key electrophysiological and contractile properties.

Invasive methods, such as patch clamping, are traditionally limited to single cell analysis, and have proven difficult for high-throughput applications. Attempts to incorporate patch-clamping into high-throughput and commercial use are limited by cell membrane quality.[164] In addition, the instability of the seals prevents extended or longitudinal studies.[165,166] Fluorescence-based

optical methods such as voltage and calcium sensitive dyes provide non-invasive means to observe electrophysiological properties of iPS-CMs.[167] However, these dyes can impact cell function, and therefore are not suitable for prolonged studies. Furthermore, both dyes and genetically encoded indicators are subject to photobleaching effects.[168,169] Microelectrode arrays (MEA) have high-throughput capabilities, but require a cluster of CMs for accurate electrical signals.[24,170] Similarly, impedance-based measurements offer non-invasive, high-throughput methods of drug screening, but are limited to monolayer cell cultures.[171,172]

Therefore, there remains a need to develop a high-throughput, sensitive, yet non-invasive detection platform for iPS-CMs. We have previously demonstrated a platform that utilizes brightfield images of iPS-CMs to measure drug effects on cardiac behavior (e.g. the positive chronotropic effects of isoprenaline)[51] Optical flow analysis is performed on the images to generate vectors representative of cardiomyocyte motion. This inexpensive and non-invasive imaging method requires only the use of a brightfield microscope and camera, and is thus applicable to longitudinal studies in cell clusters, monolayers, and individual cells. To enhance this methodology, our current study pairs the brightfield optical flow method with a computational analysis method: supervised machine learning. Machine learning can evaluate multiple parameters simultaneously without *a priori* knowledge; therefore, it can discover unexpected relationships to potentially yield better detection. Furthermore, machine learning provides a singular quantitative index that summarizes the impact of multiple parameters, and thus simplifies the assessment of drug effects on cardiomyocytes. We hypothesize that combining machine learning with optical flow detection will produce an automated, high-throughput methodology that is more sensitive than fluorescence-based detection schemes to capture drug-induced effects on human iPS-CMs.

To test our hypothesis, we evaluated the iPS-CMs response to three cardioactive drug compounds with distinct, dissimilar effects: E-4031 (hERG K^+ channel inhibitor), verapamil (L-type Ca^+ channel blocker), and blebbistatin (myosin-II inhibitor). The concentration range for each drug was selected based on the demonstrated window of cardioactive effects in previous studies.[170] To the best of our knowledge, we report for the first time the integration of optical flow with machine learning on iPS-CMs to detect drug induced cardioactive effects, and demonstrate superior performance to fluorescence-based methods.

3.2 Materials and Methods

3.2.1 Cell culture

A human iPS cell line constitutively expressing the calcium sensitive fluorescent protein GCaMP6 (WTC11-AAV-CAG-GCaMP6) was obtained from Dr. Bruce Conklin (Gladstone Institute of Cardiovascular Research). The cells were grown on 6-well plates coated with Matrigel (Corning) in mTeSR1 (Stem Cell Technologies) with daily media replacement. The cells were passaged at 80% confluence using StemPro Accutase (Life Technologies) and seeded on Matrigel-coated plates in mTeSR1 containing 10 μM Y-27632 (Tocris), a Rho-associated protein kinase (ROCK) inhibitor. A small molecule Wnt modulatory protocol was used for cardiomyocyte differentiation.[173] In brief, the cells were seeded onto Matrigel-coated 12-well plates at 100,000 cells/well, and the cells are grown for 3 days prior to differentiation. On Day 0, the media was switched to RPMI 1640 (Life Technologies) and B-27 supplement without insulin (RPMI/B-27-Ins, Life Technologies) containing 12 μM CHIR99021 (Selleckchem), a glycogen synthase kinase 3 (GSK3) inhibitor. On Day 1, the media was replaced by RPMI/B-27-Ins. On Day 3, the media was replaced by RPMI/B-27-Ins containing 5 μM IWP2 (Tocris), a Wnt signaling inhibitor. On Day 5, the media was replaced by RPMI/B-27-Ins. On Day 7, the media

was replaced by RPMI/B-27 followed by media replacement every 3 days. Spontaneously contracting cells were observed between Day 10 to 13. After 20 days post-differentiation, cardiomyocytes were purified using lactate selection.[79] In brief, the cells are washed three times using DPBS (Life Technologies), and the media was replaced by glucose-free DMEM (Life Technologies) containing 4 mM lactic acid (Sigma-Aldrich) and 25 mM HEPES (Life Technologies). The media was replaced every 2 days for 8 days, with gentle shaking to dislodge dead cells.

3.2.2 Drug treatment

Cardiomyocytes were passaged by incubating in collagenase II (Life Technologies) for 1 hour followed by TrypLE Select (Life Technologies) for 4 minutes. The cells were counted and seeded as a dense monolayer on Matrigel-coated 8-chamber Lab-Tek II Chamber Slides (Electron Microscopy Sciences) at 150,000 cells/well. The drugs E-4031, verapamil, and blebbistatin (Sigma-Aldrich) were delivered in RPMI/B-27 at various concentrations known to have cardioactive effects.[170] Prior to exposure to drug compounds, three baseline measurements were made at time points 0, 30, and 60 minutes. Drugs were serially added to the wells, waiting 20 minutes after addition before taking measurement. RPMI/B-27 was used as placebo. The drug studies were performed on cardiomyocytes at 40+ days post-differentiation.

3.2.3 Time lapse imaging of cardiomyocyte motion

Images of contracting cardiomyocytes were acquired with an Olympus IX83 (Olympus) inverted scope equipped with an ORCA-R2 color charge-coupled (Hamamatsu) camera and MetaMorph software (Molecular Devices). To control for temperature and pH, an incubation system (model ZILCS) consisting of a stage top incubator, temperature controller, and gas flowmeter (Tokai

Hit) was used with 5% CO_2. Both fluorescent and bright-field acquisitions were taken for approximately 17.5 seconds at 15.6 fps at a resolution of 672 x 512 or at 8.6 fps at a resolution of 1392 x 1040 (subsequently downsized to a resolution of 672 x 512 via bilinear interpolation) and saved as a TIFF stack. A script in MetaMorph was created to acquire the fluorescent image automatically after the bright-field acquisition was completed. To address variation among cell populations within the same sample, stage locations were recorded prior to any acquisitions to ensure that the same cells among a sample were imaged.

3.2.4 Intracellular calcium from the GCaMP6 fluorescence

The TIFF stacks were imported to ImageJ (NIH), where a 240 by 240 pixels region of interest (ROI) were selected for each stack. The average intensity value within the ROI for each frame was measured and imported into MATLAB (MathWorks). An automated code was written to identify the start and the peak of each contraction. An *n*-th order (*n*=2-10) polynomial fit was used to normalize the decay of signal due to photobleaching. The data was used to calculate the beating rate, peak amplitude, and CTD_{90}. From this, the ratio of the CTD_{90} and the amplitude was calculated, and defined as the shape ratio (SR_{90}). The SR_{90} is relatively insensitive to photobleaching (both numerator and denominator impacted equally), and was thus used to correct for photobleaching of signal over time.

3.2.5 Optical flow & machine learning

Bright-field images were processed with an optical flow algorithm, as previously described, to generate matrices of x- and y-directional vectors that represent cardiomyocyte motion, both magnitude and direction.[51,174] Using a custom MATLAB script, principal component analysis (PCA) was used to summarize the magnitude and directionality of the vectors into a single

variable. When this single variable is plotted over time, a contractile profile is generated. These contractile profiles have distinct peaks that represent the contraction and relaxation. With the contractile profiles, the user is prompted to identify the start of the first contraction for each recording. By doing so, peaks with positive principal component analysis (PCA) values are identified as the contraction phase and those with negative PCA values as the relaxation phase of the cardiomyocyte beating motion. The software then calculates 12 parameters that describe the overall shape of the contractile profiles (e.g. duration of the contraction phase) (Fig. A1.1). The frequency parameter is defined as the inverse of the time (seconds) between the peak of the contraction phase for a given beat and that of a subsequent beat. Based on this definition, the frequency parameter cannot be calculated for the last beat acquired. Therefore any other calculated parameters associated with the last beat are removed from the machine learning portion.

Each of the cardiomyocyte contractions was then regarded as an individual sample for the machine learning (ML) analysis. Support vector machine (SVM), a classifying ML algorithm, was implemented to discern between normal and abnormal cardiomyocyte contractile profiles. As most biological data do not have linear trends, a non-linear kernel, radial basis function, was chosen for SVM. The classification between the contractions of the baseline measurements and those of a given drug concentration was accomplished by randomly separating the data into a training set and a test set. The data in the test set was withheld from the training process and only used to evaluate the model. The two sets were formed by first randomly grouping one third of the wells and the corresponding contractions of that drug condition into the test set. To ensure that the test set has equal number of baseline and drug samples, the baseline measurements for one ninth of the wells were randomly allocated for the test set. The reason is that the number of

baseline measurements for each well outnumbered each drug condition of that corresponding well three to one. The rest of the wells and respective contractions were used as the training set. Within the training set, a 5-fold cross validation was performed to optimize the parameters for the generated SVM model. The optimized SVM model was then used to classify the test set. The SVM accuracy of the model was calculated by the ratio of correct classifications to the total classifications for the test set. To account for potential sampling bias, this process was performed 50 times and the reported SVM accuracy was the average of all the runs. With this process repeating numerous times and having random allocation each time for the test and training sets, the size of each respective set varied from run to run. For the baseline measurements, each well had approximately 9 contractions per video acquisition. With these numbers of contractions, the training set used for the SVM classifier had at least 200 samples.

3.2.6 Statistical analysis

Statistical significance of GCaMP6 data was determined with a one-way repeated measure ANOVA. A key assumption made in repeated measures ANOVA is the condition of sphericity, the variance of the differences among all possible pairs of a group is equal. Sphericity was determined using Maulchy's Test for Sphericity (p-value < 0.05). If the assumption of sphericity was not correct, the Greenhouse-Geisser correction was used to adjust the reported p-values for the one-way repeated measures ANOVA. If a significant p-value (p-value < 0.05) was obtained from the Repeated-Measures ANOVA, we proceeded with Dunnett's test to determine which concentration differed from our baseline measurements. Differences with p-values less than 0.05 were considered statistically significant. All reported values are in the format of mean±S.E.M. All reported sample sizes (n) refer to independent wells of chamber slides (biological replicates).

3.3 Results

3.3.1 Brightfield and fluorescence signal processing

For the brightfield analysis, optical flow was used to generate motion vectors representing iPS-CM contractions (Fig. 3.1A). Using principal component analysis (PCA), we summarized these motion vectors into a contractile profile that contains distinct peaks that represent the contraction (positive PCA values) and relaxation (negative PCA values) as seen in Fig. 3.1B.

For this study, we chose Support Vector Machine (SVM) as the machine learning algorithm. In SVM, a machine is trained with data to create an optimal model with generalizability. SVM classifies the data points into two groups (e.g. normal and abnormal cardiomyocyte behavior) by creating a decision boundary that separates the two groups. The model is evaluated by classifying unseen or withheld data. This evaluation yields an accuracy value (SVM accuracy) that reflects the effectiveness of the model. The percentage accuracy represents the ability to identify an effect (e.g. 98% represents out of 100 samples, the machine can correctly classify 98 of the instances). In the absence of cardioactive compounds, we would expect the accuracy of the machine learning to be random and therefore generate a SVM accuracy of approximately 50%. Implementation of SVM is described in detail in the Methods.

As a fluorescence-based method, we utilized an iPS cell line transduced with a genetically encoded fluorescent calcium indicator, GCaMP6 (Fig. 3.1C). This method is similar to those found in industry for the high-throughput screening of drug-induced cardiotoxicity.[20–22] In this study, the raw GCaMP6 signal acquired over time shows a rapid decay due to photobleaching (Fig. 3.1D). The photobleaching artifact was eliminated by fitting a polynomial curve to the baseline of the signal, defined as the starting point of the calcium transient, and then normalizing

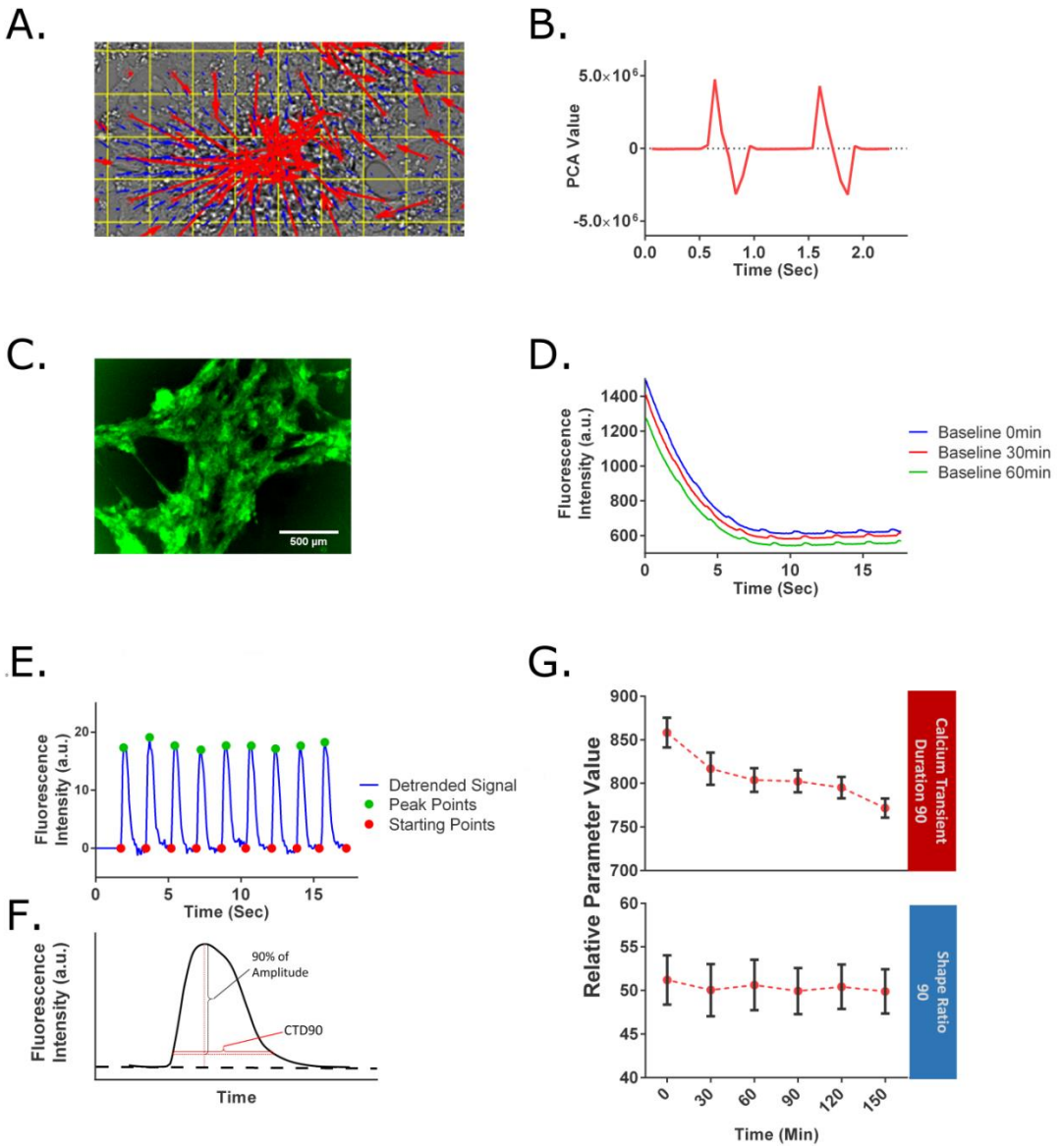

Figure 3.1: Data acquisition and analysis for GCaMP6 and bright-field signal. (A) For the bright-field method, images are processed by an optical flow algorithm to generate vectors that represent the motion of the iPS-CMs. The blue vector arrows represent the average motion of 20 x 20 pixel regions, while the red vector arrows represent 50 x 50 pixel regions. The convergence of the vector arrows toward a center visually represents an iPS-CM cluster in the contraction phase. (B) Based on the vectors, a contractile profile is derived from the 1st PCA of the norm of the x- and y-vectors. Positive PCA values indicate contraction phase, while negative values signify the relaxation values. (C) GFP signal produced by the contraction of cardiomyocytes derived from GCaMP6 iPS cells. (D) GCaMP6 signal recorded over time for 3 sequential acquisitions at baseline. The signals show a rapid photobleaching effect within the first 5 seconds, but also show a photobleaching effect between the different acquisitions. (E) The starting points and peaks of the calcium transients are identified using the detrended GCaMP6 signal. (F) A graphical explanation of CTD_{90}. The SR_{90} is defined as the ratio of CTD_{90} to the amplitude of a given calcium transient. (G) A longitudinal experiment shows an artificial decrease in CTD_{90} due to photobleaching. This is corrected by normalizing by the amplitude in SR_{90}.

the raw signal by the baseline value (Fig. 3.1E). In addition, the starting points were normalized to zero using linear interpolation. From these data, we calculated the beating rate and the calcium transient duration 90% (CTD_{90}), defined as the duration of the fluorescent signal that was 90% below the peak amplitude of the transient (Fig. 3.1F). CTD_{90} is described in detail in the Methods.

In addition to the rapid photobleaching over a single acquisition time frame, we noted that the GCaMP6 signal also experienced a smaller photobleaching effect over multiple acquisitions (Fig. 3.1G). This loss of signal intensity caused artificial decreases in CTD_{90}; this was corrected by normalizing CTD_{90} with the amplitude of the calcium transient signal. This corrected value is referred to as the Shape Ratio 90 (SR_{90}), and serves as one of the two parameters analyzed for the GCaMP6 method (Fig. 3.1G). This effect was independent of time between acquisitions (Fig. A1.2).

3.3.2 Control experiments

To ensure that the experimental setup (i.e. stage top incubator), time, and other external factors do not significantly impact the behavior of iPS-CMs, a longitudinal experiment was performed. iPS-CMs were recorded with both the CGaMP6 method and brightfield method for a total of 150 minutes at intervals of 30 minutes. In the analysis of the GCaMP6 signals, there were no changes in the beating rate and SR_{90} (Fig. A1.3), indicating stability in the iPS-CM behavior during the length of the experiment. For the brightfield method, the SVM classification was performed by grouping the first three measurements (0, 30 and 60 minutes) as the baseline control in a similar fashion to the GCaMP6 analysis. The baseline control was then compared to the 90, 120 and 150 minute time points. Corresponding SVM accuracies of 48.64±1.51, 48.22±1.57, and 49.67±1.41% were calculated (Fig. 3.2A), which are consistent with no longitudinal effect.

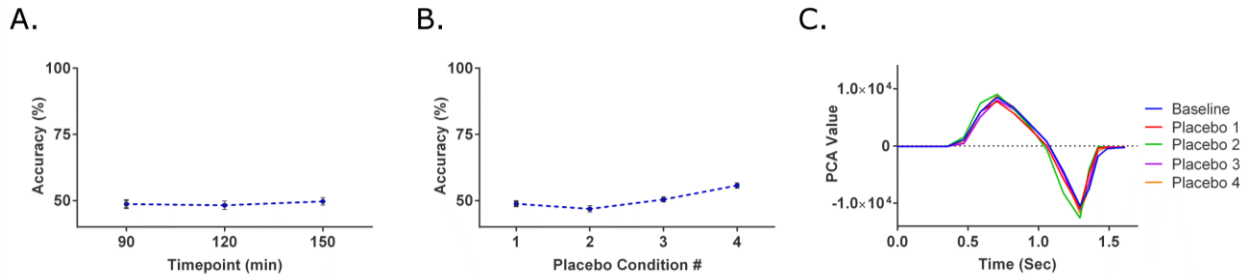

Figure 3.2: Analysis of control experiments: longitudinal and placebo experiment. (A) In the longitudinal experiment, behavior of iPS-CMs was monitored for an extended period of 150 minutes at 30 minute intervals after baseline measurements. When the machine was tasked of classifying between the first and last half of the timepoints, the SVM accuracies were approximately 50% as expected (n = 13). (B) To ensure the drug delivery process had no effects on iPS-CMs, at each placebo condition, 10 μL of media was added to the previous tested condition. The average SVM accuracy of all four placebo conditions was 50.42%, similar to that of the longitudinal experiments (n= 18). (C) Representative traces of the contractile profile from the bright-field analysis show no differences among tested conditions.

The purpose of the placebo experiment was to evaluate the drug delivery process and serve as the vehicle controls. In each placebo condition, 10 μL of RPMI/B-27 media, the vehicle for drug treatment, was added to the iPS-CMs, for a total of four placebo deliveries. Analysis with the GCaMP6 method indicated no change in beating rate and SR_{90} values when compared to the three baseline measurements taken prior to the placebo treatments (Fig. A1.4). In the brightfield method, the SVM accuracies were 48.75±1.01, 46.86±1.19, 50.40±0.98, and 55.67±1.03% respectively for each of the placebo treatments (Fig. 3.2B), again consistent with no effect. Thus, the drug delivery process had no significant impact on the behavior of iPS-CMs.

3.3.3 Response to E-4031

E-4031 is a known antiarrhythmic drug that blocks the human Ether-à-go-go-Related (hERG) K^+ channel and subsequently prolongs the QT interval.[23,24] The drug compound was administered to the iPS-CMs at an increasing concentration of 1, 3, 5, 10 and 30 nM. E-4031 induces QT prolongation, which was clearly seen in the contractile profiles generated from the brightfield images (Fig. 3.3A). At the 10 nM condition, extension of the relaxation phase was seen,

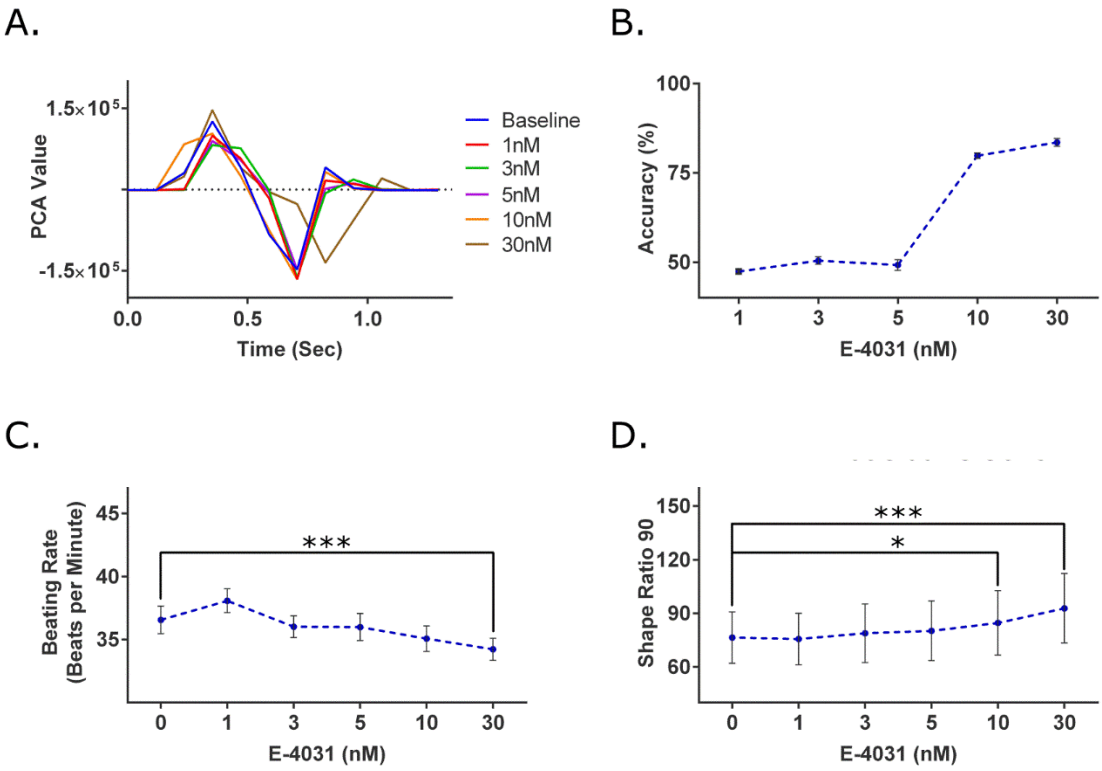

Figure 3.3: Analysis of E-4031, a hERG K^+ channel blocker known to prolong the QT interval. (A) Representative traces of the contractile profile from the bright-field analysis show a pronounced contraction elongation at the highest tested concentration (30 nM). (B) At the concentrations of 1, 3, and 5 nM, the SVM accuracies were approximately 50%, similar to those of the control experiments. For the 10 and 30 nM concentrations, the SVM accuracies increased to 79.82 $\pm$ 0.77% and 83.55 $\pm$ 1.08% respectively. This increase among accuracies suggest the compound had a cardio-modulating effect on the cells at those given concentrations (n = 15). (C) Using the GCaMP6 method, significant changes in the beating rate were seen at the 30 nM concentration ($p = 0.0175$). (D) For the SR_{90} parameter, significant differences were detected at the 10 and 30 nM concentration ($p = 0.0355$ and $p \leq 10^{-4}$ respectively) (n = 15). * $p \leq 0.05$, *** $p \leq 0.001$

consistent with the inhibition of the hERG K^+ channel that contributes to the rapid repolarization of the cardiomyocytes. The lengthening of the relaxation phase became more evident and dramatic at the next treatment level, 30 nM.

For the brightfield method, the SVM accuracies for concentration levels of 1 nM, 3 nM, and 5 nM (47.38±0.64, 50.45±1.05, and 49.19±1.49%) were similar to the baseline SVM accuracies (48.84%) (Fig. 3.3B). At the 10 nM concentration, the SVM was able to attain an accuracy of 79.82±0.77%. The SVM accuracy continued to increase to 83.55±1.08% at 30 nM concentration.

For the GCaMP6 method, a change in beating rate was detected only at 30 nM with a 6.38% decrease (Fig. 3.3C). The SR_{90} increased by 10.73% and 21.51% for 10 nM and 30 nM respectively (Fig. 3.3D), which were statistically different from baseline.

3.3.4 Response to verapamil

Verapamil is an L-type Ca^{2+} channel blocker that is used therapeutically to treat cardiac arrhythmia.[25,26] The drug compound was administered at increasing concentrations of 1, 10, 50, and 100 nM. Verapamil causes QT shortening,[27] which was consistent with the observed decrease in the duration of the contractile profile, first seen at 10 nM(Fig. 3.4A). At 50 and 100

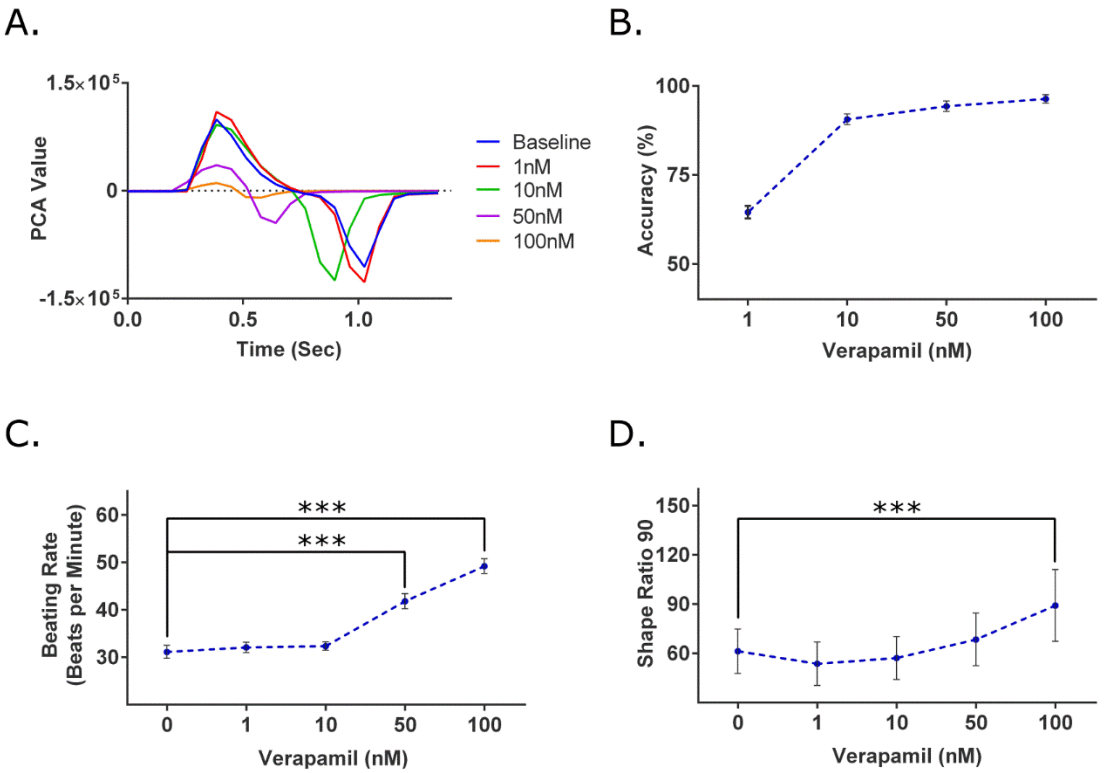

Figure 3.4: Analysis of verapamil, L-type Ca^{2+} channel blocker known to shorten QT duration. (A) Representative traces of the contractile profile from the bright-field analysis show the QT shortening effect begin at 10 nM and the negative inotropic effect at 50 nM. (B) At 1 nM, the SVM accuracy was 64.52 $\pm$ 1.78%. At the 10, 50, and 100 nM concentrations, the SVM accuracies were all above 90%, strongly indicating verapamil's cardio-modulating effect. (n = 14). (C) In the GCaMP6 method, significant changes were detected at the 50 and 100 nM concentrations ($p \leq 10^{-4}$ and $p \leq 10^{-4}$). (D) Looking at SR_{90}, significant differences were only detected at the 100 nM ($p = 8.78 \times 10^{-4}$) (n = 14). *** $p \leq 0.001$

nM, the shortening effect became more pronounced. In addition, the amplitude of the contractile profiles significantly decreased, indicating a negative inotropic effect due to decreased levels of intracellular calcium. In the brightfield method, the 1 nM concentration level had a SVM accuracy value of 64.52±1.78% (Fig. 3.4B). At the 10 nM level, the generated SVM models generated were able to achieve a SVM accuracy value that exceeded 90% (90.64±1.49%). The SVM accuracy values continued to increase for the 50 nM and 100 nM concentration levels (94.32±1.47 and 96.39±1.16% respectively). With the GCaMP6 method, the beating rate decreased by 32.93% and 56.39% for 50 and 100 nM, respectively (Fig. 3.4C), which were statistically significant. A change in the SR_{90} value, a 45.42% increase, was statistically significant only at the highest concentration of 100 nM, (Fig. 3.4D).

3.3.5 Response to blebbistatin

Blebbistatin is a myosin-II inhibitor and a known excitation-contraction decoupler.[28] The drug compound was administered at an increasing concentration of 1, 10, 100, 500, and 1000 nM. The SVM accuracy values for the 1 nM and 10 nM concentration levels were near 50% (44.02±1.45 and 47.38±1.44% respectively) (Fig. 3.5B). However, at 100 nM, the SVM accuracy increased to 85.08±1.49%. For both 500 and 1000 nM, SVM accuracy values increased to nearly 100% (99.67±0.26 and 99.03±0.57% respectively). Conversely, in the GCaMP6 method, there were no changes for any of the given concentrations (Fig. 3.5C, 3.5D).

As an excitation-contraction decoupler, blebbistatin induces a negative inotropic effect on the iPS-CMs. The expected negative inotropic effects were seen starting at 100 nM (Fig. 3.5A). At the highest concentration of 1000 nM, contraction and relaxation phases were still distinctly seen. However, the max amplitude of the contraction peak for the 1000 nM concentration was

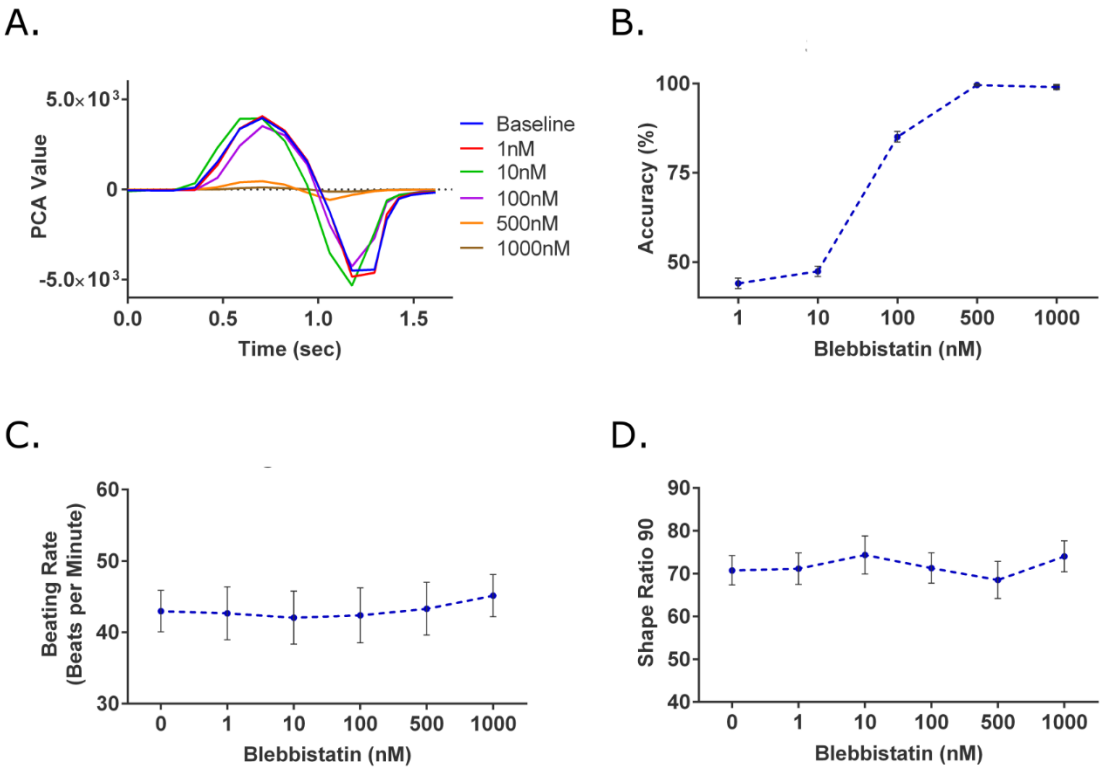

Figure 3.5: Analysis of blebbistatin, a myosin-II inhibitor and excitation-contraction decoupler. (A) Representative traces of the contractile profile from the bright-field method showed significant loss of contractility at higher concentrations. (D) At 1 and 10 nM the SVM accuracies were near 50%, suggesting minor to no changes in iPS-CMs. At 100 nM, the accuracy increased to 85.08 $\pm$ 1.49%. For 500 and 1000 nM, the respective SVM accuracies further increased and were both near 100% (n = 11). As expected with the GCaMP6 method, blebbistatin resulted in a false negative with no changes in (C) beating rate or (D) SR_{90} at any of the tested concentrations (n = 11).

approximately 33-fold smaller than that of the baseline measurement (121.00 PCA value compared 3976.42 PCA value).

3.4 Discussion

There is a pressing need for the development of new drug screening assays, as current methods remain inadequate at detecting and predicting the cardiotoxicity of compounds. Leveraging the capabilities of human stem cells to yield human cardiomyocytes, we present a simple and inexpensive method that can identify drug-induced cardiac effects in iPS-CMs. The method pairs brightfield imaging with optical flow and machine learning, and in all cases the method met or

exceeded the sensitivity of a more traditional fluorescent-based intracellular calcium assay. Thus, we believe our method has the potential to be used in high-throughput assays to identify compounds with potential cardiotoxicity.

In conditions where no drug effects are anticipated (e.g. placebo experiments), the SVM accuracy values were expected to be around 50%, reflecting the random chance of correctly predicting the presence or absence of the drug or intervention. With successive addition of compounds that are cardioactive, we would expect an increase in the SVM accuracy as the decision boundary becomes more distinct. As a way to assess this method, iPS-CMs that are genetically encoded with a calcium indicator, GCaMP6, were used as a control method due to its similarities to multiple commercially available drug screening assays.

The average SVM accuracies obtained from the three longitudinal time points (90, 120, and 150 minutes) was 48.84%, and the average of all four placebo conditions was 50.42%. Furthermore, the GCaMP6 data had no statistical significance in the recorded parameters among the conditions in both these control experiments. These data suggests only small, but still negligible, variations in iPS-CM behavior over time. Thus, both the longitudinal and placebo experiments confirmed that when machine learning is applied to data of iPS-CMs in the absence of cardioactive compounds, the SVM accuracy values would be in the range of 50%.

For the drug experiments, all three compounds were purposely selected for their known effect on iPS-CM behavior. The compounds E-4031 and verapamil are known to have very strong electrophysiological effects and only secondarily affect contractility. While calcium transients are not a direct readout for cardiomyocyte electrophysiology, previous findings have shown that changes in calcium transient are reliable surrogate readouts for changes in electrophysiology as

they reflect changes in the excitation-contraction coupling.[25,184,185] Assays that utilize calcium transient measurements have been shown to specifically detect changes in human stem cell-derived cardiomyocytes induced by E-4031 and verapamil.[25,184] By demonstrating that the brightfield method can capture the effects of these drugs (E-4031 and verapmil) that primarily affect cardiomyocyte electrophysiology, we will have shown that the brightfield method is not only effective to screen compounds that primarily affect contractility but is more broadly applicable.

As expected, a more pronounced difference in iPS-CM behavior caused by increasing concentrations of cardioactive compounds resulted in an increase in accuracy of the machine's prediction, as summarized in Table 1. Looking at E-4031, the SVM accuracy values remained around 50% at the lower concentrations (1, 3, and 5 nM), indicating that there were no cardioactive effects at the given concentrations. As higher concentrations were introduced, noticeably higher SVM accuracy values were achieved (79.82% and 83.56% for 10 and 30 nM respectively), suggesting drug-induced effects. These observations were corroborated by the GCaMP6 data, which showed statistical significance among the parameters at 10 and 30 nM.

Table 3.1: Summary of the SVM accuracies calculated for the concentrations of each drug compound with the bright-field method.

E-4031		**Verapamil**		**Blebbistatin**	
Concentration	Accuracy	Concentration	Accuracy	Concentration	Accuracy
1 nM	47.38%	1 nM	64.52%	1 nM	44.02%
3 nM	50.45%	10 nM	90.64%	10 nM	47.38%
5 nM	49.19%	50 nM	94.32%	100 nM	85.08%
10 nM	79.82%	100 nM	96.38%	500 nM	99.63%
30 nM	83.55%			1000 nM	99.04%

This separation in accuracy values highlights the utility and applicability of machine learning for drug screening purposes.

Interestingly, at 10 nM of verapamil, a SVM accuracy of 90.64% was reported, indicating a change in cardiomyocyte behavior, while the lowest concentration level that had a significant change in the GCaMP6 data was at 50 nM. Verapamil inhibits the L-type Ca^{+} channel, thus reducing both the amplitude and duration of the calcium transient. Thus, when normalizing by the amplitude to calculate SR_{90}, the decrease in CTD_{90} could be masked by the decrease in amplitude. The shortened contractile profile (Fig. 3.4A) and decrease in CTD_{90}, may suggest that the effects of verapamil were masked at lower concentrations. If this is the case, the increases in SR_{90} values at higher concentrations indicate that the relative decrease in the amplitude is greater than the decrease in the duration of the calcium transient.

The SR_{90} parameter is prone to inaccuracies in drug compounds that elicit similar and simultaneous changes in the amplitude and duration of calcium transients. However, it is necessary as a means of normalization to counteract the photobleaching effect seen in the GCaMP6 method. Attempts to normalize the decay to the control experiments were not possible as the decay pattern among each sample of the longitudinal experiments greatly differed (Fig. A1.2). Due to unpredictability of this decay, modeling the decreasing trend as linear or exponential functions dependent on the acquisition number was unsuccessful as well. This photobleaching effect is not unique to the GCaMP6 method, but rather present in most fluorescence-based techniques. Although there are ways to minimize photobleaching effects, there are considerable trade-offs. One method of adjustment is reducing the laser intensity; however, this reduces signal-to-noise ratio and does not remove the photobleaching effect altogether. A line-scan mode of acquisition can significantly reduce photobleaching, but this

method eliminates wide field-of-view image acquisition, making it less suitable for high-throughput screening. The brightfield method is not subject to this photobleaching effect and can be adapted for high–throughput, longitudinal studies on the same set of the iPS-CMs without degradation of signals.

Blebbistatin, a myosin II inhibitor, was expected to have no changes in the GCaMP6 signal as the inhibition occurs downstream in the proteins that generate the force of contraction, and not intracellular calcium. The predictions of blebbistatin as a false negative in the GCaMP6 method were confirmed as the analysis showed there were no differences in any of the tested concentrations. However, in the brightfield method, a decrease in the amplitude of the contractile profile was seen starting at 100 nM. This experiment clearly demonstrates that methods based on the electrophysiological profiles, such as patch clamping, fluorescence-based optics, and MEA, are prone to type II errors with drugs such as blebbistatin that decouple excitation and contraction of iPS-CM. Thus, it is crucial in future cardiotoxicity drug screening assays to have a component that monitors contraction and relaxation of the iPS-CMs.

The progression of the field towards including assays that monitor contractility is supported by the number of commercially available systems that use impedance-based arrays.[172,186–189] However, impedance-based arrays require a minimum number of iPS-CMs in a monolayer to attain a signal. Because various culture techniques have been presented to acquire more physiologically relevant iPS-CMs including multi-culture systems with fibroblasts and endothelial cells, pacing, and culturing on 3-D platforms with anisotropic features, the implementation of impedance-based arrays with such techniques is very difficult. [68–70,82,190,191] In contrast, the brightfield method is simple as the only requirement is an optically clear platform that allows real-time acquisition of brightfield images. The flexibility also allows this method to

complement current techniques, such as intracellular calcium transients, to provide better accuracy. Furthermore, this method is not limited to high-throughput drug screening purposes; it can be easily employed for basic research use (e.g. as a readout in the study of iPS-CM maturation).

The concept of using image-based analysis of cardiomyocyte beating dynamics has been explored by various research groups.[42,64,192] However, these studies have all required the need for custom cell culture apparatuses. More recently, research groups have investigated brightfield-based methods that are widely applicable to both standard cell culture apparatuses, such as a 384-well cell culture plates, and custom ones.[193–200] These respective methods have all demonstrated the feasibility of tracking the contractile behavior of cardiomyocytes and extracting out quantitative parameters to describe the apparent motion. Maddah et al. validated the practicability of using brightfield microscopy to monitor contractile behavior of cardiomyocytes in various setups: monolayer, cardiosphere and single cell.[201] There are primarily two strategies in achieving this: (i) methods that derive signals based on pixel differences or derivatives between frames and (ii) methods that derive signals based on generated motion vectors.

In this study, the latter, a vector-based strategy using optical flow, was chosen as we have previously demonstrated that the directional component of a vector can be crucial in the analysis of cardiomyocyte motion.[51] When looking at just the magnitude of pixel differences or vector displacement, a contractile beat is assumed to be represented by two distinct peaks (one representing the contraction phase and one representing relaxation).[197,199] The ability to discern between the two phases can be achieved if a resting phase is present. However, if the beating frequency of the cells is increased, multiple phases can be embedded into one singular peak as

we have shown in our previous study.[51] Thus, methods that analyze both the magnitude and directional components of vectors should provide more detailed information.

Admittedly, a potential limitation in this study's set-up is the higher computational resource requirement of the used the optical flow algorithm when compared to other algorithms used for vector-based methods (e.g. block-matching and minimum quadratic difference algorithms).[195,198–200] However, the advantages of image segmentation and signal processing using PCA along with machine learning analysis can be leveraged by applying these techniques to the vectors of such other algorithms. The implementation of PCA summarizes the magnitude and directional components of vectors into one dimensional data. It automatically discerns the contraction phases (positive PCA values) from the relaxation phases (negative PCA values). In addition, while not demonstrated in this study, the calculated spatial PCA can be applied to segment asynchronously beating cell clusters. The SVM accuracy calculated in our method serves as a singular quantitative index or metric that summarizes not only the impact of the 12 parameters, but also any underlying relationships or interactions among parameters. This index becomes valuable for high-throughput screening of drug-induced cardiotoxicity by highlighting compounds that have any cardioactive effect on the contractile behavior of cardiomyocytes.

In summary, we present a screening method that combines brightfield microscopy and machine learning to enable the sensitive detection of changes in the contraction of human iPS-derived cardiomyocytes. Unlike fluorescence-based methods that suffer from photobleaching, this brightfield method does not result in the loss of signal over time even in longitudinal studies. Furthermore, this approach can be implemented in combination with other screening methods, and provides insights on how patterns in electrophysiological data are coupled to those of

contraction. Moreover, this method is easily adaptable to various configurations, even 3D tissue models, to enable easy, robust, and information-rich readouts of cardiomyocyte behavior.

Chapter Authors

Eugene K. Lee[#], Yosuke Kurokawa[,#], Robin Tu, Steven C. George[§], and Michelle Khine[§]

[#,§]Authors contributed equally to this chapter

Final publication is available through Nature Publishing Group,

http://dx.doi.org/10.1038/srep11817

Chapter 4: Modeling Trastuzumab-Related Cardiotoxicity *in vitro* Using Human Stem Cell-Derived Cardiomyocytes

4.1 Introduction

Cardiotoxicity screening using human pluripotent stem cell-derived cardiomyocytes (hPSC-CMs) has rapidly evolved over the past decade. Initial efforts, including the Comprehensive *in vitro* Proarrhythmia Assay (CiPA) initiative, have focused on using hPSC-CMs to determine the arrhythmogenic potential of drugs, as several FDA-approved drugs have been pulled off the market due to proarrhythmic side effects.[202–204] While significant shortcomings still exist, hPSC-CMs have proven to accurately detect clinically-relevant proarrhythmic cardiotoxicity for the majority of compounds tested to date.[23–25,170,187,205,206] Combined with the ability of induced pluripotent stem cell-derived cardiomyocytes (iPS-CMs) to recapitulate patient-specific phenotypes, novel drugs and therapeutics can be developed to target specific electrophysiological disease states.[207–209]

More recently, researchers have explored the use of hPSC-CMs to better understand drug-induced structural cardiotoxicity, defined as compounds that lead to decreased cardiomyocyte viability.[210–213] Given the wide use of anticancer drugs with known clinical cardiotoxicity through loss of cardiomyocytes (e.g. anthracyclines such as doxorubicin),[214] it is especially important to have a human *in vitro* platform that can rapidly screen new compounds for potential structural cardiotoxicity. Several recent studies have leveraged hPSC-CMs to develop a mechanistic understanding of doxorubicin-induced cardiotoxicity.[215–218]

Separate from anthracyclines, the use of targeted drugs that inhibit specific pathways critical for cancer progression have also gained broad clinical use.[219] These compounds have led to

improved clinical outcomes in certain cancer types; however, incidents of clinical cardiotoxicity associated with these drugs have been reported.[220,221] One such compound is trastuzumab (Herceptin®), a monoclonal antibody against ErbB2 (Her2) used to treat patients with $Her2^+$ breast cancer.[93] Trastuzumab, administered with an anthracycline or on its own, significantly increases the incidence of left ventricular dysfunction.[93,94,222–224] Animal studies have shown that ErbB2, together with its co-receptor ErbB4 and its activating ligand neuregulin-1 (NRG-1) are critical for normal cardiac development and homeostasis.[88–90,225] Studies using isolated rat cardiomyocytes have shown that activation of the ErbB2/4 pathway with NRG-1 ameliorates anthracycline-induced cardiotoxicity, suggesting a mechanism for trastuzumab's cardiotoxic effects.[95,226]

Here we utilize human iPS-CMs to model trastuzumab-related cardiotoxicity. We first demonstrate that recombinant NRG-1 provides cardioprotective effects against anthracycline exposure. We observe that ErbB2/4 signaling must be active in order to detect trastuzumab-related cardiotoxicity. We additionally show that heparin-binding EGF-like growth factor (HB-EGF) similarly activates the ErbB2/4 pathway and provides cardioprotection against anthracyclines. We also demonstrate that a CM-EC co-culture platform enables the detection of trastuzumab-related cardiotoxicity through the activation of the ErbB2/4 pathway via EC-secreted NRG-1. Our results demonstrate the potential of using hPSC-CMs to not only detect the arrhythmogenic potential of drugs, but to also detect cardiomyocyte toxicity that impacts viability.

4.2 Materials and Methods

4.2.1 Cell culture

Wild-type human iPSCs reprogrammed from dermal fibroblasts of a healthy male volunteer (cell line WTC-11) were cultured as previously described (gifted by Dr. Bruce Conklin, Gladstone Institutes).[227] The iPSCs express the calcium indicator GCaMP6f, which increases in fluorescent intensity in response to increasing concentrations of Ca^{2+} in the cytosol.[228,229] Routine checks for mycoplasma were performed every 6 months using MycoAlert mycoplasma detection kit (Lonza) following manufacturer's protocol. The iPSCs were used between passages 40-60.

Endothelial colony forming cell-derived endothelial cells (ECFC-ECs) were isolated and cultured in endothelial growth medium-2 (EGM-2, Lonza) as described previously.[230] The ECFC-ECs were used between passages 5-8.

4.2.2 Cardiomyocyte differentiation

A small molecule Wnt modulatory protocol was used as previously described, with modifications[231,232] (Fig. A2.1A). Briefly, iPSCs were grown to ~85% confluence on 6-well plates coated with growth factor reduced Matrigel (Corning) in Essential 8 (E8) medium (Gibco). On Day 0, the medium was changed to RPMI 1640 (Gibco) with B-27 supplement without insulin (RPMI/B-27 -Ins, Gibco) containing 6 µM CHIR99021 (LC Laboratories). On Day 2, the medium was changed to RPMI/B-27 -Ins. On Day 3, the medium was changed to RPMI/B-27 -Ins containing 5 µM IWP2 (Tocris). On Day 5, the medium was changed to RPMI/B-27 -Ins. On Day 7 and 10, the medium was changed to RPMI/B-27 (with insulin), with spontaneously contracting cardiomyocytes appearing on Day 8. Non-cardiomyocytes were removed using lactate selection,[79] changing the medium every two days between Day 13 and 21 with RPMI

1640 without glucose, with 4 mM lactic acid (Sigma-Aldrich), and 25 mM HEPES (Gibco). On Day 24, the iPS-CMs were passaged by incubating in 200 U/ml collagenase II (GIbco) for 1 hour followed by TrypLE Express (Gibco) for 4 minutes. The cells were either cryopreserved using CryoStor10 (STEMCELL Technologies) or replated on Matrigel-coated 6-well plates.

4.2.3 Flow cytometry

The iPS-CMs were passaged between Day 27-30 and fixed in Fixation Buffer (BioLegend) for 20 minutes. The cells were permeabilized in PBS + 0.1% Triton-X (Sigma-Aldrich) and stained using APC-preconjugated anti-cardiac troponin T (cTnT) antibody (Miltenyi Biotec) or a APC-preconjugated isotype control following manufacturer's protocol. The samples were read using the Guava easyCyte flow cytometer (Millipore) and analyzed using FlowJo.

4.2.4 Drug exposure

For all drug exposure studies, the iPS-CMs were passaged and replated on Matrigel-coated 96-well plates at 50,000 cells/well. The targeted concentrations of doxorubicin (LC Laboratories), NRG-1β (R&D Systems), HB-EGF (R&D Systems), trastuzumab (Genentech), and/or corresponding volumes of vehicle control (Milli-Q ultrapure water) was added to the media as specified. The drug exposure studies were performed using iPS-CMs between Day 30-40 of differentiation.

4.2.5 Lactate dehydrogenase (LDH) measurement

After 72 hours of drug exposure, the LDH release was measured using the Pierce LDH Cytotoxicity Assay Kit (Thermo Scientific) following manufacturer's protocol. Absorbance was measured using the Epoch microplate spectrophotometer (BioTek). For dose-dependent analysis, measured absorbance values were calculated relative to the average of the no-drug control

condition ($A_{control}$). For column analysis, the measured values were normalized to the doxorubicin condition (A_{DOX}) and baseline-subtracted the no-drug control condition using the formula: normalized LDH release=$(A_{measured}-A_{control})/(A_{DOX}-A_{control})$.

4.2.6 CM-EC co-culture

Both iPS-CMs and ECFC-ECs were passaged and mixed at the density to seed 40,000 and 2,500 iPS-CMs and ECFC-ECs per well, respectively, in a Matrigel-coated 96-well plate. The cells were fed with EGM-2 for 3 days before drug exposure.

4.2.7 Quantitative real-time PCR

RNA was isolated using the RNeasy Plus Mini Kit (Qiagen) following manufacturer's protocols, and cDNA was produced using the High Capacity RNA-to-cDNA Kit (Applied Biosystems). Gene expression was measured using Taqman Gene Expression Assays (*NRG1*: Hs01101538_m1, *HBEGF*: Hs00181813_m1, *18S*: Hs99999901_s1) using the CFX96 Real-Time PCR Detection System (Bio-Rad). Relative expression was calculated using the comparative C_t method,[233] normalizing the expression level to the iPSCs.

4.2.8 Statistical analysis

All experiments were performed using at least 3 biological replicates per condition, and all results are reported as mean±SD. Significance was calculated using either one-way analysis of variance (ANOVA) in conjunction with Tukey's multiple comparison test or two-way ANOVA in conjunction with Dunnett's or Holm-Sidak's multiple comparison test, with p-values less than 0.05 considered statistically significant. Data were compiled, analyzed, and graphed using Microsoft Excel and GraphPad Prism 6.

4.3 Results

4.3.1 Differentiation and isolation of iPS-CMs

We differentiated the iPS-CMs using an established Wnt modulatory protocol, which was followed by a metabolic selection whereby cardiomyocytes were enriched through their ability to utilize lactate as an energy source. The resulting cell population stained positively for cTnT at 95.08±2.06% as measured by flow cytometry (Fig. A2.1B). A monolayer of iPS-CMs replated in a 96-well plate and stained for cTnT demonstrated semi-organized troponin structures (Fig. A2.1C), indicative of the immature phenotype of iPS-CMs.[33,38]

4.3.2 Cardioprotective effects of NRG-1

We hypothesized that active ErbB2/4 signaling is required to model trastuzumab-related cardiotoxicity *in vitro*. Thus, we first studied the cardioprotective effects of NRG-1 via activation of the ErbB2/4 pathway. Performing a dose-dependent response of iPS-CMs to doxorubicin with or without NRG-1, we observed a statistically significant difference in the dose response curves ($F=23.73$, $p<0.0001$) (Fig. 4.1A). The addition of NRG-1 provided cardioprotective effects, reducing the LDH release by iPS-CMs and shifting the half-maximal effective concentration (EC_{50}) from 163.9 μM to 263.6 μM. The cardioprotective effects were most evident at the higher concentrations of doxorubicin, with statistically significant differences between each point of the curves above 10 μM doxorubicin concentration. Therefore, all subsequent studies utilized doxorubicin concentration of 10 μM, which falls within the range of *in vivo* peak plasma concentration of doxorubicin.[215]

Next, we observed that the cardioprotective effects of NRG-1 is dose-dependent, with concentrations above 0.1 ng/ml causing a statistically significant reduction in LDH release in

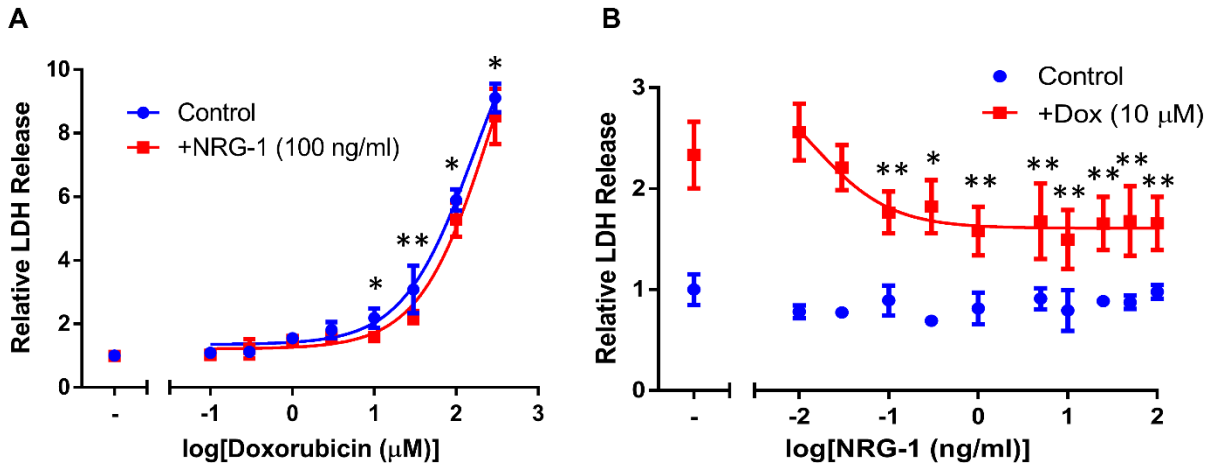

Figure 4.1: Cardioprotective effects of NRG-1. (A) A dose-response curve of doxorubicin with or without the presence of NRG-1 as measured by relative LDH release. (-) indicates no doxorubicin. *p<0.05, **p<0.005 between the control and +NRG-1 for the given doxorubicin concentration. (B) Dose-response curve of NRG-1 with or without the presence of doxorubicin as measured by relative LDH release. (-) indicates no NRG-1. *p<0.05, **p<0.005 compared to control condition with doxorubicin (no NRG-1). Dox = doxorubicin.

response to doxorubicin (Fig. 4.1B). We also observed no significant changes in LDH release following the addition of NRG-1 without doxorubicin exposure, suggesting that the cardioprotective effects of NRG-1 is only detectable under cellular stress. Subsequent studies utilized NRG-1 concentration of 1 ng/ml, which is in the range of average NRG-1 plasma concentration.[234]

4.3.3 Trastuzumab-related cardiotoxicity

When iPS-CMs were exposed to varying concentrations of trastuzumab, no difference in LDH release was observed with or without the addition of doxorubicin (Fig. 4.2A). Even in the presence of NRG-1 (i.e. active ErbB2/4 signaling), the addition of trastuzumab did not lead to any increased LDH release. However, in the presence of both NRG-1 and doxorubicin, it was possible to detect the cardiotoxic effects of trastuzumab (Fig. 4.2B). While the addition of NRG-1 resulted in a 56±14% decrease in normalized LDH release compared to doxorubicin alone, the

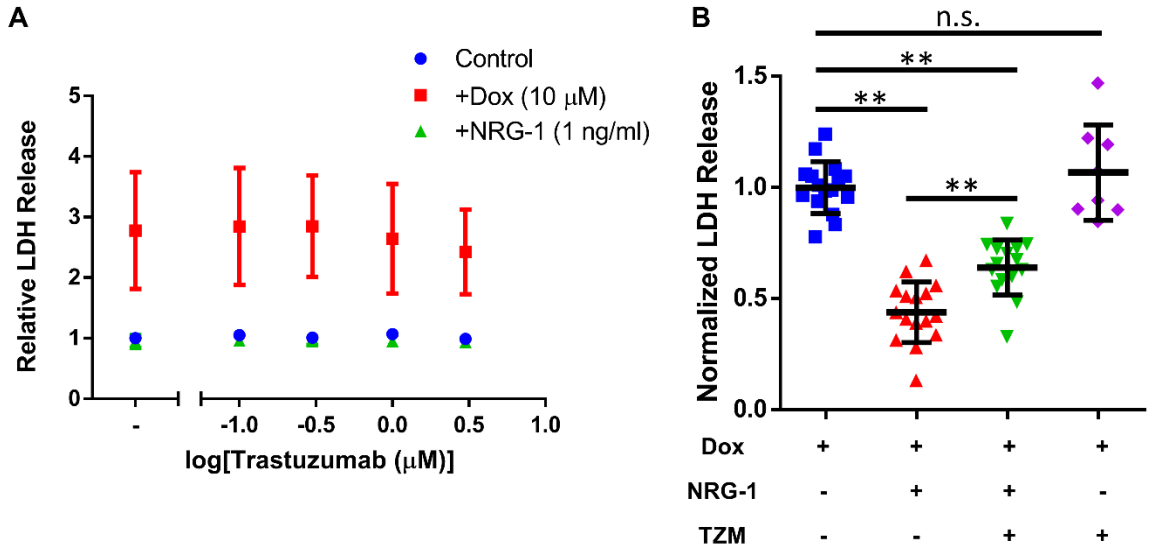

Figure 4.2: Cardiotoxicity of trastuzumab. (A) A dose-response curve of trastuzumab with doxorubicin or NRG-1 as measured by relative LDH release. None of these conditions detect trastuzumab-related cardiotoxicity. (-) indicates no trastuzumab. (B) Trastuzumab (1 μM), combined with doxorubicin (10 μM) and NRG-1 (1 ng/ml), increases the normalized LDH release compared to having doxorubicin and NRG-1 without trastuzumab. Adding trastuzumab and doxorubicin without the addition of NRG-1 does not increase LDH release compared to having doxorubicin alone. **p<0.005. TZM = trastuzumab.

addition of both NRG-1 and trastuzumab led to a smaller (36±12%) decrease; in other words, comparing the two conditions with both doxorubicin and NRG-1, the addition of trastuzumab led to a 58±38% increase in normalized LDH release.

4.3.4 Cardioprotective effect of HB-EGF

Next, we explored whether we can observe a similar cardioprotective effect using HB-EGF, another ligand that binds to ErbB4 and activates the ErbB2/4 pathway. Similar to NRG-1, we observed a dose-dependent cardioprotective effect of HB-EGF against doxorubicin-induced cardiotoxicity (Fig. 4.3A). We also did not observe a change in LDH release by the addition of HB-EGF without the presence of doxorubicin. In the presence of HB-EGF, we also detected the cardiotoxic effects of trastuzumab (Fig. 4.3B). The addition of HB-EGF resulted in a 26±19% reduction in the normalized LDH release, but the addition of both HB-EGF and trastuzumab

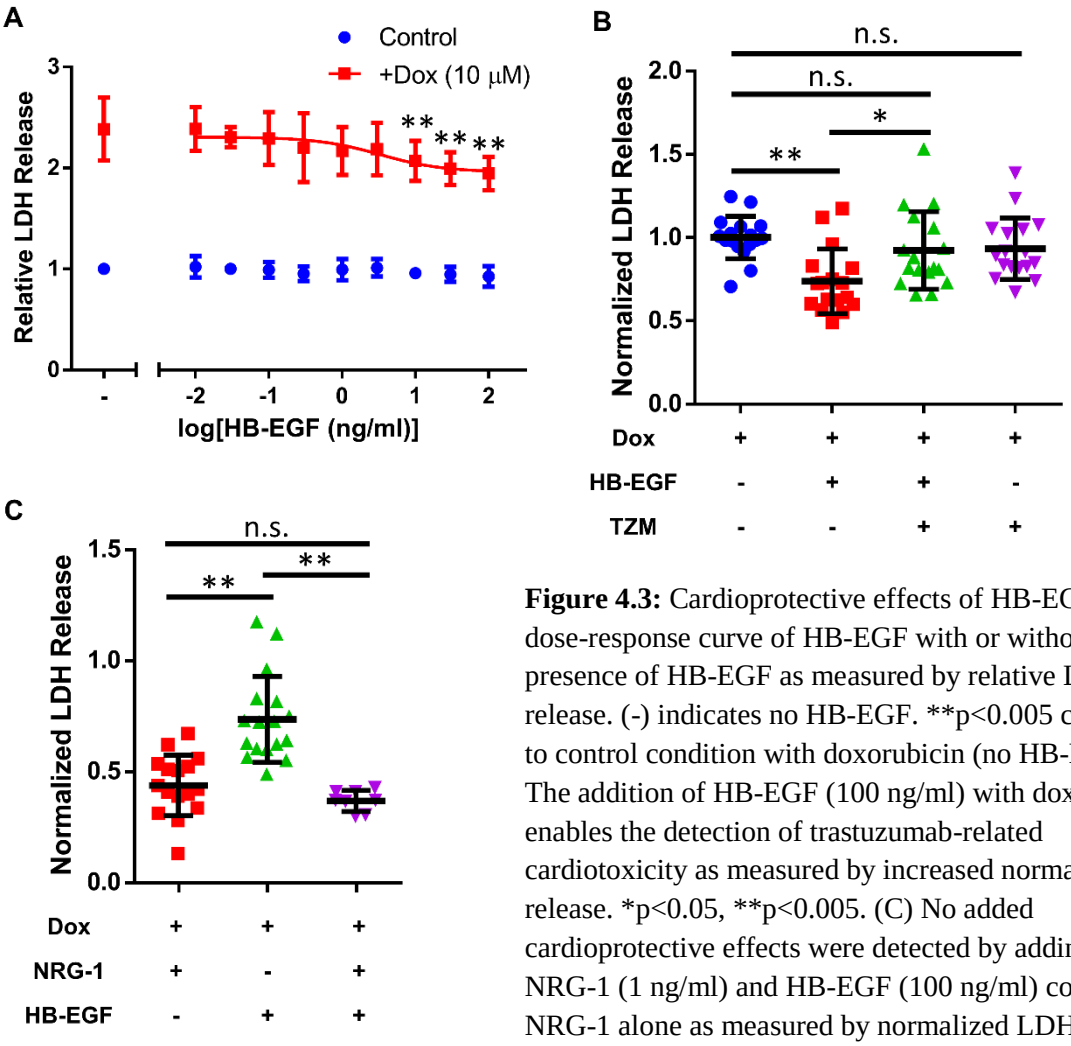

Figure 4.3: Cardioprotective effects of HB-EGF. (A) A dose-response curve of HB-EGF with or without the presence of HB-EGF as measured by relative LDH release. (-) indicates no HB-EGF. **p<0.005 compared to control condition with doxorubicin (no HB-EGF). (B) The addition of HB-EGF (100 ng/ml) with doxorubicin enables the detection of trastuzumab-related cardiotoxicity as measured by increased normalized LDH release. *p<0.05, **p<0.005. (C) No added cardioprotective effects were detected by adding both NRG-1 (1 ng/ml) and HB-EGF (100 ng/ml) compared to NRG-1 alone as measured by normalized LDH release. **p<0.005.

removed any statistically significant cardioprotective effects (decrease of 7.8±23%, p=0.6257). Comparing the two conditions with both doxorubicin and HB-EGF, the addition of trastuzumab resulted in a 27±24% increase in normalized LDH release.

Comparing the degree of cardioprotection provided by NRG-1 and HB-EGF, we observed that NRG-1 significantly reduces the normalized LDH release compared to HB-EGF (Fig. 4.3C). Importantly, the addition of both NRG-1 and HB-EGF does not provide any additional cardioprotective effects compared to NRG-1 alone (56±14% vs. 63±5%, p=0.549).

4.3.5 CM-EC co-culture platform

Since NRG-1 is mainly secreted by endothelial cells in the cardiac microenvironment,[86] we aimed to recapitulate this phenomenon using a co-culture of iPS-CMs and ECFC-ECs. First, we measured that NRG-1 is expressed by the ECFC-ECs using qPCR and ELISA. Compared to iPSCs and iPS-CMs, the ECFC-ECs have significantly higher *NRG1* expression (Fig. 4.4A). The secretion of NRG-1 into the growth medium was confirmed using ELISA, with protein concentrations reaching 604±142 pg/ml in 48 hours. This level of NRG-1 is sufficient to observe a significant cardioprotective effect based on the NRG-1 dose-response experiment (Fig. 4.1B).

In order to produce a simple and reproducible co-culture platform that is amenable to high-throughput analysis, we utilized a monolayer co-culture in 96-well plates. The iPS-CMs and ECFC-ECs were seeded at a ratio of 16:1 (40,000:2,500) in order to promote even distribution of the two cell types (Fig. 4.4B), whereas using higher concentrations of ECFC-ECs resulted in the

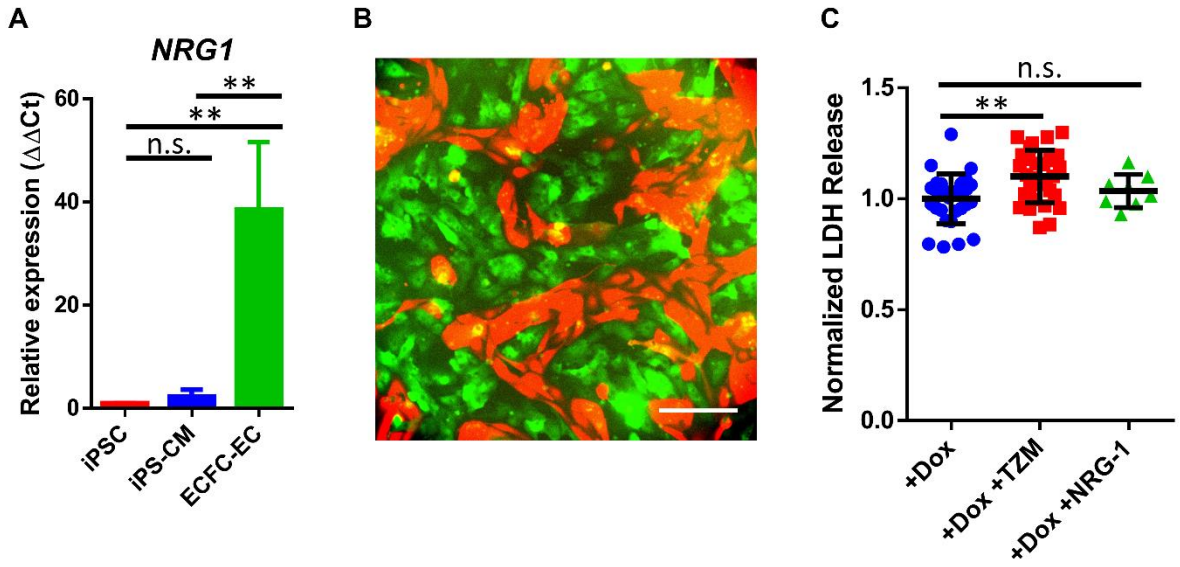

Figure 4.4: Co-culture of iPS-CM and ECFC-EC. (A) Relative expression of *NRG1* between the iPSCs, iPS-CMs, and ECFC-ECs. **p<0.005. (B) Representative image of the CM-EC co-culture. Green = iPS-CM (GCaMP6), red = ECFC-EC (transduced). Scale bar = 250 μm. (C) The addition of trastuzumab with doxorubicin increases normalized LDH release compared to doxorubicin alone. **p<0.005.

overcrowding of ECFC-ECs (Fig. A2.2). Using this co-culture platform, we were able to detect the cardiotoxic effects of trastuzumab. The addition of both doxorubicin and trastuzumab increased the normalized LDH release by 10±12% compared to doxorubicin alone, which was statistically significant (Fig. 4.4C). The addition of exogenous NRG-1 did not result in a reduced LDH release, suggesting that the cardioprotective effects of ErbB2/4 signaling is already active via EC-secreted NRG-1.

4.4 Discussion

Since the advent of hPSC-CMs, their potential use in drug screening applications has rapidly expanded.[235] In our study, we demonstrate that iPS-CMs are capable of detecting trastuzumab-related cardiotoxicity when ErbB2/4 signaling is active, suggesting that trastuzumab is blocking the cardioprotective effects of the ErbB2/4 pathway. While NRG-1 is recognized as the main activator of the ErbB2/4 pathway in the cardiac microenvironment, we demonstrate that HB-EGF can also activate the same cardioprotective pathway. Additionally, we demonstrate that a co-culture platform of iPS-CMs and ECs recapitulates the physiological effects of EC-secreted NRG-1 activating the ErbB2/4 pathway.

ErbB2/4 signaling has critical functions in cardiac development, including trabeculation and formation of the conduction system.[88–90,236] While previous studies have explored the role of ErbB2/4 signaling in hPSC-CM differentiation,[91,237] it remained unclear whether hPSC-CMs can recapitulate the cardiotoxic effects of ErbB2 inhibition via trastuzumab exposure. Here we demonstrate that, while functionally immature, iPS-CMs can recapitulate the cardioprotective effects of ErbB2/4 signaling and the cardiotoxic effects of ErbB2 inhibition. Without the addition of NRG-1 or HB-EGF to activate the ErbB2/4 pathway, we were not able to detect trastuzumab-

related cardiotoxicity. This result differs from two recent studies that observed change in cell impedance and gene expression when hPSC-CMs were exposed to trastuzumab without the addition of NRG-1 or HB-EGF.[99,238] Interestingly, both studies used a commercially available source of iPS-CMs and a proprietary maintenance medium, which may contain growth factors that activate the ErbB2/4 pathway. The proprietary medium also contains animal-derived serum, which has inherent variability between lots and can mask the effects of drugs.[147,239] While we utilized a serum-free growth medium, it is important to develop a chemically-defined medium that contains growth factors appropriate for the cardiac microenvironment in order to improve the relevance of iPS-CMs for drug screening applications.

While NRG-1 is widely known as the activating ligand of the ErbB2/4 pathway, we identify HB-EGF as having a similar pattern of activation that results in cardioprotective effects against doxorubicin. The addition of both NRG-1 and HB-EGF did not confer additive cardioprotective effects, suggesting that both ligands activate ErbB2/4 signaling that is saturated by the addition of NRG-1 alone at the tested concentrations. Therapeutic use of recombinant NRG-1 has been extensively explored in animal models, showing improved cardiac function in disease models such as myocardial infarction and doxorubicin-induced cardiomyopathy.[240] Clinical trials have also shown promising data on treating chronic heart failure patients using recombinant NRG-1.[241,242] HB-EGF has been shown to be critical in cardiac development and homeostasis in mice through ErbB2/4 activation,[243] but its potential therapeutic use in treating cardiovascular disease has remained largely unexplored.[244] While the cardioprotective effects of HB-EGF was less pronounced compared to NRG-1 in our study, the clinical potential of HB-EGF warrants further investigation.

Trastuzumab has clinically been shown to induce cardiotoxic side effects including reduction in the left ventricular ejection fraction (LVEF) and increases in the serum cardiac troponin I (cTnI) concentration, suggesting ErbB2 inhibition directly affects cardiomyocyte viability.[222,224] Loss of cardiomyocytes is largely irreversible in the adult heart, and a recent study showed that treatments using trastuzumab (with or without doxorubicin) resulted in reduced LVEF that does not recover back to baseline after 5 years.[223] On the other hand, we observed that the addition of doxorubicin was necessary to detect trastuzumab-related cardiotoxicity using iPS-CMs. The finding supports the existing theory that trastuzumab potentiates pre-existing cardiac stress (drug-induced or otherwise) by inhibiting the cardioprotective effects of ErbB2/4 signaling.[245–247] Mice with cardiac deletion of *ErbB2* led to increased susceptibility to anthracycline-induced cardiomyocyte death, suggesting that the physiological functions of ErbB2/4 signaling are critical in preventing the progression of cardiac injury.[225,248] No overt phenotype initially appears in these mice, consistent with our finding that ErbB2 inhibition on its own does not induce acute cardiotoxic effects.

Other potential mechanisms of trastuzumab-related cardiotoxicity have been proposed. Trastuzumab has been shown to induce antibody-dependent cell-mediated cytotoxicity by natural killer cells on Her2+ tumors,[249] a process by which cardiomyocytes may be similarly affected. Wilkinson et al.[250] recently showed that human cardiac microvascular endothelial cells also express ErbB2 and that their permeability is affected by exposure to trastuzumab. While we did not observe any loss of EC viability through exposure to trastuzumab (data not shown), the increased permeability may be a contributing factor to the clinically observed cardiotoxicity by promoting higher transport and accumulation of doxorubicin into the heart. Barth et al.[251] demonstrated that trastuzumab reduces the angiogenic capacity of human cardiosphere-derived

cells *in vitro,* suggesting that trastuzumab exposure may affect the vascular response to stress in the cardiac environment. Kirabo et al.[252] recently showed that human cardiac ventricular fibroblasts also respond to NRG-1 signaling, promoting the secretion of pro-reparative factors. While we demonstrated that a simple co-culture system of iPS-CMs and ECs recapitulate features of trastuzumab-related cardiotoxicity, it does not fully resolve all the potential mechanisms of toxicity. With recent advancements in creating complex tissues and microphysiological systems *in vitro,*[253,254] future studies should aim to utilize multicellular screening platforms to better model trastuzumab-related cardiotoxicity. Such platforms can be leveraged during drug development to identify modes of cardiotoxicity that may be otherwise missed using a cardiomyocyte mono-culture platform.

One limitation in our study is that we utilized a single iPSC line. Recent studies have demonstrated that clinically-relevant cardiotoxicity of doxorubicin and sotalol can be predicted using iPS-CMs differentiated from patient-derived iPSCs.[208,215] Much like doxorubicin, not every patient treated using trastuzumab shows clinical symptoms of cardiac dysfunction.[255] It remains to be seen if trastuzumab-related cardiotoxicity is a phenotype that is similarly dependent on the genetic background of the patient and can be recapitulated using patient-derived iPS-CMs. Such patient-specific models can be utilized to further our mechanistic understanding of trastuzumab-related cardiotoxicity and aid in the development of therapeutic targets to more effectively combat trastuzumab-related cardiotoxicity.

Another limitation in our study was the use of LDH release as the readout of cardiotoxicity. LDH release is a clinically-relevant readout for cardiac injury but lacks specificity.[256] We observed that in the CM-EC co-culture platform, the ECs contributed a non-negligible amount of LDH, which resulted in decreased sensitivity in detecting LDH release by the cardiomyocytes. While

more costly and time-consuming, cardiomyocyte-specific markers of toxicity, such as cTnI and cTnT release, can be utilized in the future for improved sensitivity and specificity in cardiotoxicity screening.

In conclusion, we demonstrate that iPS-CMs recapitulate the cardioprotective effects of ErbB2/4 signaling and the cardiotoxic effects of ErbB2 inhibition by trastuzumab. We also establish a simple and high-throughput CM-EC co-culture platform that recapitulates physiological crosstalk between the two cell types including activation of ErbB2/4 signaling via EC-secreted NRG-1. Further advancements in our ability to model the human cardiac microenvironment *in vitro* will be critical in broadening our understanding of trastuzumab-related cardiotoxicity.

Chapter Authors

Yosuke Kurokawa, Michael R. Shang, Rose T. Yin, Steven C. George

Chapter 5: Human Induced Pluripotent Stem Cell-Derived Endothelial Cells for Three-Dimensional Microphysiological Systems

5.1 Introduction

Nearly every tissue within the human body relies on vasculature for delivery of nutrients and oxygen and removal of waste. In addition, the endothelial cells (EC) that line the vasculature play critical roles in organ development, homeostasis, and disease progression.[257–259] The burgeoning field of microphysiological systems (MPS, or "organ-on-a-chip") seeks to create human tissue mimics at the micron to millimeter scale. These model systems have important applications in the areas of *in vitro* pharmacokinetic modeling, drug toxicity, and drug efficacy. The incorporation of dynamic and functional vascular networks into microphysiological systems remains a priority, as it significantly advances the physiological relevance of these systems.[253,260–262] A variety of methods have been developed for creating 3D vasculature *in vitro*,[145,263,264] but we and others have focused on utilizing the native vasculogenic program of endothelial cells to spontaneously form robust and perfusable vascular networks in microfluidic devices.[230,265–271] Such methods are amenable to including other functional cells types (e.g., hepatocytes, cardiomyocytes) to create complex, vascularized tissues that may be used for drug screening and mechanistic studies.[272–275]

While efforts in the field have mostly revolved around the use of primary cells, there has been growing interest in using human pluripotent stem cells (hPSC) as the source of endothelial cells to create vessel networks. Employing a single stem cell line to derive endothelial cells has several important advantages. First, concerns over donor-to-donor variability in primary cells are ameliorated. Second, advances in gene editing (e.g. CRISPR) have facilitated the creation of

stem cell lines that have useful reporters or modified functions for mechanistic studies.[276] Finally, the use of human induced pluripotent stem cells (hiPSC) offers the potential to perform disease-specific and patient-specific drug screening *in vitro*.[253,277–280] Future applications may also include using iPSC-derived endothelial cells (iPS-EC) as an autologous cell source for regenerative medicine.

Several differentiation protocols now exist to create endothelial cells from hPSCs, usually defined by the expression of definitive endothelial markers such as platelet-endothelial cell adhesion molecule-1 (PECAM1, or CD31), vascular endothelial (VE)-cadherin (CD144), endothelial nitric oxide synthase (eNOS), and von Willebrand factor (vWF).[281–283] However, studies that investigate their potential uses in microphysiological systems have been limited. Belair et al.[271] recently showed promising results using iPS-ECs for various *in vitro* assays that demonstrate their physiological functions. In particular, they demonstrate the key roles of VEGF and FGF signaling in sprouting angiogenesis of iPS-ECs. Most previous works have used primary cell sources such as human umbilical vein endothelial cells (HUVEC) and endothelial colony forming cell-derived endothelial cells (ECFC-EC), with ECFC-EC being considered the desired cell source due to their high proliferative capacity and vasculogenic potential.[284] It is of great interest in the field to further understand how iPS-ECs perform in these platforms, thus providing an important alternative to primary endothelial cells.

Herein we investigate the vasculogenic potential of iPS-ECs derived from an mCherry-VE-Cadherin fusion protein reporter iPSC line. The cells demonstrate physiological functions of endothelial cells, display a predominantly venous phenotype, respond to shear stress, and form perfusable vascular networks within 3D microfluidic devices. We also demonstrate drug

screening capabilities of the platform by observing changes in the vasculature in response to small molecule inhibitors.

5.2 Materials and Methods

5.2.1 Cell culture

Two human iPSC lines were used in the experiments: WTC11 (gifted by Dr. Bruce Conklin, Gladstone Institutes) and C2A (gifted by Dr. Gordana Vunjak-Novakovic, Columbia University). The iPSC were cultured as described previously,[232] with modifications. Briefly, the cells were grown on 6-well plates coated with growth factor reduced Matrigel (Corning) in Essential 8 (E8) Medium (Thermo Scientific) with daily media replacement. The cells were passaged at 80% confluence using StemPro Accutase (Life Technologies) and seeded on Matrigel-coated plates in E8 medium containing 10 μM Y-27632 (LC Laboratories), a Rho-associated protein kinase (ROCK) inhibitor. All cells were cultured at 37 °C and 5 % CO_2.

Human umbilical arterial endothelial cells (HUAEC), human umbilical venous endothelial cells (HUVEC), and human dermal lymphatic endothelial cells (HDLEC) were purchased from PromoCell and cultured according to manufacturer protocols. Endothelial colony forming cell-derived EC (ECFC-EC) were isolated and cultured as described previously.[230] Normal human lung fibroblasts (NHLF) were purchased from Lonza and cultured according to manufacturer protocols. The cells were used between passages 3-6.

5.2.2 CDH5-mCherry iPSC line

The CDH5-mCherry tagged cell line was generated from the GCaMP6-WTC11 human iPSC line[229] by the Genome Engineering and iPSC Center (GEiC), Washington University in St. Louis. The GCaMP6-WTC11 line constitutively expresses GCaMP6 and can thus be used to

report changes in intracellular calcium. Approximately 2×10^6 WTC11 iPSCs were resuspended in P3 primary buffer and electroporated using a 4D-Nucleofector (Lonza) with 1.5 μg of *CDH5-mCherry* donor plasmid (GeneArt), 1 μg gRNA (MS232.CDH5.g11 targets 5'-taggcggccgaggtcactc tgg-3' near the CDH5 stop codon) and 1.5 μg Cas9 vectors using nucleofection program CA-137. Following nucleofection, cells were single-cell sorted and screened with PCRs using primer sets specific to genomic and donor plasmid regions. The overall nucleofection efficiency was 50-60% based on the expression of a co-delivered GFP construct. CDH5-mCherry tagged region of final clones was sequence-confirmed using Sanger sequencing.

5.2.3 Derivation and isolation of iPS-EC

The iPS-EC were differentiated following a previously established protocol (Fig. 5.1A).[285] Briefly, ~80% confluent iPSC were split 1:4 onto Matrigel-coated tissue culture flasks as described above (Day 0). Between Day 0 and Day 2 of differentiation, the cells were cultured in E8BA medium, which consisted of E8 medium supplemented with 5 ng/ml BMP4 (R&D) and 25 ng/ml Activin A (PeproTech), with daily medium replacement. On Day 0 of differentiation, 10 μM Y-27632 was added to the E8BA medium. Between Day 2 and Day 6 of differentiation, the cells were cultured in E7BVi medium, which consisted of Essential 6 (E6) Medium supplemented with 100 ng/ml FGF2 (PeproTech), 10 ng/ml BMP4, 50 ng/ml VEGF-A (PeproTech), and 5 μM TGF-β inhibitor SB431542 (STEMCELL Technologies), with daily medium replacement. On Day 6, the cells were passaged using TrypLE (Life Technologies) and sorted using CD31 Microbead Kit (Miltenyi Biotec) and EasySep™ Magnet (STEMCELL Technologies) following manufacturer protocols. After purification, the $CD31^+$ cells were cultured on tissue culture flasks coated with human fibronectin (1 μg/cm^2, Millipore) in E7V

medium (E6 + 100 ng/ml FGF2 + 50 ng/ml VEGF-A). The cells were passaged on Day 8 using TrypLE and frozen in CryoStor10 (STEMCELL Technologies) at $1x10^6$ cells/ml. All experiments were performed using cells between Day 10-18 differentiation.

5.2.4 Flow cytometry

Cells were passaged using TrypLE and fixed in Fixation Buffer (BioLegend) for 20 minutes. The cells were washed in PBS and stained in Cell Staining Buffer (BioLegend) with CD31 (Dako), CD90 (STEMCELL Technologies), or mouse IgG isotype control (Dako) for 30 minutes at room temperature, followed by secondary antibody staining using goat anti-mouse IgG (H+L) Alexa Fluor 647 (Invitrogen). The cells were also stained using preconjugated antibodies FITC-CD45 (BioLegend), PE-CD133 (Miltenyi Biotec), APC-CD34 (BioLegend), or a corresponding preconjugated isotype control (BioLegend) in Cell Staining Buffer for 30 minutes at room temperature. The samples were read using the Guava easyCyte Flow Cytometer (Millipore) with a default number of events set at 5,000 and analyzed using FlowJo.

5.2.5 Immunofluorescent staining

Cells were fixed in 4% paraformaldehyde or 10% neutral buffered formalin for 10 minutes. Permeabilization was performed using 0.1% Triton-X in PBS for 10 minutes. The cells were blocked in 10% goat serum for 20 minutes. The cells were stained using antibodies for CD31 (Dako), VE-cadherin (R&D), von WIllebrand Factor (Abcam), eNOS (BD Biosciences), LYVE-1 (Abcam), Podoplanin (BioLegend), PROX1 (Abcam), or laminin (Abcam) in PBS with 2% bovine serum albumin (BSA, Sigma-Aldrich) for 60 minutes. Mouse IgG isotype control and rabbit IgG isotype control (Abcam) were used as negative controls. After washing 3 times in PBS, secondary antibodies Alexa Fluor 488 and Alexa Fluor 594 (Invitrogen) were used in PBS

with 2% BSA for 45 minutes or overnight at 4 ˚C. After washing 3 times in PBS, nuclei were stained using 4',6-Diamidino-2-Phenylindole, Dihydrochloride (DAPI, Thermo Scientific) for 5 minutes. For staining microfluidic devices, all staining steps were performed overnight at 4 ˚C. The cells were imaged using the IX83 inverted microscope or FV3000 confocal microscope (Olympus).

5.2.6 Quantitative real-time PCR

RNA was isolated using RNeasy Plus Mini (QIAGEN) following manufacturer protocols. RNA concentration was measured using NanoDrop 2000 (Thermo Scientific), and cDNA was produced using High Capacity RNA-to-cDNA kit (Life Technologies). TaqMan Universal Master Mix II and TaqMan Gene Expression Assays (Life Technologies) were used to assess gene expression (Table S1). The qPCR reactions were performed using the CFX96 Real-Time PCR Detection System (Bio-Rad). All reactions were performed in duplicate using 18S as an endogenous control gene and analyzed using the comparative C_t method,[233] normalizing the expression level to ECFC-EC using the formula $2^{-\Delta\Delta Ct}$, where $\Delta\Delta C_t$ is described as $[(C_{t\ \text{gene of interest}} - C_{t\ 18S})_{\text{sample of interest}} - (C_{t\ \text{gene of interest}} - C_{t\ 18S})_{\text{ECFC-EC}}]$. The natural log of the ratio of ephrinB2 and EphB4 expression was used to represent arterial versus venous phenotype, as previously described.[286]

5.2.7 Tube formation assay

Undiluted Matrigel was used to coat the bottom of a 96-well plate and polymerized for 1 hour at 37 ˚C. Cells were seeded in EGM-2 with 50 ng/ml VEGF-A at $1x10^4$ cells/well. The formation of tubes was observed over a 72-hour period under a light microscope, and the total tube length was calculated using ImageJ.

5.2.8 Permeability assay

Fibronectin was coated on 12-well Transwell® inserts (Corning) with 0.4 μm membrane pore size and incubated for 1 hour at 37 ˚C. Cells were seeded in EGM-2 with 25 ng/ml VEGF-A at $1.5x10^5$ cells/well and cultured for 3 days with daily medium change. The luminal (top) chamber was loaded with EGM-2 containing 0.1 mg/ml 70 kDa FITC-dextran, which was allowed to diffuse through the cell monolayer into the abluminal (bottom) chamber. The abluminal chamber was loaded with EGM-2 containing 0.1 mg/ml 70 kDa Texas Red-dextran to prevent osmotic pressure formation. Medium volumes of 0.5 and 1.5 ml in the luminal and abluminal chamber, respectively, were used to create equal hydrostatic pressures. After 2 hours, the amount of FITC-dextran in the abluminal chamber was measured using the Infinite 200 PRO microplate reader (Tecan), using a standard curve to interpolate the dextran concentration. The permeability of the system (membrane plus cells) was estimated by using the equation $P_s = (C_A V_A)/(tSC_L)$, where C_A and C_L are the concentrations of the FITC-dextran in the abluminal and luminal chamber, respectively; V_A is the abluminal chamber volume, t is the time, and S is the surface area of the membrane, as previously performed.[287,288] The permeability of the cells was calculated using the equation $1/P_{cells} = 1/P_s - 1/P_m$, where P_m is the permeability of the membrane only.

5.2.9 mCherry-VE-cadherin response to thrombin

A monolayer of CDH5-iPS-ECs were grown to confluence over 48 hours. At the start of the imaging, thrombin was added to the media (3 U/ml final concentration). Images were taken at 3 minute intervals for 45 minutes.

5.2.10 Microfluidic device fabrication and culture

The microfluidic device were fabricated using standard soft lithography and replica molding techniques, as described previously.[230,275,289] The devices were cast of polydimethylsiloxane (PDMS), plasma bonded onto glass slides, and sterilized before cell loading. For shear stress experiments, the devices were coated with fibronectin for 1 hour at 37 ˚C before introducing the cells at $2x10^7$ cells/ml in a total volume of 2 µl. The cells were incubated for 2 hours at 37 ˚C before feeding with E7V medium to flush out unattached cells. For the 3D vasculogenesis assays, the devices were loaded through the side loading channel with $1x10^7$ iPS-EC/ml and $5x10^6$ NHLF/ml in 10 mg/ml fibrinogen (Sigma-Aldrich) and 0.25 U/ml aprotinin (Sigma-Aldrich) in 7.5 µl volume mixed with 0.9 µl of thrombin (3 U/ml final concentration, Sigma-Aldrich). The fibrin gel was polymerized for 15 minutes at 37 ˚C before coating the fluidic lines with fibronectin (100 µg/ml). The devices were incubated for an additional 15 minutes at 37 ˚C before feeding with endothelial growth medium 2 (EGM-2, Lonza) containing 0.25 U/ml aprotinin.

5.2.11 Shear stress response

The iPS-EC were cultured in the microfluidic device for 3 days with daily medium change before exposure to shear stress. COMSOL Multiphysics® was used to model and calculate the flow necessary to achieve the desired average shear stress at the bottom surface of the device.[290] The flow was set using the PHD ULTRA™ syringe pump (Harvard Apparatus) and Tygon® flexible plastic tubing (Saint-Gobain). The shear stress response of the cells was observed under the microscope over the course of 20 hours using the mCherry-VE-Cadherin reporter. The cell perimeter and area were measured using ImageJ and used to calculate the circularity of the cell [4π*area/(perimeter^2)].

5.2.12 Vasculogenesis device analysis

The co-cultured iPS-EC and NHLF were imaged and fed with EGM-2 every 2 days, with alternating interstitial flow directions using a 5 mm H_2O hydrostatic pressure difference across the tissue chambers. Where indicated, SB431542 or sunitinib was supplemented at concentrations of 10 and 0.1 µM, respectively. The barrier function of the vasculature was tested by introducing 70 kDa FITC dextran (Molecular Probes) or fluorescent 1 µm diameter FluoSpheres® microspheres (Molecular Probes) through the media channel. The devices were fixed for immunofluorescence on Day 14. For vessel area quantification, a region of interest (ROI) was selected to outline the chamber using ImageJ (NIH). A Gaussian blur was applied to reduce noise, then the image was thresholded to create a binary image. The erode function was used to further reduce noise, and the area was measured within the ROI. For vessel length quantification, segmented lines were manually traced over the vessels within the ROI. The ratio of the vessel area and the vessel length was used to quantify the average vessel diameter. Each of the 3 chambers within the microfluidic device was analyzed separately, and each experimental condition consisted of at least 3 independent devices. The images were blinded for analysis.

5.2.13 Statistical analysis

All experiments were performed using at least 3 biological replicates. Significance was calculated using one-way analysis of variance (ANOVA) in conjunction with Tukey's multiple comparison test, with *p*-values less than 0.05 considered statistically significant. For the shear stress response, each time point was compared to the control (Time 0) using one-way ANOVA in conjunction with Dunnett's multiple comparison test. For the vessel analysis, two-way ANOVA in conjunction with Sidak's multiple comparison test was used. All results are reported as

mean±SD. Data were compiled, analyzed, and graphed using Microsoft Excel and GraphPad Prism 6.

5.3 Results

5.3.1 Physiological characterization of iPS-EC

The iPS-ECs were differentiated using a monolayer, serum-free differentiation protocol as diagramed (Fig. 5.1A). Day 6 of differentiation yielded a cell population that was 47.1±14.5% $CD31^+$ (Fig. 5.1B-i) prior to magnetic sorting. Following magnetic sorting, the cell population

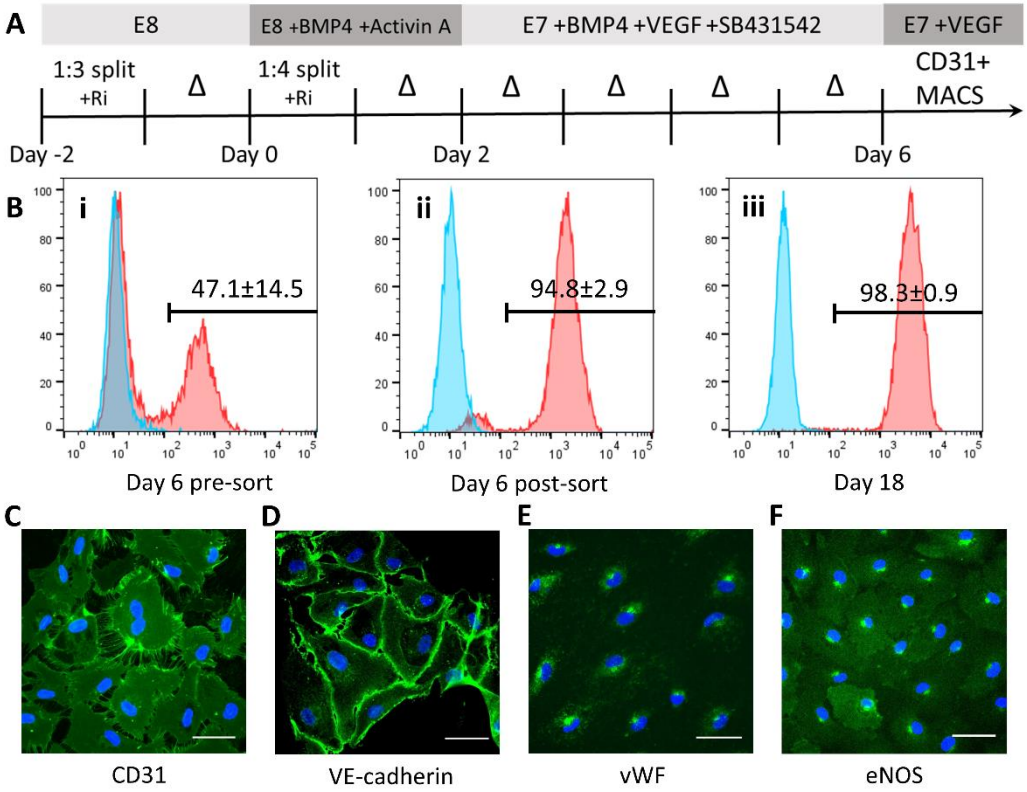

Figure 5.1: Differentiation, isolation, and basic characterization of the iPS-EC. (A) Schematic of the iPS-EC differentiation protocol. The iPS-ECs were isolated using MACS for CD31 on Day 6. (B) The differentiated cells were analyzed for CD31 expression by flow cytometry at Day 6 (i) before sorting, (ii) after MACS sorting, and (iii) 12 days of culture after sorting. Blue = isotype control. The expression of definitive endothelial markers was confirmed using immunofluorescence for (C) CD31, (D) VE-cadherin, (E) vWF, and (F) eNOS. Scale bar: 50 µm.

was purified to 94.8±2.9% $CD31^+$ (Fig. 5.1B-ii). The cells were then grown on fibronectin-coated tissue culture plastic, and an additional 12 days of culture further enriched for iPS-ECs, yielding 98.3±0.9% $CD31^+$ cells (Fig. 5.1B-iii). The sorted iPS-EC population also expressed the endothelial progenitor cell (EPC) marker CD34 (82.4±9.6%), while a small subpopulation stained positively for another EPC marker CD133 (5.90±1.11%) (Fig. A3.1A, A3.1B). The cells did not express the hematopoietic marker CD45 (0.87±0.19%) while staining positively for the mesenchymal marker CD90 (93.2±3.39%), which has previously been shown to be expressed in EPCs (Fig. A3.1C, A3.1D).[291,292] The resulting cells demonstrated a "cobblestone" morphology characteristic of primary endothelial cells including HUAEC, HUVEC, HDLEC, and ECFC-EC (Fig. A3.2A). These cells also had protein expression characteristic of endothelial cells, including expression of CD31 and VE-cadherin that predominantly co-localized at cell junctions (Fig. 5.1C, 1D) and cytoplasmic expression of vWF and eNOS (Fig. 5.1E, 1F). ECFC-ECs were used as a positive control, while isotype IgG antibodies were used as negative controls (Fig. A3.2B, A3.2C). Successful differentiation and isolation was achieved using 2 different human iPSC lines (Fig. A3.2D). The iPS-ECs thawed from Day 8 of differentiation underwent ~7-fold increase in cell number before undergoing senescence (Fig. A3.2E). Culturing the iPS-EC in EGM-2 instead of the E7V medium resulted in observable dedifferentiation of the iPS-EC into cells of stromal- or smooth muscle-like morphology (Fig. A3.2F).

5.3.2 Phenotypic characterization of iPS-ECs

In addition to the definitive endothelial markers, we investigated the expression of markers that define arterial, venous, and lymphatic endothelial phenotype. We specifically measured the ratio of the expression of the putative arterial and venous markers (ephrinB2 and EphB4, respectively).[293,294] The results were compared to primary human endothelial cells of known

phenotype, and normalized to ECFC-ECs as the progenitor endothelial cell control. As expected, the HUAECs had a more arterial-like phenotype compared to ECFC-ECs (higher ratio of ephrinB2 to EphB4), while HUVECs and HDLECs had a more venous-like phenotype (Fig. 5.2A). The iPS-ECs also demonstrated a strong venous phenotype compared to ECFC-ECs (Fig. 5.2A). To distinguish between venous and lymphatic endothelial phenotype, we investigated the

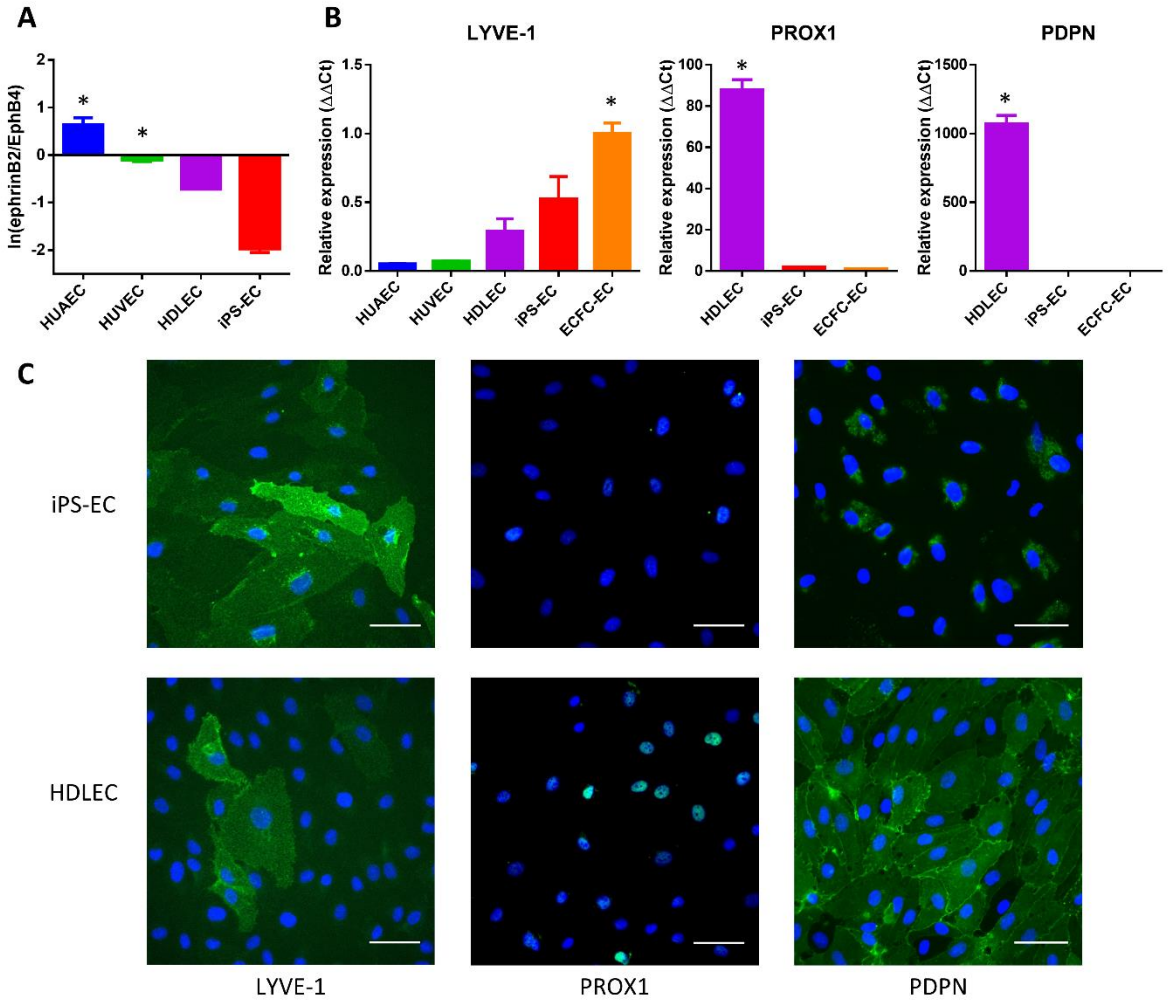

Figure 5.2: Phenotype characterization of iPS-EC. (A) The ratio of ephrinB2 to EphB4 expression levels measured by qPCR. The expression levels are normalized to ECFC-EC, with values greater than 0 indicating a more arterial phenotype than ECFC-EC. HUVEC, HDLEC, and iPS-EC demonstrate a more venous phenotype than ECFC-EC. *p<0.05 compared to iPS-EC. (B) Expression levels of lymphatic markers measured by qPCR, normalized to ECFC-EC. *p<0.05 compared to iPS-EC. (C) Expression of lymphatic markers confirmed by immunofluorescence. The HDLEC stain positively for all 3 markers while the iPS-EC only stain positively for LYVE-1. Blue = DAPI. Scale bar: 50 µm.

expression of 3 different lymphatic endothelial markers: lymphatic vessel endothelial hyaluronan receptor-1 (LYVE-1), Prospero homeobox protein 1 (PROX1), and podoplanin (PDPN). As expected, the HDLECs showed positive expression of all 3 markers (Fig. 5.2B). The iPS-ECs showed low expression of PDPN and PROX1, but showed high expression of LYVE-1 (Fig. 5.2B). A similar expression pattern was observed for the ECFC-ECs (Fig. 5.2B). The expression pattern of the lymphatic markers for iPS-ECs and HDLECs was confirmed using immunofluorescence (Fig. 5.2C).

5.3.3 CDH5-mCherry iPSC line

Using CRISPR/Cas9, we established a mCherry-VE-cadherin reporter iPSC line. The iPS-ECs derived from the CDH5-mCherry iPSC line (CDH5-iPS-EC) demonstrated robust mCherry signal that co-localized to the cell junctions, as well as an accumulation of the signal near the cell nucleus (Fig. 5.3A). Since VE-cadherin is involved in maintaining endothelial barrier function,[295] we investigated whether the fusion protein impacted the permeability of the CDH5-iPS-EC monolayer. Using a Transwell permeability assay, we observed no statistically significant difference in the diffusion of 70 kDa dextran between the CDH5-iPS-ECs, iPS-ECs, and ECFC-ECs (Fig. 5.3B). All 3 EC types demonstrated significantly lower permeability of 70 kDa dextran compared to fibroblasts, with permeability values comparable to previous studies using primary vascular endothelial cells ($4.73 \times 10^{-6} \pm 0.85 \times 10^{-6}$cm/s for CDH5-iPS-EC) (Fig. 5.3B).[287,296] We also studied the ability of the CDH5-iPS-ECs to form tube-like structures on Matrigel (Fig. 5.3C). Again, we observed no statistically significant difference between the CDH5-iPS-ECs, iPS-ECs, and ECFC-ECs (Fig. 5.3D). In addition, we tested the physiological response to the CDH5-iPS-EC to thrombin, which induces EC retraction through the redistribution of VE-cadherin.[297] Time-lapse imaging of the CDH5-iPS-ECs showed dissociation

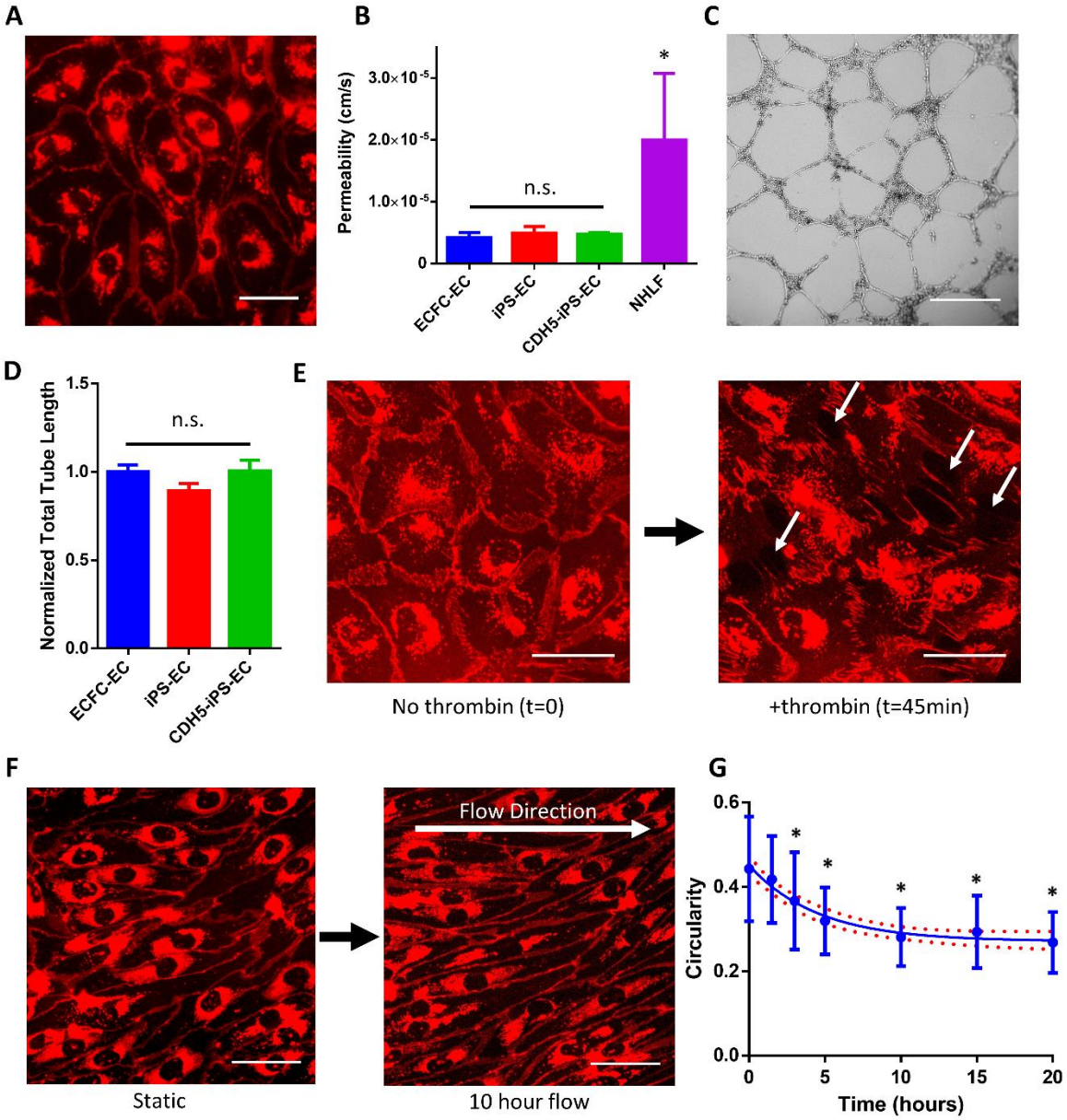

Figure 5.3: The use of CDH5-mCherry iPSC-derived EC (CDH5-iPS-EC). (A) The CDH5-iPS-ECs demonstrate mCherry signal that localizes to cell junctions. (B) The permeability measured by the diffusion of 70 kDa dextran across a cell monolayer. The permeability of CDH5-iPS-EC monolayer is unchanged compared to iPS-EC as well as ECFC-EC. *p<0.05 compared to CDH5-iPS-EC. (C) Representative image of Matrigel tube formation assay for CDH5-iPS-EC. (D) The total tube length normalized to ECFC-EC. No significant differences were observed across the 3 EC types. (E) CDH5-iPS-EC response to thrombin. The mCherry-VE-cadherin disaggregate from cell junctions, resulting in the formation of intercellular gaps (indicated by white arrows). (F) The CDH5-iPS-ECs are used to image the response to shear stress in real time. The cells demonstrate a more elongated morphology over time. (G) The circularity of the CDH5-iPS-EC in response to shear stress is calculated over time. *p<0.05 compared to time 0. Line indicates a one phase decay fit with 95% confidence band. Scale bar: 50 µm (A,E,F), 500 µm (C).

of the mCherry-VE-cadherin signal at cell junctions in response to thrombin, resulting in EC retraction and formation of intercellular gaps (Fig. 5.3E).

5.3.4 iPS-EC response to shear stress

Using the CDH5-iPS-ECs, we investigated the cellular response to an applied shear stress. We utilized a microfluidic device that consisted of microfluidic lines 10 mm in length with cross sectional dimensions of 800 and 100 μm in width and height, respectively. Using finite element modeling to determine the fluid shear stress, we set the fluid flow within the line to produce an average shear stress of 4 dynes/cm^2 (Fig. A3.3). The cells were observed using time-lapse imaging of the mCherry-VE-cadherin signal, and morphological changes were observed over the course of 20 hours (Fig. 5.3E). Using circularity as a morphological index, we observed significant elongation of the cells in response to shear stress (Fig. 5.3F).

5.3.5 3D iPS-EC vascular networks

We next investigated the ability of the CDH5-iPS-ECs to form 3D vascular networks by co-culturing them with fibroblasts in microfluidic devices (Fig. 5.4A). Using the mCherry-VE-cadherin signal to track vessel formation, we observed the development of a robust vessel network over the course of 14 days (Fig. 5.4B, quantitative analysis in Fig. 5.5). The iPS-ECs undergo vacuole formation and aggregate into tube-like structures in the first 48 hours, as previously observed using primary ECs (Fig. A3.4A).[298] The microvessel network connected to the top and bottom microfluidic lines (Fig. 5.4C), enabling the flow of media through the vascular networks without leakage into the surrounding tissue space. The vessels have a complete lumen as confirmed by staining for CD31 and imaging using confocal microscopy (Fig. 5.4D). Co-staining for laminin, a basement membrane protein, we observed the localization of

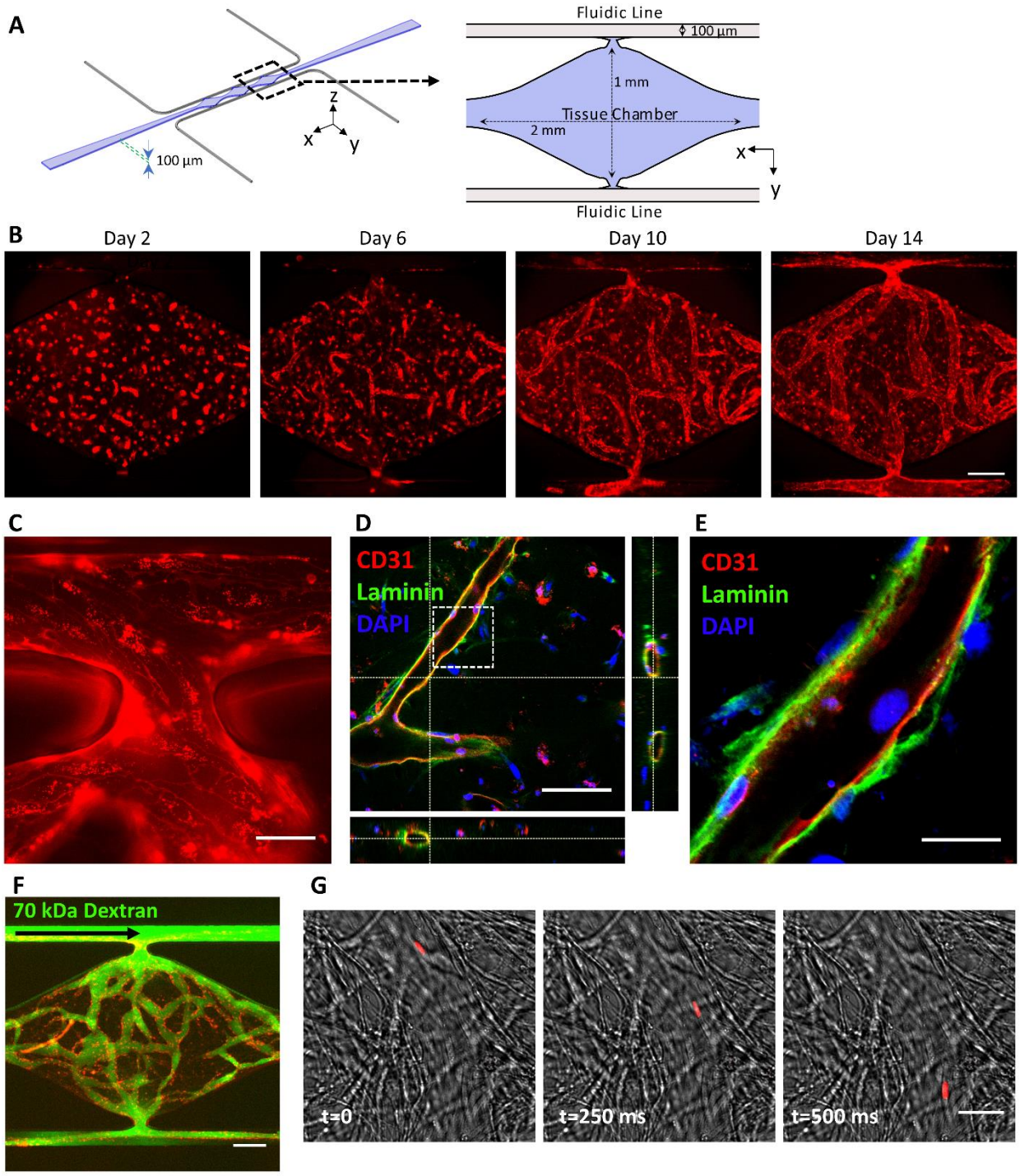

Figure 5.4: 3D culture of iPS-EC in microfluidic devices. (A) Schematic illustration of the microfluidic device. The cell suspension in fibrin is loaded into the tissue chamber region, while media is delivered through the top and bottom fluidic lines. (B) Representative images of the vessel network formation by CDH5-iPS-EC tracked over a period of 14 days. (C) The vessel anastomoses to the top fluidic line as indicated by the continuous CDH5-iPS-EC lining around the opening of the tissue chamber.

(legend continued on next page)

Figure 5.4 (Cont.): (D) The microvessels demonstrate a patent lumen as confirmed by confocal microscopy. The dashed box region: (E) the iPS-ECs deposit laminin as a part of the basement membrane. (F) The vessel network effectively retains 70 kDa dextran introduced through the top fluidic line. (G) 1 µm bead (red) is captured flowing through the vessel. Scale bar: 200 µm (B,F), 50 µm (C), 100 µm (D), 25 µm (E,G).

laminin on the outer wall of the microvessels as outlined by CD31 (Fig. 5.4E). The vascular network demonstrates a physiological barrier function, as they effectively retain fluorescently labeled 70 kDa dextran (Fig. 5.4F). Furthermore, we were able to flow 1 µm beads through the vessels (Fig. 5.4G).

5.3.6 Supplementation of small molecule TGF-β inhibitor

Since TGF-β inhibition has an established effect of enhancing iPS-EC proliferation in monolayer culture,[299] we explored whether TGF-β inhibition also leads to improved vessel network formation. A small molecule TGF-β inhibitor (SB431542) was supplemented into the growth medium, and the vessel formation was compared to the control condition (Fig. 5.5A). The addition of SB431542 resulted in a significant increase in vessel length (26-49%) at all measured time points (Day 6, 10, 14) (Fig. 5.5B). The increase in vessel area (23-57%) was statistically significant for Day 6 and 10, and showed a strong positive trend for Day 14 (p=0.12) (Fig. 5.5C). No statistically significant difference in the average vessel diameter was observed at all 3 time points (Fig. 5.5D).

5.3.7 Vessel response to anti-angiogenic drug

To further demonstrate the utility of the platform, we investigated the effects of the anti-angiogenic drug sunitinib. Sunitinib is a multitargeted tyrosine kinase inhibitor used for cancer treatment due to its anti-angiogenic and anti-tumor activities.[300,301] On Day 6 of culture, sunitinib

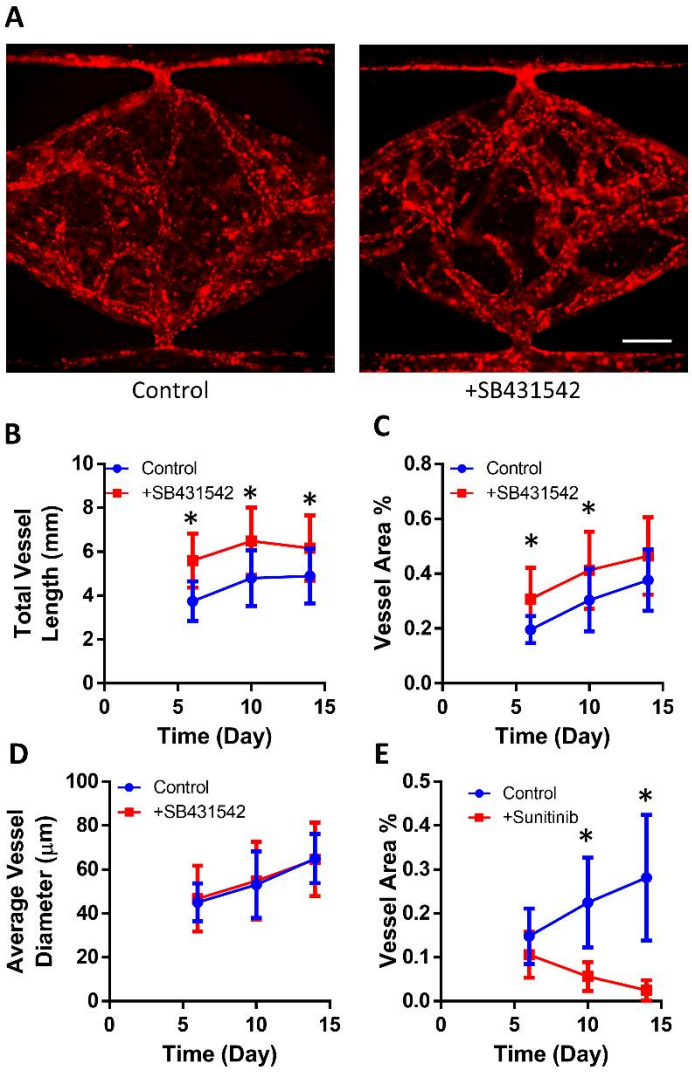

Figure 5.5: Response of iPS-EC vasculature to small molecule inhibitors. (A) Representative CDH5-iPS-EC vessel networks developed at day 14 with or without the supplementation of SB431542 in the growth medium. The addition of SB432542 significantly increased (B) the total vessel length and (C) the total vessel area coverage within the tissue chamber. *p<0.05 compared to control at the given time point. (D) The average vessel diameter is not significantly affected by the addition of SB431542. (E) The total vessel area within the tissue chamber decrease in response to sunitinib treatment. *p<0.05 comparing control versus sunitinib-treated condition at the given time point.

was added to the medium at 100 nM, and we observed statistically significant reduction in the total vessel area compared to control (Fig. 5.5E).

5.4 Discussion

In this study, we characterized critical physiological functions of iPS-ECs using 2D and 3D *in vitro* cultures. The iPS-ECs demonstrated the expression of several definitive endothelial cell markers and maintained this expression pattern even after 12 days of culture in a serum-free medium. We established a novel CDH5-iPS-EC line expressing the mCherry-VE-cadherin fusion protein, which was used to perform live cell imaging at various time points over the course of a

single experiment. The gene expression pattern of the iPS-ECs suggests a venous-like endothelial phenotype compared to ECFC-ECs. The iPS-EC monolayer demonstrates physiological barrier functions, a shear stress response, and the ability to form vessel structures when cultured on Matrigel. In 3D, the iPS-EC are capable of undergoing vasculogenic and angiogenic processes to form robust, perfusable vascular networks. Finally, we demonstrate that the iPS-EC vascular networks are responsive to small molecule inhibitors that have angiogenic or anti-angiogenic effects. Thus, the CDH5-iPS-EC line provides a convenient yet robust model that is consistent with the physiological characteristics of primary ECs. Based on their ability to form 3D perfused vascular networks, we believe iPS-ECs have the potential to be used in a wide range of *in vitro* and *in vivo* tissue engineering applications.

The iPS-EC differentiation protocol utilized here has several advantages compared to several previously established differentiation protocols. The differentiation does not vary in technique from the standard monolayer, feeder-free culture of hPSC, requiring no additional steps for embryoid body formation or suspension culture. The differentiation and maintenance media are serum-free, which minimizes the variability in the differentiation protocol. Bao et al.[302] recently reported the successful differentiation of human iPS-ECs using chemically-defined, albumin-free media and xenogen-free substrate (Synthemax vitronectin). While their reported differentiation efficiency is lower than achieved here (~30% vs. ~45%), further advancements in chemically-defined differentiation protocols could further improve reproducibility and translational applications.

Additionally, selecting an appropriate iPS-EC differentiation strategy requires careful consideration of the intended application and function of the tissue. Whereas the iPS-ECs derived here demonstrated a predominantly venous phenotype, previous studies have reported a

more arterial phenotype, especially when cultured in high concentrations of VEGF-A.[303–305] Other groups have reported an indeterminate phenotype, which may be an indication of the immaturity of the iPS-ECs.[286,306] Differences are likely due to the distinct differentiation protocols utilized by the different research groups, highlighting the sensitivity in differentiating ECs from hPSCs and that further work is needed to better control this process. The expression of LYVE-1 without the expression of other lymphatic markers is consistent with previous findings.[299,306] It has been shown that LYVE-1 expression is not limited to lymphatic ECs,[307] and the lack of expression of PROX1 and PDPN strongly suggests that the iPS-ECs in our study are indeed more venous-like and not lymphatic. It remains to be seen how the phenotype-specific functions of iPS-ECs will influence their potential applications in MPS. In addition to the basic phenotype of the iPS-ECs, it will be critical to consider organ- and tissue-specific functions of endothelial cells in order to further advance the capabilities of MPS to model the *in vivo* microenvironment.[258,282,308]

We established a CDH5-mCherry human iPSC line that can be utilized to generate iPS-ECs expressing an mCherry-VE-cadherin fusion protein. While we did not detect any dysregulation in the CDH5-iPS-EC barrier function or response to thrombin, we observed mCherry signal accumulation around the cell nucleus. We believe that this cytoplasmic mCherry signal is due to VE-cadherin internalization, as VE-cadherin has known mechanisms of endocytosis in response to signaling factors such as VEGF and thrombin.[297,309] Indeed, some of the mCherry signal can be observed entering the cytoplasm of the cell in response to thrombin. Similar observations of signal accumulation were made in previous works using HUVECs that expressed fluorescently-labeled VE-cadherin via lentiviral transduction.[310,311] While efficient, lentiviral systems have significant shortcomings, as the gene encoding the fusion protein is randomly inserted into the

genome and the expression of the protein is forced through a promoter sequence. The CDH5-mCherry iPSC line utilized CRISPR/Cas9 to specifically modify the CDH5 gene; thus, the mCherry signal is only observed in cells that express VE-cadherin using the native promoter. Further genetic modifications can be made on the CDH5-iPSC line to perform mechanistic studies on VE-cadherin and its role in EC physiology and pathophysiology.

While the iPS-ECs formed 3D vessel networks within the microfluidic device, we utilized a relatively high density of iPS-ECs ($1x10^7$ cells/ml) to achieve consistent vascular network formation. We observed that the iPS-ECs loaded at the same concentration as previous experiments using ECFC-ECs ($5x10^6$ cells/ml) resulted in fragmented vessel networks that did not consistently form a continuous vessel network across the top and bottom fluidic lines (Fig. A3.4B). In addition, we observed a large number of iPS-ECs within the device that did not integrate into vessel networks. These data suggest that the iPS-ECs have a limited vasculogenic potential compared to the ECFC-ECs, and that the iPS-EC population may include poorly differentiated cells that have vasculogenic deficiencies. While the iPS-ECs express CD31, additional markers may be necessary to select for a highly vasculogenic iPS-EC subpopulation. For example, neuropilin-1 (NRP-1) is a marker that has been shown to select for a human iPS-EC subpopulation that shows high proliferative capacity and robust vessel network formation *in vivo*.[277,312] Hu et al.[313] recently reported that iPS-ECs differentiated from an iPSC line that originates from ECs (as opposed to fibroblasts) have higher expression of EC markers, suggesting that the cellular origin of the iPSC may also play a role in iPS-EC functionality. Additional studies are necessary to investigate how to enrich for highly vasculogenic iPS-ECs. The data also highlights the inability of the Matrigel tube formation assay to assess vasculogenic

potential of ECs, as no significant difference between the ECFC-ECs and iPS-ECs were detected.

Our investigations of the microvessels formed by the iPS-ECs demonstrate features of a mature vasculature. The microvessels demonstrate a continuous basement membrane that stained positively for laminin, a key ECM protein involved in vessel stabilization and maturation.[314] This is in contrast to the iPS-ECs cultured in a 2D monolayer where laminin staining is discontinuous and localizes around the nucleus (Fig. A3.5), as similarly observed in a previous study.[315] It is also interesting to note that the iPS-ECs in the device were cultured using EGM-2 for 14 days, a condition under which the iPS-ECs cultured in a 2D monolayer showed a propensity to dedifferentiate into cells with a stromal phenotype. These data suggest that the 3D culture of the iPS-ECs in the presence of fibroblasts can enhance the phenotypic commitment of the iPS-ECs. Cytokines released by fibroblasts have been demonstrated as a critical component in the formation of stable microvessels *in vitro*.[266,316] Further studies are required to establish if these cytokines enhance the differentiation and maturation of iPS-ECs.

We demonstrated that the iPS-EC vessel network formation can be improved by the addition of a small molecule TGF-β inhibitor SB431542in the culture medium. SB431542 inhibits TGF-β signaling by blocking activin-like kinase (ALK) receptors[317] and is commonly used to enhance EC differentiation and expansion.[285,286,299,306,318] Using 2D tube formation assays, previous studies have shown that the addition of SB431542 in the culture medium can enhance area of coverage and total branch number of iPS-ECs.[306,318] A similar response is observed in our 3D vasculogenesis assay using iPS-ECs, as the addition of SB431542 results in significant increases in both the total vessel area and the total vessel length. No significant increase in the average

vessel diameter was observed, indicating that the increased branching of the vasculature leads to the increased total vessel area.

In conclusion, this study advances the current understanding of iPS-ECs and their utility in creating advanced MPS. The iPS-ECs demonstrate physiological functions in both 2D and 3D culture, and can be manipulated to create robust microvascular networks in microfluidic devices. By understanding the basic characteristics and behavior of iPS-ECs, the tissue engineering community can make informed decisions on the integration of iPS-ECs in advancing MPS as well as other tissue engineering platforms.

Chapter Authors

Yosuke Kurokawa, Rose T. Yin, Michael R. Shang, Venktesh S. Shirure, Monica L. Moya, Steven C. George

Final publication is available from Mary Ann Liebert, Inc., publishers
http://dx.doi.org/10.1089/ten.tec.2017.0133

Chapter 6: Challenges and Opportunities

Over the last 5 years, significant advancements have been made in the field of cardiac microphysiological systems and its applicability for *in vitro* drug screening. Notwithstanding, several key challenges still remain before researchers can fully realize the potential of human iPSC-derived cardiovascular cells for drug screening applications.

6.1 Integration of Organ Systems

Integrating multiple organ systems has been a long-term goal of the Microphysiological Systems Program.[10] Such integrated platforms, termed "human-on-a-chip", can provide information on a compound of interest that is not possible to obtain using simpler *in vitro* platforms. For example, the integration of a liver microphysiological model will be significant for understanding the effects of the drug metabolites.[319] Researchers also envision using an integrated platform to study the pharmacokinetics of how a drug of interest will be distributed throughout the body.[320] Such an *in vitro* platform can complement computational models and animal studies to better predict drug safety and efficacy in human patients. Such a system also has higher physiological relevance by recapitulating the interaction between different organ systems, which may be critical for understanding specific drug mechanisms.

Several critical challenges exist for creating integrated microphysiological platforms. One is the choice of growth medium. Most commercially available growth media have been optimized for a small subset of cell types, whereas a universal medium that can support the physiological function of all the integrated organ systems is desirable.[321] The scaling of the integrated organ systems in terms of their physiological function must also be optimized so as to mimic the human body.[260] The technical challenges of connecting microfluidic systems with the proper

fluidics to support the organ systems must also be addressed to increase throughput of such platforms for drug screening applications.

6.2 Disease Modeling

The ability of microphysiological systems to recapitulate disease states will be critical for drug development. In the field of cardiovascular disease modeling, significant progress has been made using cardiomyocytes differentiated from patient-derived iPSCs carrying a disease-related genetic mutation. Many monogenic diseases, such as dilated cardiomyopathy and long-QT syndrome, can be recapitulated at the single cardiomyocyte level, and new molecular targets and therapeutic options are being proposed using such disease models.[322–324] However, more complex diseases, such as atrial fibrillation and hypertension, are difficult to model due to the unknown nature of all the contributing factors that cause the disease in patients. As more advanced microphysiological systems develop, it may be possible to use these platforms to mechanistically probe stimuli that induce the disease phenotype.

More advanced disease models also open the potential for phenotypic drug screening, which focuses on identifying compounds that modulate the disease-linked phenotype. Phenotypic drug screening was commonly performed in animal models before the popularization of target-based drug screening, and has recently regained use in part due to advancements in disease models.[325] One of the critical components to a phenotypic drug screening is a physiologically-relevant model of the disease.[326] Using such platforms, compounds of potentially novel mechanisms can be identified that effectively correct the disease phenotype.

6.3 Patient-Specific Drug Screening

The concept of patient-specific drug screening, also referred to as personalized medicine or precision medicine, has gained significant traction over the past decade, as studies have shown that many drugs have different responses in patients with different genetic backgrounds.[327] The ability to use multiple iPSC lines to represent a varied genetic background in patients holds a strong potential for patient-specific drug screening to become a reality. Recent research findings have proven the concept of personalized medicine to be effective in predicting cardiovascular drug response. Burridge et al.[215] demonstrated that iPS-CMs recapitulated doxorubicin-induced cardiotoxicity at a patient-specific level: iPS-CMs from patients who displayed symptoms of doxorubicin-induced cardiotoxicity had lower tolerance to doxorubicin *in vitro*. Matsa et al.[328] demonstrated that reprogramming and differentiation of patient-derived cells into iPS-CMs preserve the patient's genetic background and that their transcriptomic profile can be used to predict drug-induced cardiotoxicity. Stillitano et al.[208] demonstrated that iPS-CMs accurately predicts changes in electrophysiology induced by the drug sotalol, showing a good match to the observed patient response.

Several challenges remain to realize the potential of patient-specific drug screening. The associated cost of utilizing patient-specific models instead of a single model must be addressed. While the potential benefits to the patients are immense, the personalized medicine approach may not offer enough to pharmaceutical companies to offset the increased cost, especially for rare-diseases that may only benefit a small subpopulation.[329] It also remains to be seen if certain diseases can be predicted at the patient-specific level. While genome-wide association studies have helped identify common mutations that puts patients at risk for certain diseases, non-heritable diseases have no known genetic profile that predisposes a person to the disease.[330] As

alluded to in Chapter 4, it remains to be seen if trastuzumab-related cardiotoxicity can be predicted at the patient-specific level. Since most of the work presented in this dissertation was performed using human iPSC-derived cells, it is possible to add components of patient-specific drug screening into the presented platforms. However, considerable progress in the science of personalized medicine and cost reduction of the associated methods must be achieved before the practice becomes a standard of care at the clinical level.

6.4 Conclusion

Microphysiological systems have the potential to resolve some of the critical issues in drug development today. As we create more advanced models of the human body, we can improve our understanding of human physiology and pathophysiology which in turn guides the drug development process. The use of iPSCs open doors to disease- and patient-specific drug screening applications, which have transformative potential in the pharmaceutical industry. Strong interest and funding from academia, industry, and government agencies have been critical for the rapid development of microphysiological systems, and continued support will be required to realize commercial success of the technology. Many challenges remain, and it will be exciting to see new research findings and technological breakthroughs address these challenges in the future.

References

1. DiMasi, J. A., Grabowski, H. G. & Hansen, R. W. Innovation in the pharmaceutical industry: New estimates of R&D costs. *J. Health Econ.* **47,** 20–33 (2016).

2. Sertkaya, A., Wong, H.-H., Jessup, A. & Beleche, T. Key cost drivers of pharmaceutical clinical trials in the United States. *Clin. Trials* **13,** 117–126 (2016).

3. Avorn, J. The $2.6 Billion Pill — Methodologic and Policy Considerations. *N. Engl. J. Med.* **372,** 1877–1879 (2015).

4. Kesselheim, A. S., Avorn, J. & Sarpatwari, A. The High Cost of Prescription Drugs in the United States. *JAMA* **316,** 858 (2016).

5. Paul, S. M. *et al.* How to improve R&D productivity: the pharmaceutical industry's grand challenge. *Nat. Rev. Drug Discov.* **9,** 203–214 (2010).

6. Scannell, J. W., Blanckley, A., Boldon, H. & Warrington, B. Diagnosing the decline in pharmaceutical R&D efficiency. *Nat. Rev. Drug Discov.* **11,** 191–200 (2012).

7. Naci, H., Carter, A. W. & Mossialos, E. Why the drug development pipeline is not delivering better medicines. *BMJ* **5542,** h5542 (2015).

8. Arrowsmith, J. & Miller, P. Trial Watch: Phase II and Phase III attrition rates 2011–2012. *Nat. Rev. Drug Discov.* **12,** 569–569 (2013).

9. Horrobin, D. F. Opinion: Modern biomedical research: an internally self-consistent universe with little contact with medical reality? *Nat. Rev. Drug Discov.* **2,** 151–154 (2003).

10. Sutherland, M. L., Fabre, K. M. & Tagle, D. a. The National Institutes of Health Microphysiological Systems Program focuses on a critical challenge in the drug discovery pipeline. *Stem Cell Res. Ther.* **4,** I1 (2013).

11. Global status report on noncommunicable diseases 2010. *World Health Organization* (2011). Available at: http://www.who.int/nmh/publications/ncd_report_full_en.pdf. (Accessed: 13th January 2015)

12. Shah, R. R. Can pharmacogenetics help rescue drugs withdrawn from the market? *Pharmacogenomics* **7,** 889–908 (2006).

13. Chen, M. H. Cardiac dysfunction induced by novel targeted anticancer therapy: An emerging issue. *Curr. Cardiol. Rep.* **11,** 167–174 (2009).

14. Ewer, M. S. & Ewer, S. M. Cardiotoxicity of anticancer treatments: what the cardiologist needs to know. *Nat. Rev. Cardiol.* **7,** 564–575 (2010).

15. Kaese, S. & Verheule, S. Cardiac electrophysiology in mice: a matter of size. *Front. Physiol.* **3,** 345 (2012).

16. Gintant, G. An evaluation of hERG current assay performance: Translating preclinical safety studies to clinical QT prolongation. *Pharmacol. Ther.* **129,** 109–119 (2011).

17. Mercola, M., Colas, A. & Willems, E. Induced pluripotent stem cells in cardiovascular drug discovery. *Circ. Res.* **112,** 534–548 (2013).

18. *Anatomy & Physiology*. (OpenStax College, 2013).

19. Severs, N. J. The cardiac gap junction and intercalated disc. *Int. J. Cardiol.* **26,** 137–173 (1990).

20. Braam, S. R., Passier, R. & Mummery, C. L. Cardiomyocytes from human pluripotent stem cells in regenerative medicine and drug discovery. *Trends Pharmacol. Sci.* **30,** 536–545 (2009).

21. Leyton-Mange, J. S. & Milan, D. J. Pluripotent Stem Cells as a Platform for Cardiac Arrhythmia Drug Screening. *Curr. Treat. Options Cardiovasc. Med.* **16,** 334 (2014).

22. Caspi, O. *et al.* In vitro electrophysiological drug testing using human embryonic stem cell derived cardiomyocytes. *Stem Cells Dev.* **18,** 161–172 (2009).

23. Liang, P. *et al.* Drug screening using a library of human induced pluripotent stem cell-derived cardiomyocytes reveals disease-specific patterns of cardiotoxicity. *Circulation* **127,** 1677–91 (2013).

24. Navarrete, E. G. *et al.* Screening Drug-Induced Arrhythmia Using Human Induced Pluripotent Stem Cell-Derived Cardiomyocytes and Low-Impedance Microelectrode Arrays. *Circulation* **128,** S3–S13 (2013).

25. Sirenko, O. *et al.* Multiparameter in vitro assessment of compound effects on cardiomyocyte physiology using iPSC cells. *J. Biomol. Screen.* **18,** 39–53 (2013).

26. Yan, P. *et al.* Palette of fluorinated voltage-sensitive hemicyanine dyes. *Proc. Natl. Acad. Sci. U. S. A.* **109,** 20443–8 (2012).

27. Jonsson, M. K. B., Wang, Q.-D. & Becker, B. Impedance-Based Detection of Beating Rhythm and Proarrhythmic Effects of Compounds on Stem Cell-Derived Cardiomyocytes. *Assay Drug Dev. Technol.* **9,** 589–599 (2011).

28. Nguemo, F. *et al.* In vitro model for assessing arrhythmogenic properties of drugs based on high-resolution impedance measurements. *Cell. Physiol. Biochem.* **29,** 819–832 (2012).

29. Itzhaki, I. *et al.* Modelling the long QT syndrome with induced pluripotent stem cells. *Nature* **471,** 225–9 (2011).

30. Matsa, E. *et al.* Drug evaluation in cardiomyocytes derived from human induced pluripotent stem cells carrying a long QT syndrome type 2 mutation. *Eur. Heart J.* **32,** 952–962 (2011).

31. Moretti, A. *et al.* Patient-specific induced pluripotent stem-cell models for long-QT

syndrome. *N. Engl. J. Med.* **363,** 1397–1409 (2010).

32. Chi, K. R. Revolution dawning in cardiotoxicity testing. *Nat. Rev. Drug Discov.* **12,** 565–567 (2013).

33. Robertson, C., Tran, D. D. & George, S. C. Concise review: Maturation phases of human pluripotent stem cell-derived cardiomyocytes. *Stem Cells* **31,** 829–837 (2013).

34. Sheng, C. C. & Hong, C. C. Pluripotent Stem Cells to Model Human Cardiac Diseases. *Methods Mol. Biol.* **997,** 149–161 (2013).

35. Lundy, S. D., Zhu, W.-Z., Regnier, M. & Laflamme, M. a. Structural and Functional Maturation of Cardiomyocytes Derived from Human Pluripotent Stem Cells. *Stem Cells Dev.* **22,** (2013).

36. Lee, Y.-K. *et al.* Calcium Homeostasis in Human Induced Pluripotent Stem Cell-Derived Cardiomyocytes. *Stem Cell Rev. Reports* **7,** 976–986 (2011).

37. Shinozawa, T., Imahashi, K., Sawada, H., Furukawa, H. & Takami, K. Determination of appropriate stage of human-induced pluripotent stem cell-derived cardiomyocytes for drug screening and pharmacological evaluation in vitro. *J. Biomol. Screen.* **17,** 1192–203 (2012).

38. Yang, X., Pabon, L. & Murry, C. E. Engineering adolescence: maturation of human pluripotent stem cell-derived cardiomyocytes. *Circ. Res.* **114,** 511–23 (2014).

39. Gerdes, A. M. *et al.* Structural remodeling of cardiac myocytes in patients with ischemic cardiomyopathy. *Circulation* **86,** 426–430 (1992).

40. Bursac, N., Parker, K. K., Iravanian, S. & Tung, L. Cardiomyocyte cultures with controlled macroscopic anisotropy: a model for functional electrophysiological studies of cardiac muscle. *Circ. Res.* **91,** e45–e54 (2002).

41. McDevitt, T. C. *et al.* In vitro generation of differentiated cardiac myofibers on micropatterned laminin surfaces. *J. Biomed. Mater. Res.* **60,** 472–479 (2002).

42. Grosberg, A., Alford, P. W., McCain, M. L. & Parker, K. K. Ensembles of engineered cardiac tissues for physiological and pharmacological study: Heart on a chip. *Lab Chip* **11,** 4165 (2011).

43. McCain, M. L., Sheehy, S. P., Grosberg, A., Goss, J. A. & Parker, K. K. Recapitulating maladaptive, multiscale remodeling of failing myocardium on a chip. *Proc. Natl. Acad. Sci. U. S. A.* **110,** 9770–5 (2013).

44. McCain, M. L., Agarwal, A., Nesmith, H. W., Nesmith, A. P. & Parker, K. K. Micromolded gelatin hydrogels for extended culture of engineered cardiac tissues. *Biomaterials* 1–10 (2014). doi:10.1016/j.biomaterials.2014.03.052

45. Wang, G. *et al.* Modeling the mitochondrial cardiomyopathy of Barth syndrome with induced pluripotent stem cell and heart-on-chip technologies. *Nat. Med.* **20,** 616–623

(2014).

46. Wang, P. Y., Yu, J., Lin, J. H. & Tsai, W. B. Modulation of alignment, elongation and contraction of cardiomyocytes through a combination of nanotopography and rigidity of substrates. *Acta Biomater.* **7,** 3285–3293 (2011).

47. Chen, A. *et al.* Shrink-film configurable multiscale wrinkles for functional alignment of human embryonic stem cells and their cardiac derivatives. *Adv. Mater.* **23,** 5785–5791 (2011).

48. Kim, D.-H. *et al.* Nanoscale cues regulate the structure and function of macroscopic cardiac tissue constructs. *Proc. Natl. Acad. Sci. U. S. A.* **107,** 565–570 (2010).

49. Rockwood, D. N., Akins, R. E., Parrag, I. C., Woodhouse, K. a. & Rabolt, J. F. Culture on electrospun polyurethane scaffolds decreases atrial natriuretic peptide expression by cardiomyocytes in vitro. *Biomaterials* **29,** 4783–4791 (2008).

50. Badie, N. & Bursac, N. Novel micropatterned cardiac cell cultures with realistic ventricular microstructure. *Biophys. J.* **96,** 3873–3885 (2009).

51. Chen, A. *et al.* Integrated platform for functional monitoring of biomimetic heart sheets derived from human pluripotent stem cells. *Biomaterials* **35,** 675–683 (2014).

52. Griffith, L. G. & Swartz, M. a. Capturing complex 3D tissue physiology in vitro. *Nat. Rev. Mol. Cell Biol.* **7,** 211–224 (2006).

53. Horning, J. L. *et al.* 3-D tumor model for in vitro evaluation of anticancer drugs. *Mol. Pharm.* **5,** 849–862 (2008).

54. Howes, A. L. *et al.* The phosphatidylinositol 3-kinase inhibitor, PX-866, is a potent inhibitor of cancer cell motility and growth in three-dimensional cultures. *Mol. Cancer Ther.* **6,** 2505–2514 (2007).

55. Khetani, S. R. & Bhatia, S. N. Microscale culture of human liver cells for drug development. *Nat. Biotechnol.* **26,** 120–126 (2008).

56. Schyschka, L. *et al.* Hepatic 3D cultures but not 2D cultures preserve specific transporter activity for acetaminophen-induced hepatotoxicity. *Arch. Toxicol.* **87,** 1581–1593 (2013).

57. Roth, A. & Singer, T. The application of 3D cell models to support drug safety assessment: Opportunities & challenges. *Adv. Drug Deliv. Rev.* **69–70,** 179–189 (2014).

58. Carrier, R. L. *et al.* Cardiac tissue engineering: Cell seeding, cultivation parameters, and tissue construct characterization. *Biotechnol. Bioeng.* **64,** 580–589 (1999).

59. Lee, E. J., Kim, D. E., Azeloglu, E. U. & Costa, K. D. Engineered cardiac organoid chambers: toward a functional biological model ventricle. *Tissue Eng. Part A* **14,** 215–25 (2008).

60. Shapira-Schweitzer, K., Habib, M., Gepstein, L. & Seliktar, D. A photopolymerizable

hydrogel for 3-D culture of human embryonic stem cell-derived cardiomyocytes and rat neonatal cardiac cells. *J. Mol. Cell. Cardiol.* **46,** 213–224 (2009).

61. Eschenhagen, T. *et al.* Three-dimensional reconstitution of embryonic cardiomyocytes in a collagen matrix: a new heart muscle model system. *FASEB J.* **11,** 683–694 (1997).

62. Boudou, T., Legant, W. & Chen, C. A microfabricated platform to measure and manipulate the mechanics of engineered cardiac microtissues. *Tissue Eng. Part A* **18,** 910–919 (2011).

63. Hansen, A. *et al.* Development of a drug screening platform based on engineered heart tissue. *Circ. Res.* **107,** 35–44 (2010).

64. Schaaf, S. *et al.* Human engineered heart tissue as a versatile tool in basic research and preclinical toxicology. *PLoS One* **6,** (2011).

65. Turnbull, I. C. *et al.* Advancing functional engineered cardiac tissues toward a preclinical model of human myocardium. *FASEB J.* **28,** 644–654 (2014).

66. Kensah, G. *et al.* Murine and human pluripotent stem cell-derived cardiac bodies form contractile myocardial tissue in vitro. *Eur. Heart J.* **34,** 1134–46 (2013).

67. Tulloch, N. L. *et al.* Growth of engineered human myocardium with mechanical loading and vascular coculture. *Circ. Res.* **109,** 47–59 (2011).

68. Zhang, D. *et al.* Tissue-engineered cardiac patch for advanced functional maturation of human ESC-derived cardiomyocytes. *Biomaterials* **34,** 5813–5820 (2013).

69. Radisic, M. *et al.* Functional assembly of engineered myocardium by electrical stimulation of cardiac myocytes cultured on scaffolds. *Proc. Natl. Acad. Sci. U. S. A.* **101,** 18129–18134 (2004).

70. Nunes, S. S. *et al.* Biowire: a platform for maturation of human pluripotent stem cell-derived cardiomyocytes. *Nat. Methods* **10,** 781–7 (2013).

71. Miklas, J. W. *et al.* Bioreactor for modulation of cardiac microtissue phenotype by combined static stretch and electrical stimulation. *Biofabrication* **6,** 24113 (2014).

72. Hirt, M. N. *et al.* Functional improvement and maturation of rat and human engineered heart tissue by chronic electrical stimulation. *J. Mol. Cell. Cardiol.* **74,** 151–161 (2014).

73. Zwi, L. *et al.* Cardiomyocyte differentiation of human induced pluripotent stem cells. *Circulation* **120,** 1513–1523 (2009).

74. Nguyen, D. C. *et al.* Microscale generation of cardiospheres promotes robust enrichment of cardiomyocytes derived from human pluripotent stem cells. *Stem cell reports* **3,** 260–8 (2014).

75. Beauchamp, P. *et al.* Development and characterization of a scaffold-free 3D spheroid model of iPSC-derived human cardiomyocytes. *Tissue Eng. Part C Methods* **10,**

150210034755008 (2015).

76. Zhu, R. *et al.* Physical developmental cues for the maturation of human pluripotent stem cell-derived cardiomyocytes. *Stem Cell Res. Ther.* **5,** 117 (2014).

77. Mathur, A. *et al.* Human iPSC-based Cardiac Microphysiological System For Drug Screening Applications. *Sci. Rep.* **5,** 8883 (2015).

78. Hattori, F. *et al.* Nongenetic method for purifying stem cell-derived cardiomyocytes. *Nat. Methods* **7,** 61–6 (2010).

79. Tohyama, S. *et al.* Distinct metabolic flow enables large-scale purification of mouse and human pluripotent stem cell-derived cardiomyocytes. *Cell Stem Cell* **12,** 127–37 (2013).

80. Anderson, D. *et al.* Transgenic enrichment of cardiomyocytes from human embryonic stem cells. *Mol. Ther.* **15,** 2027–2036 (2007).

81. Tian, Y. & Morrisey, E. E. Importance of myocyte-nonmyocyte interactions in cardiac development and disease. *Circ. Res.* **110,** 1023–1034 (2012).

82. Kim, C. *et al.* Non-cardiomyocytes influence the electrophysiological maturation of human embryonic stem cell-derived cardiomyocytes during differentiation. *Stem Cells Dev.* **19,** 783–795 (2010).

83. Berg, E. L., Hsu, Y. C. & Lee, J. a. Consideration of the cellular microenvironment: Physiologically relevant co-culture systems in drug discovery. *Adv. Drug Deliv. Rev.* **69–70,** 190–204 (2014).

84. Shah, A. M. Paracrine modulation of heart cell function by endothelial cells. *Cardiovasc. Res.* **31,** 847–867 (1996).

85. Hsieh, P. P. C. H., Davis, M. M. E., Lisowski, L. K. & Lee, R. T. Endothelial-cardiomyocyte interactions in cardiac development and repair. *Annu. Rev. Physiol.* **68,** 51–66 (2006).

86. Brutsaert, D. L. Cardiac Endothelial-Myocardial Signaling: Its Role in Cardiac Growth, Contractile Performance, and Rhythmicity. *Physiol. Rev.* **83,** 59–115 (2003).

87. Parodi, E. M. & Kuhn, B. Signalling between microvascular endothelium and cardiomyocytes through neuregulin. *Cardiovasc. Res.* **102,** 194–204 (2014).

88. Meyer, D. & Birchmeier, C. Multiple essential functions of neuregulin in development. *Nature* **378,** 386–390 (1995).

89. Gassmann, M. *et al.* Aberrant neural and cardiac development in mice lacking the ErbB4 neuregulin receptor. *Nature* **378,** 390–394 (1995).

90. Lee, K. F. *et al.* Requirement for neuregulin receptor erbB2 in neural and cardiac development. *Nature* **378,** 394–398 (1995).

91. Zhu, W.-Z. *et al.* Neuregulin/ErbB Signaling Regulates Cardiac Subtype Specification in Differentiating Human Embryonic Stem Cells. *Circ. Res.* **107,** 776–786 (2010).

92. Iglesias-García, O. *et al.* Neuregulin-1β Induces Mature Ventricular Cardiac Differentiation from Induced Pluripotent Stem Cells Contributing to Cardiac Tissue Repair. *Stem Cells Dev.* **24,** 484–496 (2015).

93. Slamon, D. J. *et al.* Use of chemotherapy plus a monoclonal antibody against HER2 for metastatic breast cancer that overexpresses HER2. *N. Engl. J. Med.* **344,** 783–92 (2001).

94. Feldman, A. M., Lorell, B. H. & Reis, S. E. Trastuzumab in the Treatment of Metastatic Breast Cancer : Anticancer Therapy Versus Cardiotoxicity. *Circulation* **102,** 272–274 (2000).

95. Sawyer, D. B., Zuppinger, C., Miller, T. A., Eppenberger, H. M. & Suter, T. M. Modulation of anthracycline-induced myofibrillar disarray in rat ventricular myocytes by neuregulin-1beta and anti-erbB2: potential mechanism for trastuzumab-induced cardiotoxicity. *Circulation* **105,** 1551–4 (2002).

96. Zhao, Y. *et al.* Neuregulins Promote Survival and Growth of Cardiac Myocytes. *J. Biol. Chem.* **273,** 10261–10269 (1998).

97. Hedhli, N. *et al.* Endothelium-derived neuregulin protects the heart against ischemic injury. *Circulation* **123,** 2254–62 (2011).

98. Bersell, K., Arab, S., Haring, B. & Kühn, B. Neuregulin1/ErbB4 Signaling Induces Cardiomyocyte Proliferation and Repair of Heart Injury. *Cell* **138,** 257–270 (2009).

99. Eldridge, S. *et al.* Examining the protective role of ErbB2 modulation in human-induced pluripotent stem cell-derived cardiomyocytes. *Toxicol. Sci.* **141,** 547–59 (2014).

100. Vasti, C. & Hertig, C. M. Neuregulin-1/erbB activities with focus on the susceptibility of the heart to anthracyclines. *World J. Cardiol.* **6,** 653–662 (2014).

101. Champion, H. C. *et al.* Modulation of In Vivo Cardiac Function by Myocyte-Specific Nitric Oxide Synthase-3. *Circ. Res.* **94,** 657–663 (2004).

102. Gödecke, a *et al.* Inotropic response to beta-adrenergic receptor stimulation and anti-adrenergic effect of ACh in endothelial NO synthase-deficient mouse hearts. *J. Physiol.* **532,** 195–204 (2001).

103. Lemmens, K., Fransen, P., Sys, S. U., Brutsaert, D. L. & De Keulenaer, G. W. Neuregulin-1 Induces a Negative Inotropic Effect in Cardiac Muscle: Role of Nitric Oxide Synthase. *Circulation* **109,** 324–326 (2004).

104. Mebazaa, a *et al.* Paracrine effects of endocardial endothelial cells on myocyte contraction mediated via endothelin. *Am. J. Physiol.* **265,** H1841–H1846 (1993).

105. Lüscher, T. F. *et al.* Interaction between endothelin-1 and endothelium-derived relaxing factor in human arteries and veins. *Circ. Res.* **66,** 1088–1094 (1990).

106. Lemmens, K., Segers, V. F. M., Demolder, M. & De Keulenaer, G. W. Role of neuregulin-1/ErbB2 signaling in endothelium-cardiomyocyte cross-talk. *J. Biol. Chem.* **281,** 19469–19477 (2006).

107. Caspi, O. *et al.* Tissue engineering of vascularized cardiac muscle from human embryonic stem cells. *Circ. Res.* **100,** 263–72 (2007).

108. Sekine, H. *et al.* Endothelial cell coculture within tissue-engineered cardiomyocyte sheets enhances neovascularization and improves cardiac function of ischemic hearts. *Circulation* **118,** S145-52 (2008).

109. Narmoneva, D. a, Vukmirovic, R., Davis, M. E., Kamm, R. D. & Lee, R. T. Endothelial cells promote cardiac myocyte survival and spatial reorganization: implications for cardiac regeneration. *Circulation* **110,** 962–8 (2004).

110. Burridge, P. W. *et al.* Multi-cellular interactions sustain long-term contractility of human pluripotent stem cell-derived cardiomyocytes. *Am. J. Transl. Res.* **6,** 724–735 (2014).

111. Stevens, K. R. *et al.* Physiological function and transplantation of scaffold-free and vascularized human cardiac muscle tissue. *Proc. Natl. Acad. Sci. U. S. A.* **106,** 16568–16573 (2009).

112. Vollert, I. *et al.* In vitro perfusion of engineered heart tissue through endothelialized channels. *Tissue Eng. Part A* **20,** 854–63 (2014).

113. Huh, D. *et al.* Reconstituting organ-level lung functions on a chip. *Science* **328,** 1662–1668 (2010).

114. Guzzardi, M. A., Vozzi, F. & Ahluwalia, A. D. Study of the crosstalk between hepatocytes and endothelial cells using a novel multicompartmental bioreactor: a comparison between connected cultures and cocultures. *Tissue Eng. Part A* **15,** 3635–3644 (2009).

115. Hendrickx, J. *et al.* Molecular diversity of cardiac endothelial cells in vitro and in vivo. *Physiol. Genomics* **19,** 198–206 (2004).

116. Kusuma, S. *et al.* Self-organized vascular networks from human pluripotent stem cells in a synthetic matrix. *Proc. Natl. Acad. Sci. U. S. A.* **110,** 12601–6 (2013).

117. Orlova, V. V *et al.* Generation, expansion and functional analysis of endothelial cells and pericytes derived from human pluripotent stem cells. *Nat. Protoc.* **9,** 1514–31 (2014).

118. Souders, C. A., Bowers, S. L. K. & Baudino, T. A. Cardiac fibroblast: The renaissance cell. *Circulation Research* **105,** 1164–1176 (2009).

119. Adler, C. P., Ringlage, W. P. & Böhm, N. DNS-Gehalt and Zellzahl in Herz and Leber von Kindern. *Pathol. - Res. Pract.* **172,** 25–41 (1981).

120. Grove, D., Zak, R., Nair, K. G. & Aschenbrenner, V. Biochemical correlates of cardiac hypertrophy. IV. Observations on the cellular organization of growth during myocardial

hypertrophy in the rat. *Circ. Res.* **25,** 473–485 (1969).

121. Camelliti, P., Borg, T. K. & Kohl, P. Structural and functional characterisation of cardiac fibroblasts. *Cardiovasc. Res.* **65,** 40–51 (2005).

122. Bowers, S. L. K., Borg, T. K. & Baudino, T. a. The dynamics of fibroblast-myocyte-capillary interactions in the heart. *Ann. N. Y. Acad. Sci.* **1188,** 143–152 (2010).

123. Rienks, M., Papageorgiou, A. P., Frangogiannis, N. G. & Heymans, S. Myocardial extracellular matrix: An ever-changing and diverse entity. *Circ. Res.* **114,** 872–888 (2014).

124. Marijianowski, M. M., van der Loos, C. M., Mohrschladt, M. F. & Becker, A. E. The neonatal heart has a relatively high content of total collagen and type I collagen, a condition that may explain the less compliant state. *J. Am. Coll. Cardiol.* **23,** 1204–1208 (1994).

125. Kühn, B. *et al.* Periostin induces proliferation of differentiated cardiomyocytes and promotes cardiac repair. *Nat. Med.* **13,** 962–969 (2007).

126. Fan, D., Takawale, A., Lee, J. & Kassiri, Z. Cardiac fibroblasts, fibrosis and extracellular matrix remodeling in heart disease. *Fibrogenesis Tissue Repair* **5,** 15 (2012).

127. Merna, N. *et al.* Differential β 3 Integrin Expression Regulates the Response of Human Lung and Cardiac Fibroblasts to Extracellular Matrix and Its Components. *Tissue Eng. Part A* (2015). doi:10.1089/ten.tea.2014.0337

128. Carver, W., Nagpal, M. L., Nachtigal, M., Borg, T. K. & Terracio, L. Collagen expression in mechanically stimulated cardiac fibroblasts. *Circ. Res.* **69,** 116–122 (1991).

129. Camelliti, P., Green, C. R., LeGrice, I. & Kohl, P. Fibroblast Network in Rabbit Sinoatrial Node: Structural and Functional Identification of Homogeneous and Heterogeneous Cell Coupling. *Circ. Res.* **94,** 828–835 (2004).

130. Gaudesius, G., Miragoli, M., Thomas, S. P. & Rohr, S. Coupling of cardiac electrical activity over extended distances by fibroblasts of cardiac origin. *Circ. Res.* **93,** 421–428 (2003).

131. Kohl, P. & Gourdie, R. G. Fibroblast-myocyte electrotonic coupling: Does it occur in native cardiac tissue? *J. Mol. Cell. Cardiol.* **70,** 37–46 (2014).

132. Yue, L., Xie, J. & Nattel, S. Molecular determinants of cardiac fibroblast electrical function and therapeutic implications for atrial fibrillation. *Cardiovasc. Res.* **89,** 744–753 (2011).

133. Miragoli, M., Salvarani, N. & Rohr, S. Myofibroblasts induce ectopic activity in cardiac tissue. *Circ. Res.* **101,** 755–758 (2007).

134. Zlochiver, S. *et al.* Electrotonic myofibroblast-to-myocyte coupling increases propensity to reentrant arrhythmias in two-dimensional cardiac monolayers. *Biophys. J.* **95,** 4469–4480 (2008).

135. Radisic, M. *et al.* Pre-treatment of synthetic elastomeric scaffolds by cardiac fibroblasts improves engineered heart tissue. *J. Biomed. Mater. Res. A* **86,** 713–24 (2008).

136. Iyer, R. K., Chiu, L. L. Y. & Radisic, M. Microfabricated poly(ethylene glycol) templates enable rapid screening of triculture conditions for cardiac tissue engineering. *J. Biomed. Mater. Res. - Part A* **89,** 616–631 (2009).

137. Iyer, R. K., Odedra, D., Chiu, L. L. Y., Vunjak-Novakovic, G. & Radisic, M. Vascular endothelial growth factor secretion by nonmyocytes modulates Connexin-43 levels in cardiac organoids. *Tissue Eng. Part A* **18,** 1771–83 (2012).

138. Zhang, D. *et al.* Tissue-engineered cardiac patch for advanced functional maturation of human ESC-derived cardiomyocytes. *Biomaterials* **34,** 5813–5820 (2013).

139. Liau, B., Christoforou, N., Leong, K. W. & Bursac, N. Pluripotent stem cell-derived cardiac tissue patch with advanced structure and function. *Biomaterials* **32,** 9180–7 (2011).

140. Thavandiran, N. *et al.* Design and formulation of functional pluripotent stem cell-derived cardiac microtissues. *Proc. Natl. Acad. Sci. U. S. A.* **110,** E4698-707 (2013).

141. Fries, K. M. *et al.* Evidence of fibroblast heterogeneity and the role of fibroblast subpopulations in fibrosis. *Clinical immunology and immunopathology* **72,** 283–292 (1994).

142. Goodpaster, T. *et al.* An immunohistochemical method for identifying fibroblasts in formalin-fixed, paraffin-embedded tissue. *J. Histochem. Cytochem.* **56,** 347–358 (2008).

143. Radisic, M. *et al.* Biomimetic Approach to Cardiac Tissue Engineering: Oxygen Carriers and Channeled Scaffolds. *Tissue Eng.* **12,** 60913044658032 (2006).

144. Cheng, M., Moretti, M., Engelmayr, G. C. & Freed, L. E. Insulin-like growth factor-I and slow, bi-directional perfusion enhance the formation of tissue-engineered cardiac grafts. *Tissue Eng. Part A* **15,** 645–653 (2009).

145. Sun, X., Altalhi, W. & Nunes, S. S. Vascularization strategies of engineered tissues and their application in cardiac regeneration. *Adv. Drug Deliv. Rev.* **96,** 183–194 (2016).

146. Caputo, M. *et al.* MicroRNAs in vascular tissue engineering and post-ischemic neovascularization. *Adv. Drug Deliv. Rev.* (2015). doi:10.1016/j.addr.2015.05.003

147. Dambrot, C. *et al.* Serum supplemented culture medium masks hypertrophic phenotypes in human pluripotent stem cell derived cardiomyocytes. *J. Cell. Mol. Med.* **18,** 1509–1518 (2014).

148. Zierhut, W. & Zimmer, H. G. Significance of myocardial alpha- and beta-adrenoceptors in catecholamine-induced cardiac hypertrophy. *Circ. Res.* **65,** 1417–1425 (1989).

149. Zhang, Y. *et al.* Acetylcholine inhibits the hypoxia-induced reduction of connexin43 protein in rat cardiomyocytes. *J. Pharmacol. Sci.* **101,** 214–222 (2006).

150. Lyon, A. R., Rees, P. S. C., Prasad, S., Poole-Wilson, P. a & Harding, S. E. Stress (Takotsubo) cardiomyopathy--a novel pathophysiological hypothesis to explain catecholamine-induced acute myocardial stunning. *Nat. Clin. Pract. Cardiovasc. Med.* **5,** 22–29 (2008).

151. Földes, G. *et al.* Modulation of human embryonic stem cell-derived cardiomyocyte growth: A testbed for studying human cardiac hypertrophy? *J. Mol. Cell. Cardiol.* **50,** 367–376 (2011).

152. Tiburcy, M. *et al.* Terminal differentiation, advanced organotypic maturation, and modeling of hypertrophic growth in engineered heart tissue. *Circ. Res.* **109,** 1105–1114 (2011).

153. Cheng, M., Park, H., Engelmayr, G. C., Moretti, M. & Freed, L. E. Effects of regulatory factors on engineered cardiac tissue in vitro. *Tissue Eng.* **13,** 2709–2719 (2007).

154. Veerman, C. C. *et al.* Immaturity of Human Stem-Cell-Derived Cardiomyocytes in Culture: Fatal Flaw or Soluble Problem? *Stem Cells Dev.* **0,** 150225071411000 (2015).

155. Yang, X. *et al.* Tri-iodo-l-thyronine promotes the maturation of human cardiomyocytes-derived from induced pluripotent stem cells. *J. Mol. Cell. Cardiol.* **72,** 296–304 (2014).

156. Ribeiro, M. C. *et al.* Functional maturation of human pluripotent stem cell derived cardiomyocytes in vitro – Correlation between contraction force and electrophysiology. *Biomaterials* **51,** 138–150 (2015).

157. Lee, Y.-K. *et al.* Triiodothyronine Promotes Cardiac Differentiation and Maturation of Embryonic Stem Cells via the Classical Genomic Pathway. *Mol. Endocrinol.* **24,** 1728–1736 (2010).

158. Lancaster, M. A. & Knoblich, J. A. Organogenesis in a dish: modeling development and disease using organoid technologies. *Science* **345,** 1247125 (2014).

159. PhRMA & Pharmaceutical Research and Manufacturers of America. 2013 Biopharmaceutical Research Industry Profile. 1–78 (2013).

160. Shah, R. R. Can pharmacogenetics help rescue drugs withdrawn from the market? *Pharmacogenomics* **7,** 889–908 (2006).

161. Aboumarzouk, O. M., Agarwal, T., Antakia, R., Shariff, U. & Nelson, R. L. Cisapride for intestinal constipation. *Cochrane database Syst. Rev.* CD007780 (2011). doi:10.1002/14651858.CD007780.pub2

162. Dick, E., Rajamohan, D., Ronksley, J. & Denning, C. Evaluating the utility of cardiomyocytes from human pluripotent stem cells for drug screening. *Biochem. Soc. Trans.* **38,** 1037–45 (2010).

163. Kehat, I. *et al.* Human embryonic stem cells can differentiate into myocytes with structural and functional properties of cardiomyocytes. *J. Clin. Invest.* **108,** 407–14 (2001).

164. Stoelzle, S. *et al.* State-of-the-Art Automated Patch Clamp Devices: Heat Activation, Action Potentials, and High Throughput in Ion Channel Screening. *Front. Pharmacol.* **2,** 76 (2011).

165. Malboubi, M. & Jiang, K. Development of Patch Clamping. in *Gigaseal Formation in Patch Clamping with Application in Nanotechnology* (Springer Berlin Heidelberg, 2014). doi:10.1007/978-3-642-39128-6

166. Yajuan, X., Xin, L. & Zhiyuan, L. A comparison of the performance and application differences between manual and automated patch-clamp techniques. *Curr. Chem. Genomics* **6,** 87–92 (2012).

167. Herron, T. J., Lee, P. & Jalife, J. Optical imaging of voltage and calcium in cardiac cells & tissues. *Circ. Res.* **110,** 609–623 (2012).

168. Bursac, N., Kirkton, K. R. D., C, M. L. & Liau, B. Characterizing functional stem cell–cardiomyocyte interactions. *Regen. Med.* **5,** 1–29 (2010).

169. McCombs, J. E. & Palmer, A. E. Measuring calcium dynamics in living cells with genetically encodable calcium indicators. *Methods* **46,** 152–9 (2008).

170. Clements, M. & Thomas, N. High-Throughput Multi-Parameter Profiling of Electrophysiological Drug Effects in Human Embryonic Stem Cell Derived Cardiomyocytes Using Multi-Electrode Arrays. *Toxicol. Sci.* **140,** 445–461 (2014).

171. Peters, M. F., Lamore, S. D., Guo, L., Scott, C. W. & Kolaja, K. L. Human Stem Cell-Derived Cardiomyocytes in Cellular Impedance Assays: Bringing Cardiotoxicity Screening to the Front Line. *Cardiovasc. Toxicol.* **15,** 127–139 (2015).

172. Xi, B. *et al.* Functional cardiotoxicity profiling and screening using the xCELLigence RTCA Cardio System. *J. Lab. Autom.* **16,** 415–21 (2011).

173. Lian, X. *et al.* Directed cardiomyocyte differentiation from human pluripotent stem cells by modulating Wnt/β-catenin signaling under fully defined conditions. *Nat. Protoc.* **8,** 162–75 (2013).

174. Sun, D., Roth, S. & Black, M. J. Secrets of optical flow estimation and their principles. *Proc. IEEE Comput. Soc. Conf. Comput. Vis. Pattern Recognit.* 2432–2439 (2010).

175. Hather, C., Roquemore, L. & Thomas, N. High-content analysis of a live multiplexed cytotoxicity study using Cytiva ™ Cardiomyocytes and IN Cell Analyzer 2000. *Healthc. Life Sci. Newsl. - Discov. Matters* 13 (2011).

176. Olsen, C., Hesley, J. & Sirenko, O. High-Throughput Multiparameter. *Genet. Eng. Biotechnol. News* **33,** 36–37 (2013).

177. Soloveva, V., Larocque, J. & Mckillip, E. When Robots Are Good:Fully Automated Thermo LAS Robotic Assay System with Dual FLIPRTETRA and TAP SelecT Robotic Cell Culture System. *J. Assoc. Lab. Autom.* **11,** 145–156 (2006).

178. Okada, Y., Ogawa, S., Sadanaga, T. & Mitamura, H. Assessment of reverse use-dependent blocking actions of class III antiarrhythmic drugs by 24-hour Holter electrocardiography. *J. Am. Coll. Cardiol.* **27,** 84–9 (1996).

179. Kirsch, G. E. *et al.* Variability in the measurement of hERG potassium channel inhibition: effects of temperature and stimulus pattern. *J. Pharmacol. Toxicol. Methods* **50,** 93–101 (2004).

180. Haft, J. I. & Habbab, M. A. Treatment of Atrial Arrhythmias Effectiveness of Verapamil When Preceded by Calcium Infusion. *Arch. Intern. Med.* **146,** 1085–1089 (1986).

181. Bergson, P., Lipkind, G., Lee, S. P., Duban, M.-E. & Hanck, D. a. Verapamil block of T-type calcium channels. *Mol. Pharmacol.* **79,** 411–9 (2011).

182. Mattiazzi, A. & A, G. Negative inotropic effect of verapamil, nifedipine and prenylamine and its reversal by calcium or isoproterenol. *Arch. Int. Physiol. Biochem.* **91,** 133–144 (1983).

183. Kovács, M. *et al.* Mechanism of blebbistatin inhibition of myosin II. *J. Biol. Chem.* **279,** 35557–35563 (2004).

184. Cerignoli, F. *et al.* High throughput measurement of Ca^{2+} dynamics for drug risk assessment in human stem cell-derived cardiomyocytes by kinetic image cytometry. *J. Pharmacol. Toxicol. Methods* **66,** 246–56 (2012).

185. Qian, J.-Y. & Guo, L. Altered cytosolic Ca2+ dynamics in cultured Guinea pig cardiomyocytes as an in vitro model to identify potential cardiotoxicants. *Toxicol. In Vitro* **24,** 960–72 (2010).

186. Ke, N., Wang, X., Xu, X. & Abassi, Y. A. The xCELLigence System for Real-Time and Label-Free Monitoring of Cell Viability. in *Mammalian Cell Viability* (ed. Stoddart, M. J.) **740,** 33–43 (Humana Press, 2011).

187. Guo, L. *et al.* Estimating the Risk of Drug-Induced Proarrhythmia Using Human Induced Pluripotent Stem Cell–Derived Cardiomyocytes. *Toxicol. Sci.* **123,** 281–289 (2011).

188. Scott, C. W. & Peters, M. F. Label-free whole-cell assays: expanding the scope of GPCR screening. *Drug Discov. Today* **15,** 704–16 (2010).

189. Qiu, Y., Liao, R. & Zhang, X. Impedance-based monitoring of ongoing cardiomyocyte death induced by tumor necrosis factor-alpha. *Biophys. J.* **96,** 1985–91 (2009).

190. Mummery, C. *et al.* Differentiation of human embryonic stem cells to cardiomyocytes: role of coculture with visceral endoderm-like cells. *Circulation* **107,** 2733–2740 (2003).

191. Hanjaya-Putra, D. & Gerecht, S. Mending the Failing Heart with a Vascularized Cardiac Patch. *Cell Stem Cell* **5,** 575–576 (2009).

192. Boudou, T. *et al.* A microfabricated platform to measure and manipulate the mechanics of engineered cardiac microtissues. *Tissue Eng. Part A* **18,** 910–9 (2012).

193. Liu, X., Iyengar, S. G. & Rittscher, J. Monitoring cardiomyocyte motion in real time through image registration and time series analysis. *IEEE Int. Symp. Biomed. Imaging From Nano to Macro* 1308–1311 (2012).

194. Hossain, M. M. *et al.* Non-invasive characterization of mouse embryonic stem cell derived cardiomyocytes based on the intensity variation in digital beating video. *Analyst* **135,** 1624–30 (2010).

195. Ahola, A. *et al.* Video image-based analysis of single human induced pluripotent stem cell derived cardiomyocyte beating dynamics using digital image correlation. *Biomed. Eng. Online* **13,** 39 (2014).

196. Kim, S. B. *et al.* A cell-based biosensor for real-time detection of cardiotoxicity using lensfree imaging. *Lab Chip* **11,** 1801–7 (2011).

197. Maddah, M. & Loewke, K. Automated , Non-Invasive Characterization of Stem Cell-Derived Cardiomyocytes from Phase-Contrast Microscopy. *Med. Image Comput. Comput. Interv.* **17,** 57–64 (2014).

198. Hayakawa, T. *et al.* Noninvasive Evaluation of Contractile Behavior of Cardiomyocyte Monolayers Based on Motion Vector Analysis. *Tissue Eng. Part C Methods* **18,** 21–32 (2012).

199. Hayakawa, T. *et al.* Image-based evaluation of contraction–relaxation kinetics of human-induced pluripotent stem cell-derived cardiomyocytes: Correlation and complementarity with extracellular electrophysiology. *J. Mol. Cell. Cardiol.* **77,** 178–191 (2014).

200. Huebsch, N. *et al.* Automated Video-Based Analysis of Contractility and Calcium Flux in Human-Induced Pluripotent Stem-Derived Cardiomyocytes Cultured over Different Spatial Scales. *Tissue Eng. Part C. Methods* **21,** 1–13 (2014).

201. Maddah, M. *et al.* A Non-invasive Platform for Functional Characterization of Stem-Cell-Derived Cardiomyocytes with Applications in Cardiotoxicity Testing. *Stem cell reports* **4,** 621–631 (2015).

202. Gintant, G., Sager, P. T. & Stockbridge, N. Evolution of strategies to improve preclinical cardiac safety testing. *Nat. Rev. Drug Discov.* **15,** 457–471 (2016).

203. Cavero, I. & Holzgrefe, H. Comprehensive in vitro Proarrhythmia Assay, a novel in vitro/in silico paradigm to detect ventricular proarrhythmic liability: a visionary 21st century initiative. *Expert Opin. Drug Saf.* **13,** 745–58 (2014).

204. Fermini, B. *et al.* A New Perspective in the Field of Cardiac Safety Testing through the Comprehensive In Vitro Proarrhythmia Assay Paradigm. *J. Biomol. Screen.* **21,** 1–11 (2016).

205. Gilchrist, K. H., Lewis, G. F., Gay, E. a., Sellgren, K. L. & Grego, S. High-throughput cardiac safety evaluation and multi-parameter arrhythmia profiling of cardiomyocytes using microelectrode arrays. *Toxicol. arahnd Appl. Pharmacol.* **288,** 249–257 (2015).

206. Blinova, K. *et al.* Comprehensive Translational Assessment of Human-Induced Pluripotent Stem Cell Derived Cardiomyocytes for Evaluating Drug-Induced Arrhythmias. *Toxicol. Sci.* **155,** 234–247 (2017).

207. Chen, I. Y., Matsa, E. & Wu, J. C. Induced pluripotent stem cells: at the heart of cardiovascular precision medicine. *Nat. Rev. Cardiol.* **13,** 333–349 (2016).

208. Stillitano, F. *et al.* Modeling susceptibility to drug-induced long QT with a panel of subject-specific induced pluripotent stem cells. *Elife* **6,** 1–24 (2017).

209. Maizels, L. *et al.* Patient-Specific Drug Screening Using a Human Induced Pluripotent Stem Cell Model of Catecholaminergic Polymorphic Ventricular Tachycardia Type 2. *Circ. Arrhythmia Electrophysiol.* **10,** e004725 (2017).

210. Clements, M., Millar, V., Williams, A. S. & Kalinka, S. Bridging functional and structural cardiotoxicity assays using human embryonic stem cell-derived cardiomyocytes for a more comprehensive risk assessment. *Toxicol. Sci.* **148,** 241–260 (2015).

211. Sharma, A. *et al.* High-throughput screening of tyrosine kinase inhibitor cardiotoxicity with human induced pluripotent stem cells. *Sci. Transl. Med.* **9,** eaaf2584 (2017).

212. Doherty, K. R. *et al.* Structural and functional screening in human induced-pluripotent stem cell-derived cardiomyocytes accurately identifies cardiotoxicity of multiple drug types. *Toxicol. Appl. Pharmacol.* **285,** 51–60 (2015).

213. Pointon, A., Abi-gerges, N., Cross, M. J. & Sidaway, J. E. Phenotypic profiling of structural cardiotoxins in vitro reveals dependency on multiple mechanisms of toxicity. *Toxicol. Sci.* **132,** 317–326 (2013).

214. Ewer, M. S. & Ewer, S. M. Cardiotoxicity of anticancer treatments. *Nat. Rev. Cardiol.* **12,** 547–558 (2015).

215. Burridge, P. W. *et al.* Human induced pluripotent stem cell–derived cardiomyocytes recapitulate the predilection of breast cancer patients to doxorubicin-induced cardiotoxicity. *Nat. Med.* **22,** 547–556 (2016).

216. Maillet, A. *et al.* Modeling Doxorubicin-Induced Cardiotoxicity in Human Pluripotent Stem Cell Derived-Cardiomyocytes. *Sci. Rep.* **6,** 25333 (2016).

217. Holmgren, G. *et al.* Identification of novel biomarkers for doxorubicin-induced toxicity in human cardiomyocytes derived from pluripotent stem cells. *Toxicology* **328,** 102–111 (2015).

218. Zhao, L. & Zhang, B. Doxorubicin induces cardiotoxicity through upregulation of death receptors mediated apoptosis in cardiomyocytes. *Sci. Rep.* **7,** 44735 (2017).

219. Brown, C. Targeted therapy: An elusive cancer target. *Nature* **537,** S106–S108 (2016).

220. Force, T. & Kolaja, K. L. Cardiotoxicity of kinase inhibitors: the prediction and translation of preclinical models to clinical outcomes. *Nat. Rev. Drug Discov.* **10,** 111–126

(2011).

221. Cross, M. J. *et al.* Physiological, pharmacological and toxicological considerations of drug-induced structural cardiac injury. *Br. J. Pharmacol.* **172,** 957–974 (2015).

222. Cardinale, D. *et al.* Trastuzumab-Induced Cardiotoxicity: Clinical and Prognostic Implications of Troponin I Evaluation. *J. Clin. Oncol.* **28,** 3910–3916 (2010).

223. Narayan, H. K. *et al.* Detailed Echocardiographic Phenotyping in Breast Cancer PatientsClinical Perspective. *Circulation* **135,** 1397–1412 (2017).

224. Seidman, A. *et al.* Cardiac Dysfunction in the Trastuzumab Clinical Trials Experience. *J. Clin. Oncol.* **20,** 1215–1221 (2002).

225. Crone, S. a *et al.* ErbB2 is essential in the prevention of dilated cardiomyopathy. *Nat. Med.* **8,** 459–465 (2002).

226. Fukazawa, R. *et al.* Neuregulin-1 protects ventricular myocytes from anthracycline-induced apoptosis via erbB4-dependent activation of PI3-kinase/Akt. *J. Mol. Cell. Cardiol.* **35,** 1473–9 (2003).

227. Kurokawa, Y. K. *et al.* Human Induced Pluripotent Stem Cell-Derived Endothelial Cells for Three-Dimensional Microphysiological Systems. *Tissue Eng. Part C Methods* **23,** 474–484 (2017).

228. Chen, T.-W. *et al.* Ultrasensitive fluorescent proteins for imaging neuronal activity. *Nature* **499,** 295–300 (2013).

229. Huebsch, N. *et al.* Automated Video-Based Analysis of Contractility and Calcium Flux in Human-Induced Pluripotent Stem Cell-Derived Cardiomyocytes Cultured over Different Spatial Scales. *Tissue Eng. Part C Methods* **21,** 467–479 (2015).

230. Moya, M. L., Hsu, Y.-H., Lee, A. P., Hughes, C. C. W. & George, S. C. In Vitro Perfused Human Capillary Networks. *Tissue Eng. Part C Methods* **19,** 730–737 (2013).

231. Lian, X. *et al.* Robust cardiomyocyte differentiation from human pluripotent stem cells via temporal modulation of canonical Wnt signaling. *Proc. Natl. Acad. Sci.* **109,** E1848–E1857 (2012).

232. Lee, E. K., Kurokawa, Y. K., Tu, R., George, S. C. & Khine, M. Machine learning plus optical flow: a simple and sensitive method to detect cardioactive drugs. *Sci. Rep.* **5,** 11817 (2015).

233. Schmittgen, T. D. & Livak, K. J. Analyzing real-time PCR data by the comparative CT method. *Nat. Protoc.* **3,** 1101–1108 (2008).

234. Geisberg, C. A. *et al.* Circulating neuregulin-1β levels vary according to the angiographic severity of coronary artery disease and ischemia. *Coron. Artery Dis.* **22,** 577–582 (2011).

235. Gintant, G., Fermini, B., Stockbridge, N. & Strauss, D. The Evolving Roles of Human

iPSC-Derived Cardiomyocytes in Drug Safety and Discovery. *Cell Stem Cell* **21,** 14–17 (2017).

236. Rentschler, S. *et al.* Neuregulin-1 promotes formation of the murine cardiac conduction system. *Proc. Natl. Acad. Sci. U. S. A.* **99,** 10464–10469 (2002).

237. Ramachandra, C. J. A., Mehta, A., Wong, P. & Shim, W. ErbB4 Activated p38γ MAPK Isoform Mediates Early Cardiogenesis Through NKx2.5 in Human Pluripotent Stem Cells. *Stem Cells* **34,** 288–298 (2016).

238. Necela, B. M. *et al.* The antineoplastic drug, trastuzumab, dysregulates metabolism in iPSC-derived cardiomyocytes. *Clin. Transl. Med.* **6,** 5 (2017).

239. Tiburcy, M. *et al.* Defined Engineered Human Myocardium With Advanced Maturation for Applications in Heart Failure Modeling and RepairClinical Perspective. *Circulation* **135,** 1832–1847 (2017).

240. Vermeulen, Z., Segers, V. F. M. & De Keulenaer, G. W. ErbB2 signaling at the crossing between heart failure and cancer. *Basic Res. Cardiol.* **111,** 60 (2016).

241. Gao, R. *et al.* A Phase II, Randomized, Double-Blind, Multicenter, Based on Standard Therapy, Placebo-Controlled Study of the Efficacy and Safety of Recombinant Human Neuregulin-1 in Patients With Chronic Heart Failure. *J. Am. Coll. Cardiol.* **55,** 1907–1914 (2010).

242. Lenihan, D. J. *et al.* A Phase I, Single Ascending Dose Study of Cimaglermin Alfa (Neuregulin 1β3) in Patients With Systolic Dysfunction and Heart Failure. *JACC Basic to Transl. Sci.* **1,** 576–586 (2016).

243. Iwamoto, R. *et al.* Heparin-binding EGF-like growth factor and ErbB signaling is essential for heart function. *Proc. Natl. Acad. Sci.* **100,** 3221–3226 (2003).

244. Takashima, S. & Kitakaze, M. HB-EGF, Transactivation, and Cardiac Hypertrophy. *Int. J. Gerontol.* **1,** 2–9 (2007).

245. Chien, K. R. Herceptin and the Heart — A Molecular Modifier of Cardiac Failure. *N. Engl. J. Med.* **354,** 789–790 (2006).

246. Tocchetti, C. G. *et al.* Detection, monitoring, and management of trastuzumab-induced left ventricular dysfunction: An actual challenge. *Eur. J. Heart Fail.* **14,** 130–137 (2012).

247. Plana, J. C. *et al.* Expert Consensus for Multimodality Imaging Evaluation of Adult Patients during and after Cancer Therapy: A Report from the American Society of Echocardiography and the European Association of Cardiovascular Imaging. *J. Am. Soc. Echocardiogr.* **27,** 911–939 (2014).

248. Ozcelik, C. *et al.* Conditional mutation of the ErbB2 (HER2) receptor in cardiomyocytes leads to dilated cardiomyopathy. *Proc. Natl. Acad. Sci.* **99,** 8880–8885 (2002).

249. Collins, D. M. *et al.* Trastuzumab induces antibody-dependent cell-mediated cytotoxicity

(ADCC) in HER-2-non-amplified breast cancer cell lines. *Ann. Oncol.* **23,** 1788–1795 (2012).

250. Wilkinson, E. L., Sidaway, J. E. & Cross, M. J. Cardiotoxic drugs Herceptin and doxorubicin inhibit cardiac microvascular endothelial cell barrier formation resulting in increased drug permeability. *Biol. Open* **5,** 1362–1370 (2016).

251. Barth, A. S. *et al.* Functional Impairment of Human Resident Cardiac Stem Cells by the Cardiotoxic Antineoplastic Agent Trastuzumab. *Stem Cells Transl. Med.* **1,** 289–297 (2012).

252. Kirabo, A. *et al.* Neuregulin-1β induces proliferation, survival and paracrine signaling in normal human cardiac ventricular fibroblasts. *J. Mol. Cell. Cardiol.* **105,** 59–69 (2017).

253. Passier, R., Orlova, V. & Mummery, C. Complex Tissue and Disease Modeling using hiPSCs. *Cell Stem Cell* **18,** 309–321 (2016).

254. Kurokawa, Y. K. & George, S. C. Tissue engineering the cardiac microenvironment: Multicellular microphysiological systems for drug screening. *Adv. Drug Deliv. Rev.* **96,** 225–233 (2016).

255. Onitilo, A. A., Engel, J. M. & Stankowski, R. V. Cardiovascular toxicity associated with adjuvant trastuzumab therapy: prevalence, patient characteristics, and risk factors. *Ther. Adv. Drug Saf.* **5,** 154–166 (2014).

256. Mair, J. Cardiac troponin I and troponin T: Are enzymes still relevant as cardiac markers? *Clin. Chim. Acta* **257,** 99–115 (1997).

257. Cleaver, O. & Melton, D. a. Endothelial signaling during development. *Nat. Med.* **9,** 661–668 (2003).

258. Rafii, S., Butler, J. M. & Ding, B.-S. Angiocrine functions of organ-specific endothelial cells. *Nature* **529,** 316–325 (2016).

259. Deanfield, J. E., Halcox, J. P. & Rabelink, T. J. Endothelial function and dysfunction: Testing and clinical relevance. *Circulation* **115,** 1285–1295 (2007).

260. Heylman, C., Sobrino, A., Shirure, V. S., Hughes, C. C. & George, S. C. A strategy for integrating essential three-dimensional microphysiological systems of human organs for realistic anticancer drug screening. *Exp. Biol. Med.* **239,** 1240–1254 (2014).

261. Esch, M. B. *et al.* How multi-organ microdevices can help foster drug development. *Adv. Drug Deliv. Rev.* **69–70,** 158–169 (2014).

262. Bhatia, S. N. & Ingber, D. E. Microfluidic organs-on-chips. *Nat. Biotechnol.* **32,** 760–772 (2014).

263. Bogorad, M. I. *et al.* Review: in vitro microvessel models. *Lab Chip* **15,** 4242–4255 (2015).

264. Morin, K. T. & Tranquillo, R. T. In vitro models of angiogenesis and vasculogenesis in fibrin gel. *Exp. Cell Res.* **319,** 2409–17 (2013).

265. Kim, S., Lee, H., Chung, M. & Jeon, N. L. Engineering of functional, perfusable 3D microvascular networks on a chip. *Lab Chip* **13,** 1489–500 (2013).

266. Whisler, J. a, Chen, M. B. & Kamm, R. D. Control of Perfusable Microvascular Network Morphology Using a Multiculture Microfluidic System. *Tissue Eng. Part C Methods* **20,** 543–552 (2014).

267. Wang, X. *et al.* Engineering anastomosis between living capillary networks and endothelial cell-lined microfluidic channels. *Lab Chip* **16,** 282–290 (2016).

268. Alonzo, L. F., Moya, M. L., Shirure, V. S. & George, S. C. Microfluidic device to control interstitial flow-mediated homotypic and heterotypic cellular communication. *Lab Chip* **15,** 3521–3529 (2015).

269. Kim, S., Chung, M., Ahn, J., Lee, S. & Jeon, N. L. Interstitial flow regulates the angiogenic response and phenotype of endothelial cells in a 3D culture model. *Lab Chip* **16,** 4189–4199 (2016).

270. Zanotelli, M. R. *et al.* Stable engineered vascular networks from human induced pluripotent stem cell-derived endothelial cells cultured in synthetic hydrogels. *Acta Biomater.* **35,** 32–41 (2016).

271. Belair, D. G. *et al.* Human Vascular Tissue Models Formed from Human Induced Pluripotent Stem Cell Derived Endothelial Cells. *Stem Cell Rev. Reports* **11,** 511–525 (2015).

272. Bersini, S. *et al.* A microfluidic 3D in vitro model for specificity of breast cancer metastasis to bone. *Biomaterials* **35,** 2454–2461 (2014).

273. Jeon, J. S. *et al.* Human 3D vascularized organotypic microfluidic assays to study breast cancer cell extravasation. *Proc. Natl. Acad. Sci.* **112,** 214–219 (2015).

274. Moya, M., Tran, D. & George, S. C. An integrated in vitro model of perfused tumor and cardiac tissue. *Stem Cell Res. Ther.* **4,** S15 (2013).

275. Sobrino, A. *et al.* 3D microtumors in vitro supported by perfused vascular networks. *Sci. Rep.* **6,** 31589 (2016).

276. Miyaoka, Y. *et al.* Isolation of single-base genome-edited human iPS cells without antibiotic selection. *Nat. Methods* **11,** 291–3 (2014).

277. Samuel, R. *et al.* Generation of functionally competent and durable engineered blood vessels from human induced pluripotent stem cells. *Proc. Natl. Acad. Sci. U. S. A.* **110,** 12774–9 (2013).

278. Mordwinkin, N. M., Lee, A. S. & Wu, J. C. Patient-Specific Stem Cells and Cardiovascular Drug Discovery. *JAMA* **310,** 2039 (2013).

279. Qin, Y. & Gao, W.-Q. Concise Review: Patient-Derived Stem Cell Research for Monogenic Disorders. *Stem Cells* **34,** 44–54 (2016).

280. Clayton, Z. E., Sadeghipour, S. & Patel, S. Generating induced pluripotent stem cell derived endothelial cells and induced endothelial cells for cardiovascular disease modelling and therapeutic angiogenesis. *Int. J. Cardiol.* **197,** 116–122 (2015).

281. Wong, W. T., Huang, N. F., Botham, C. M., Sayed, N. & Cooke, J. P. Endothelial Cells Derived From Nuclear Reprogramming. *Circ. Res.* **111,** 1363–1375 (2012).

282. Wilson, H. K., Canfield, S. G., Shusta, E. V. & Palecek, S. P. Concise Review: Tissue-Specific Microvascular Endothelial Cells Derived From Human Pluripotent Stem Cells. *Stem Cells* **32,** 3037–3045 (2014).

283. Yoder, M. C. Differentiation of pluripotent stem cells into endothelial cells. *Curr. Opin. Hematol.* **22,** 252–257 (2015).

284. Yoder, M. C. *et al.* Redefining endothelial progenitor cells via clonal analysis and hematopoietic stem/progenitor cell principals. *Blood* **109,** 1801–1809 (2007).

285. Schwartz, M. P. *et al.* Human pluripotent stem cell-derived neural constructs for predicting neural toxicity. *Proc. Natl. Acad. Sci.* **112,** 12516–12521 (2015).

286. Kusuma, S., Peijnenburg, E., Patel, P. & Gerecht, S. Low oxygen tension enhances endothelial fate of human pluripotent stem cells. *Arterioscler. Thromb. Vasc. Biol.* **34,** 913–920 (2014).

287. Siflinger-Birnboim, A. *et al.* Molecular sieving characteristics of the cultured endothelial monolayer. *J. Cell. Physiol.* **132,** 111–117 (1987).

288. Mehta, D. Signaling Mechanisms Regulating Endothelial Permeability. *Physiol. Rev.* **86,** 279–367 (2006).

289. Moya, M. L., Alonzo, L. F. & George, S. C. Microfluidic Device to Culture 3D In Vitro Human Capillary Networks. *Methods Mol. Biol.* **1202,** 21–27 (2013).

290. Shirure, V. S. & George, S. C. Design considerations to minimize the impact of drug absorption in polymer-based organ-on-a-chip platforms. *Lab Chip* **17,** 681–690 (2017).

291. Zimmerlin, L. *et al.* Stromal vascular progenitors in adult human adipose tissue. *Cytom. Part A* **77A,** 22–30 (2009).

292. Park, T. S. *et al.* Vascular progenitors from cord blood-derived induced pluripotent stem cells possess augmented capacity for regenerating ischemic retinal vasculature. *Circulation* **129,** 359–372 (2014).

293. Marcelo, K. L., Goldie, L. C. & Hirschi, K. K. Regulation of Endothelial Cell Differentiation and Specification. *Circ. Res.* **112,** 1272–1287 (2013).

294. Atkins, G. B., Jain, M. K. & Hamik, A. Endothelial Differentiation: Molecular

Mechanisms of Specification and Heterogeneity. *Arterioscler. Thromb. Vasc. Biol.* **31,** 1476–1484 (2011).

295. Dejana, E., Orsenigo, F. & Lampugnani, M. G. The role of adherens junctions and VE-cadherin in the control of vascular permeability. *J. Cell Sci.* **121,** 2115–2122 (2008).

296. Lal, B. K., Varma, S., Pappas, P. J., Hobson, R. W. & Durán, W. N. VEGF Increases Permeability of the Endothelial Cell Monolayer by Activation of PKB/akt, Endothelial Nitric-Oxide Synthase, and MAP Kinase Pathways. *Microvasc. Res.* **62,** 252–262 (2001).

297. Rabiet, M.-J. *et al.* Thrombin-Induced Increase in Endothelial Permeability Is Associated With Changes in Cell-to-Cell Junction Organization. *Arterioscler. Thromb. Vasc. Biol.* **16,** 488–496 (1996).

298. Davis, G. E., Bayless, K. J. & Mavila, A. Molecular basis of endothelial cell morphogenesis in three-dimensional extracellular matrices. *Anat. Rec.* **268,** 252–275 (2002).

299. James, D. *et al.* Expansion and maintenance of human embryonic stem cell–derived endothelial cells by TGFβ inhibition is Id1 dependent. *Nat. Biotechnol.* **28,** 161–166 (2010).

300. Demetri, G. D. *et al.* Efficacy and safety of sunitinib in patients with advanced gastrointestinal stromal tumour after failure of imatinib: a randomised controlled trial. *Lancet* **368,** 1329–1338 (2006).

301. Faivre, S., Demetri, G., Sargent, W. & Raymond, E. Molecular basis for sunitinib efficacy and future clinical development. *Nat. Rev. Drug Discov.* **6,** 734–745 (2007).

302. Bao, X. *et al.* Chemically-defined albumin-free differentiation of human pluripotent stem cells to endothelial progenitor cells. *Stem Cell Res.* **15,** 122–129 (2015).

303. White, M. P. *et al.* Limited Gene Expression Variation in Human Embryonic Stem Cell and Induced Pluripotent Stem Cell-Derived Endothelial Cells. *Stem Cells* **31,** 92–103 (2013).

304. Rufaihah, A. J. *et al.* Human induced pluripotent stem cell-derived endothelial cells exhibit functional heterogeneity. *Am. J. Transl. Res.* **5,** 21–35 (2013).

305. Sriram, G., Tan, J. Y., Islam, I., Rufaihah, A. J. & Cao, T. Efficient differentiation of human embryonic stem cells to arterial and venous endothelial cells under feeder- and serum-free conditions. *Stem Cell Res. Ther.* **6,** 261 (2015).

306. Orlova, V. V. *et al.* Functionality of Endothelial Cells and Pericytes From Human Pluripotent Stem Cells Demonstrated in Cultured Vascular Plexus and Zebrafish Xenografts. *Arterioscler. Thromb. Vasc. Biol.* **34,** 177–186 (2014).

307. Baluk, P. & McDonald, D. M. Markers for Microscopic Imaging of Lymphangiogenesis and Angiogenesis. *Ann. N. Y. Acad. Sci.* **1131,** 1–12 (2008).

308. Aird, W. C. Phenotypic Heterogeneity of the Endothelium: I. Structure, Function, and Mechanisms. *Circ. Res.* **100,** 158–173 (2007).

309. Gavard, J. & Gutkind, J. S. VEGF controls endothelial-cell permeability by promoting the β-arrestin-dependent endocytosis of VE-cadherin. *Nat. Cell Biol.* **8,** 1223–1234 (2006).

310. Breslin, J. W., Zhang, X. E., Worthylake, R. A. & Souza-Smith, F. M. Involvement of Local Lamellipodia in Endothelial Barrier Function. *PLoS One* **10,** e0117970 (2015).

311. Taha, A. A., Taha, M., Seebach, J. & Schnittler, H.-J. ARP2/3-mediated junction-associated lamellipodia control VE-cadherin-based cell junction dynamics and maintain monolayer integrity. *Mol. Biol. Cell* **25,** 245–256 (2014).

312. Prasain, N. *et al.* Differentiation of human pluripotent stem cells to cells similar to cord-blood endothelial colony–forming cells. *Nat. Biotechnol.* **32,** 1151–1157 (2014).

313. Hu, S. *et al.* Effects of cellular origin on differentiation of human induced pluripotent stem cell–derived endothelial cells. *JCI Insight* **1,** 1–12 (2016).

314. Davis, G. E. Endothelial Extracellular Matrix: Biosynthesis, Remodeling, and Functions During Vascular Morphogenesis and Neovessel Stabilization. *Circ. Res.* **97,** 1093–1107 (2005).

315. Kusuma, S., Facklam, A. & Gerecht, S. Characterizing Human Pluripotent-Stem-Cell-Derived Vascular Cells for Tissue Engineering Applications. *Stem Cells Dev.* **24,** 451–458 (2015).

316. Nakatsu, M. N. *et al.* Angiogenic sprouting and capillary lumen formation modeled by human umbilical vein endothelial cells (HUVEC) in fibrin gels: the role of fibroblasts and Angiopoietin-1. *Microvasc. Res.* **66,** 102–112 (2003).

317. Inman, G. J. SB-431542 Is a Potent and Specific Inhibitor of Transforming Growth Factor-beta Superfamily Type I Activin Receptor-Like Kinase (ALK) Receptors ALK4, ALK5, and ALK7. *Mol. Pharmacol.* **62,** 65–74 (2002).

318. Bai, H., Gao, Y., Hoyle, D. L., Cheng, T. & Wang, Z. Z. Suppression of Transforming Growth Factor-β Signaling Delays Cellular Senescence and Preserves the Function of Endothelial Cells Derived from Human Pluripotent Stem Cells. *Stem Cells Transl. Med.* **6,** 589–600 (2017).

319. Bhise, N. S. *et al.* Organ-on-a-chip platforms for studying drug delivery systems. *J. Control. Release* **190,** 82–93 (2014).

320. Sung, J. H. *et al.* Microfabricated mammalian organ systems and their integration into models of whole animals and humans. *Lab Chip* **13,** 1201 (2013).

321. Low, L. A. & Tagle, D. A. Tissue chips – innovative tools for drug development and disease modeling. *Lab Chip* **17,** 3026–3036 (2017).

322. Bezzerides, V. J., Zhang, D. & Pu, W. T. Modeling Inherited Arrhythmia Disorders Using

Induced Pluripotent Stem Cell-Derived Cardiomyocytes. *Circ. J.* **81,** 12–21 (2017).

323. Karakikes, I. *et al.* A Comprehensive TALEN-Based Knockout Library for Generating Human-Induced Pluripotent Stem Cell–Based Models for Cardiovascular DiseasesNovelty and Significance. *Circ. Res.* **120,** 1561–1571 (2017).

324. Ross, S. B., Fraser, S. T. & Semsarian, C. Induced pluripotent stem cells in the inherited cardiomyopathies: From disease mechanisms to novel therapies. *Trends Cardiovasc. Med.* **26,** 663–672 (2016).

325. Wagner, B. K. & Schreiber, S. L. The Power of Sophisticated Phenotypic Screening and Modern Mechanism-of-Action Methods. *Cell Chem. Biol.* **23,** 3–9 (2016).

326. Vincent, F. *et al.* Developing predictive assays: The phenotypic screening 'rule of 3'. *Sci. Transl. Med.* **7,** 293ps15-293ps15 (2015).

327. Schork, N. J. Personalized medicine: Time for one-person trials. *Nature* **520,** 609–611 (2015).

328. Matsa, E. *et al.* Transcriptome Profiling of Patient-Specific Human iPSC-Cardiomyocytes Predicts Individual Drug Safety and Efficacy Responses In Vitro. *Cell Stem Cell* **19,** 311–325 (2016).

329. Joyner, M. J. & Paneth, N. Seven Questions for Personalized Medicine. *JAMA* **314,** 999 (2015).

330. Forsberg, L. A., Absher, D. & Dumanski, J. P. Non-heritable genetics of human disease: spotlight on post-zygotic genetic variation acquired during lifetime. *J. Med. Genet.* **50,** 1–10 (2013).

Appendix

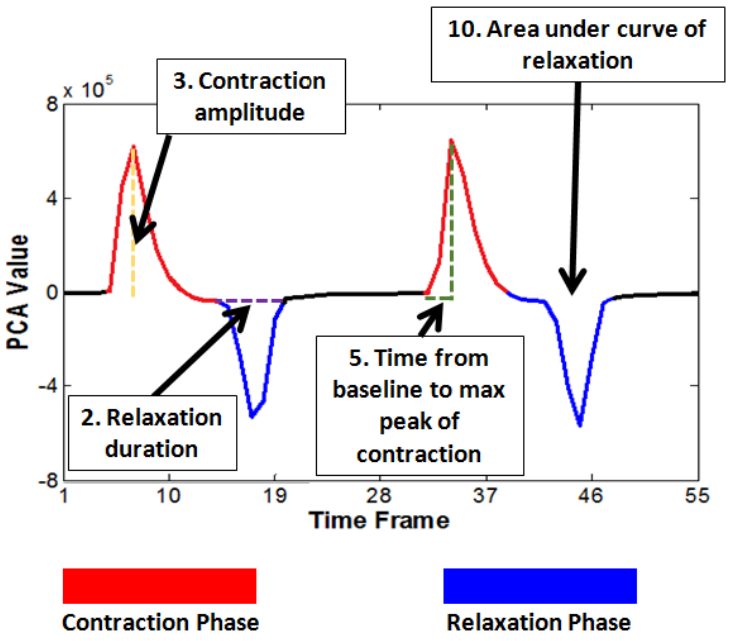

Parameters	
1.	Contraction duration
2.	Relaxation duration
3.	Contraction amplitude
4.	Relaxation amplitude
5.	Time from baseline to max peak of contraction
6.	Time from baseline to max peak of relaxation
7.	Time from max peak to baseline of contraction
8.	Time from max peak to baseline of relaxation
9.	Area under Curve of contraction
10.	Area under Curve of relaxation
11.	Frequency
12.	Total duration

Figure A1.1: Parameters derived from the contractile profiles based on the 1st PCA of motion vectors. (Left panel) Red indicates the contraction phase of an iPS-CM beat and has positive PCA values. The blue indicates the subsequent relaxation phase of a beat and is designated by negative PCA values. (Right panel) List of the 12 parameters that are extracted from the contractile profile.

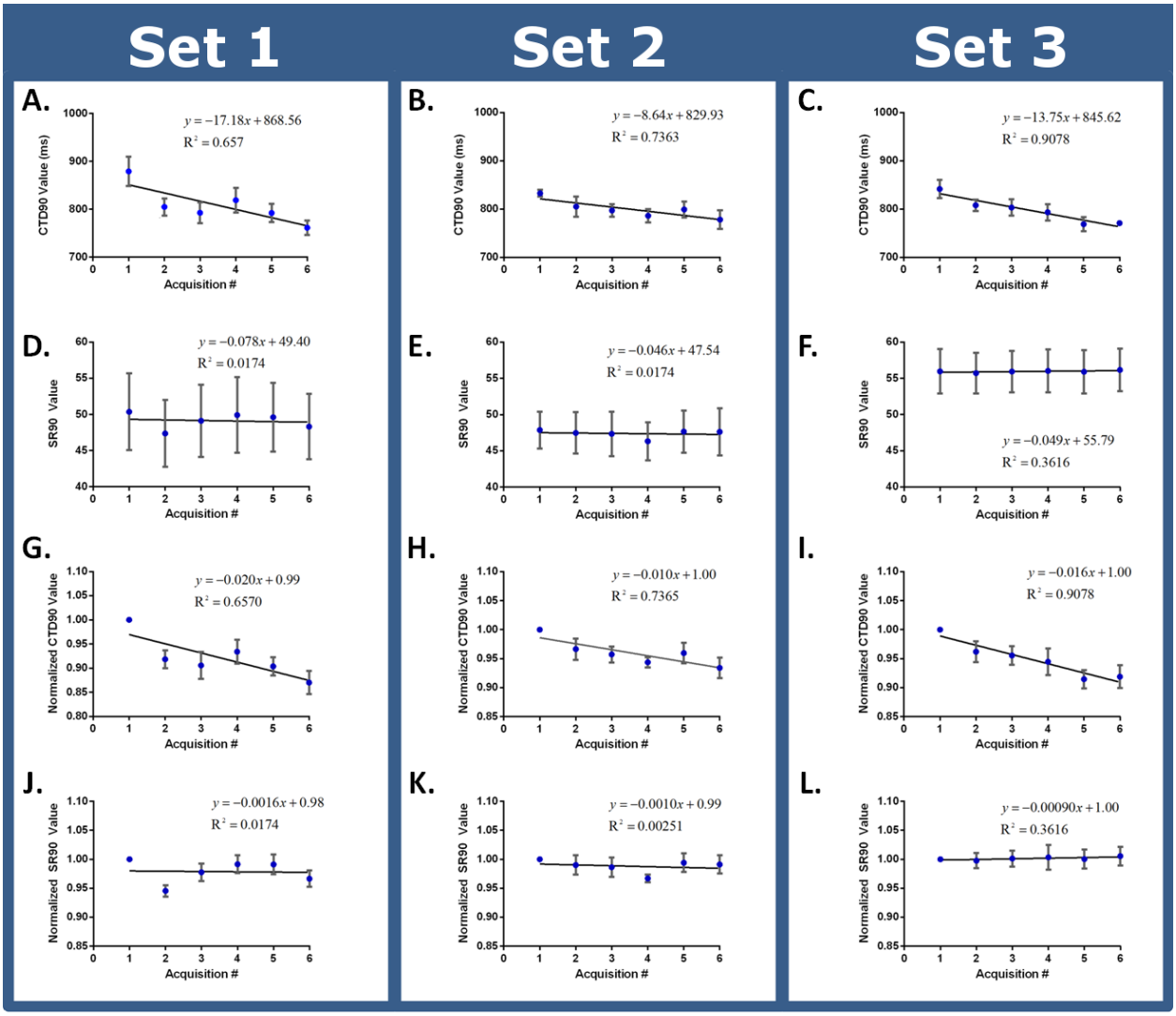

Figure A1.2: (A-C) Set 1 &2 of the longitudinal experiments had acquisitions taken at intervals of 30 minutes; while Set 3 had acquisitions taken at intervals of 9 minutes with exception of last time point (time point was taken at 90 minutes instead). The results showed a similar decrease in CTD_{90}, suggesting that there is little to no recovery from photobleaching during the length of the experiment. While the decrease is similar, the CTD90 values among each of the sets of microscope chamber slides used for the longitudinal experiment decreased at different rates. (D-E) The calculated SR90 for all three sets removed the decaying trend among acquisitions. (F-G) To control for the different initial CTD90 values, all subsequent values were normalized to the starting values. The normalization still yielded decreasing trends that differed among the sets. (J-L) The best-fit lines generated from the linear regression of the normalized SR90 values were relatively uniform.

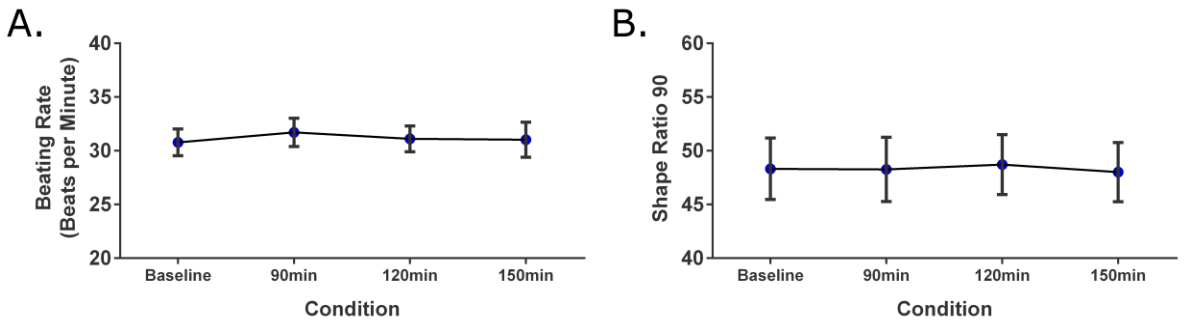

Figure A1.3: Analysis of GCaMP6 data from longitudinal study. With the GCaMP6 method, no significant changes in the (A) beating rate or (B) SR_{90} were detected at any of the time points (n = 13).

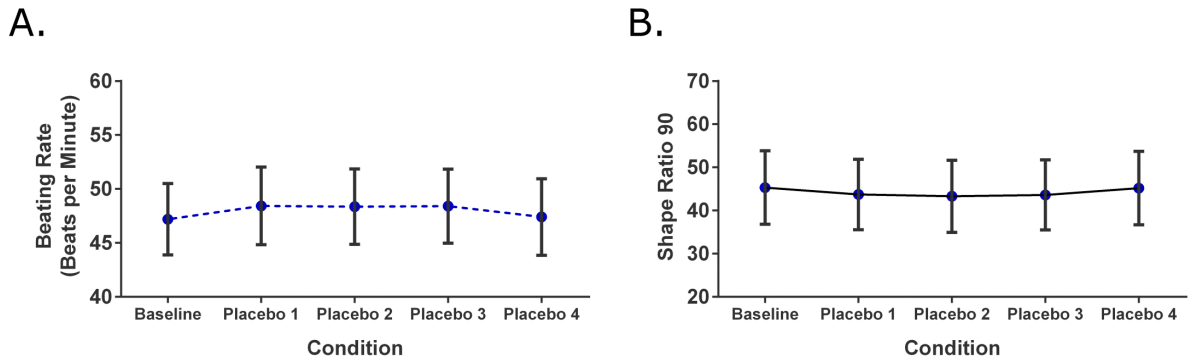

Figure A1.4: Analysis of GCaMP6 data from placebo study. During the length of the placebo experiments, there was no observable change in the (A) beating rate or (B) SR_{90} using the GCaMP analysis (n =18).

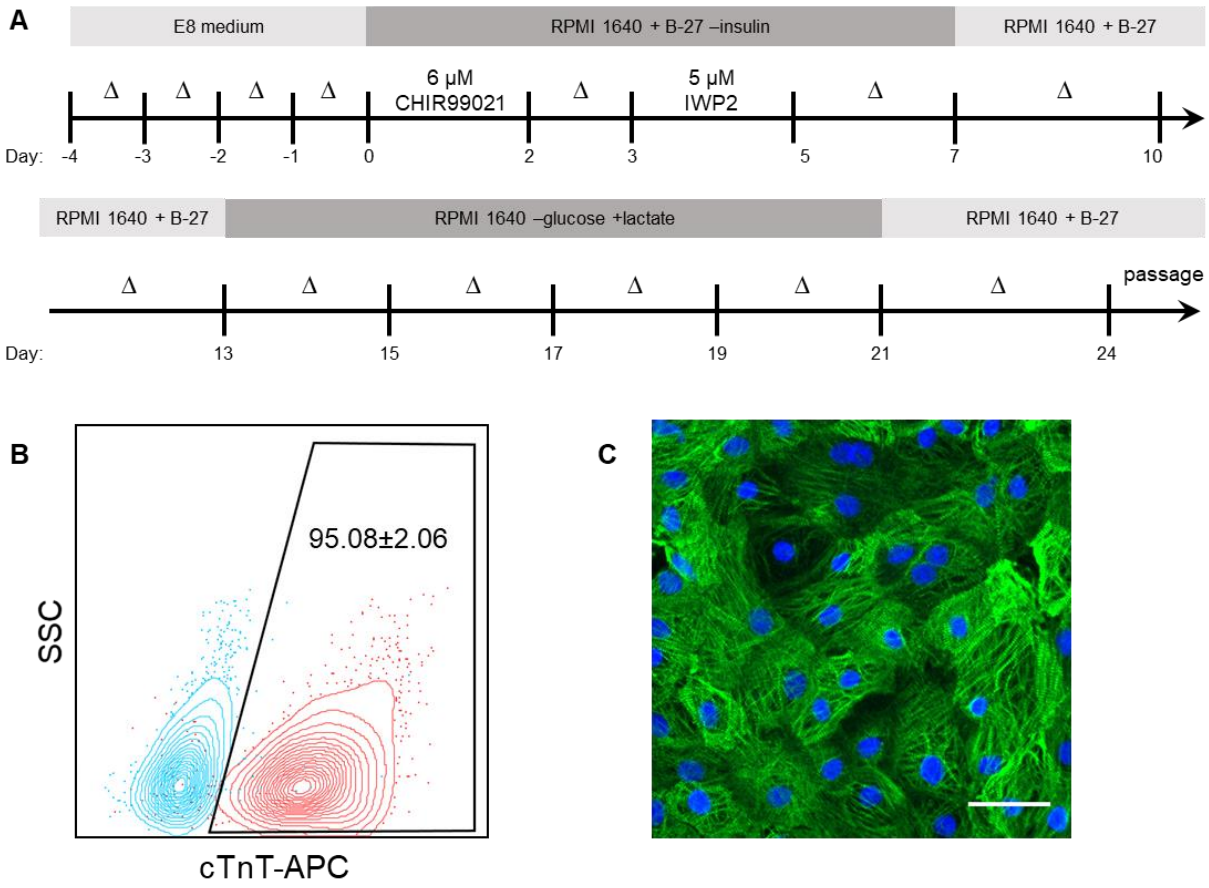

Figure A2.1: Differentiation and isolation of iPS-CMs. (A) Schematic diagram of iPS-CM differentiation and purification. The cells are passaged on Day 24 to be cryopreserved or replated. (Δ) denotes one medium change. (B) Flow cytometry analysis of the resulting iPS-CM population. The cells are stained for the expression of cTnT. (C) Immunofluorescence of the iPS-CMs replated in a 96-well plate. Green = cTnT, blue = DAPI. Scale bar = 50 µm.

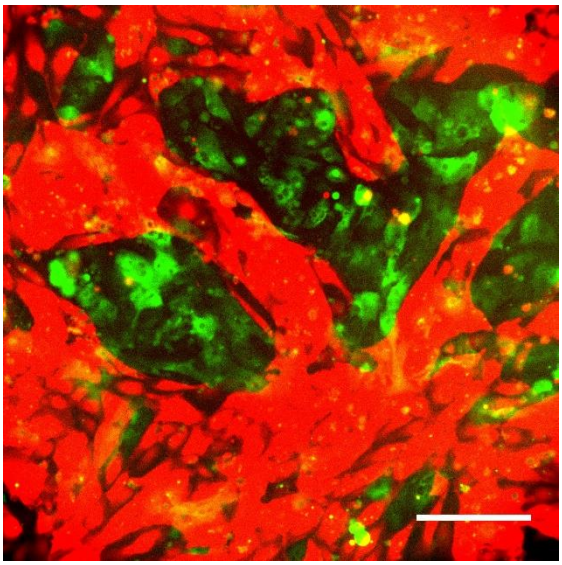

Figure A2.2: Co-culture of iPS-CM and ECFC-EC at a ratio of 40,000:5,000 CM:EC in a 96-well plate. Green = iPS-CM (GCaMP6), red = ECFC-EC (transduced). Scale bar = 250 μm.

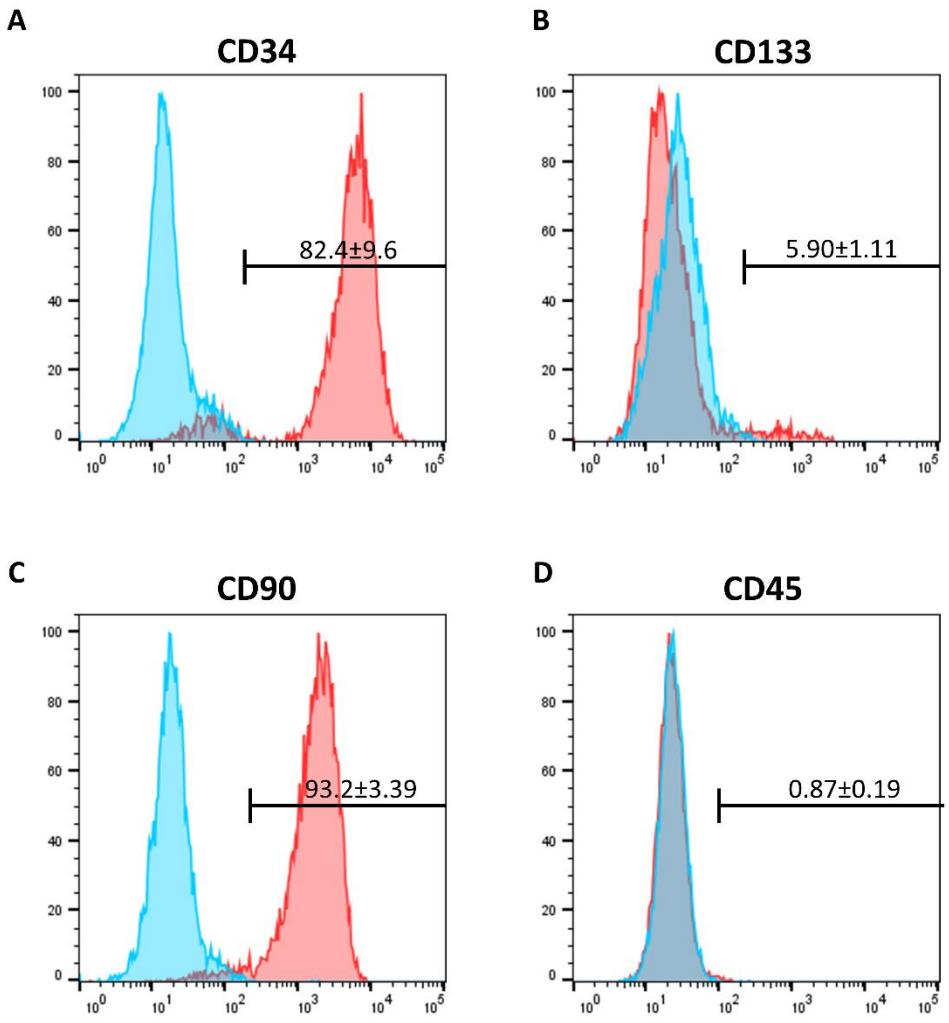

Figure A3.1: Flow cytometry analysis of iPS-ECs on Day 8. The magnetically sorted iPS-EC population was checked for expression of (A) CD34, (B) CD133, (C) CD90, and (D) CD45. Blue = isotype control.

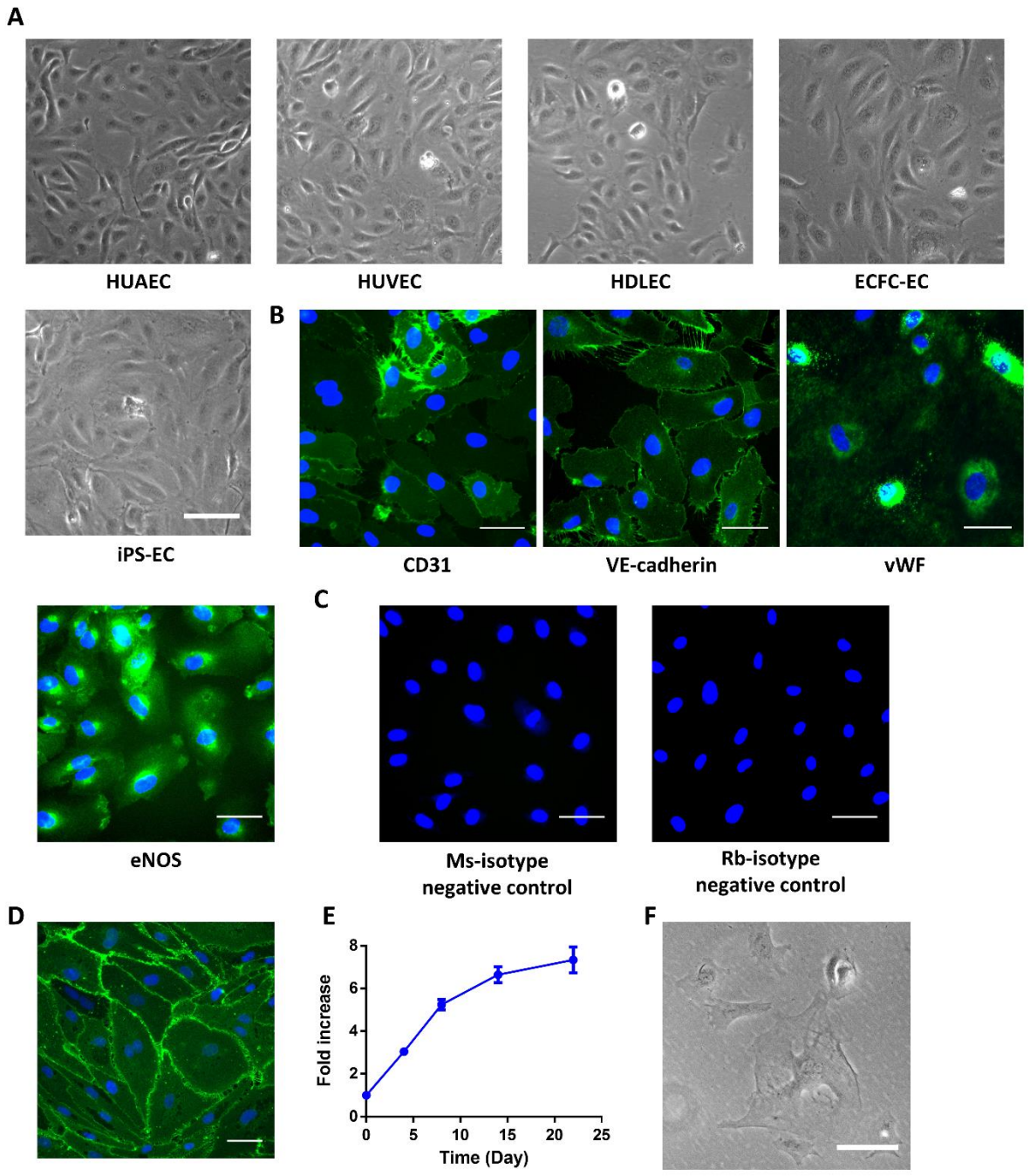

Figure A3.2: Characterization of iPS-ECs. (A) Representative brightfield of primary and iPS-derived endothelia cells. (B) ECFC-ECs were used as positive controls for staining for the endothelial cell markers. Blue = DAPI. (C) Mouse and rabbit IgG isotype control antibodies were used as negative controls for staining the iPS-ECs. (D) iPS-ECs differentiated from the C2A line, stained for CD31 expression. Blue = DAPI. (E) iPS-EC growth curve showing fold increase from Day 8 to Day 30 of differentiation. (F) The iPS-ECs demonstrate a morphological change when cultured in EGM-2 instead of E7V medium. Scale bar: 100 µm (A,F), 50 µm (B,C,D).

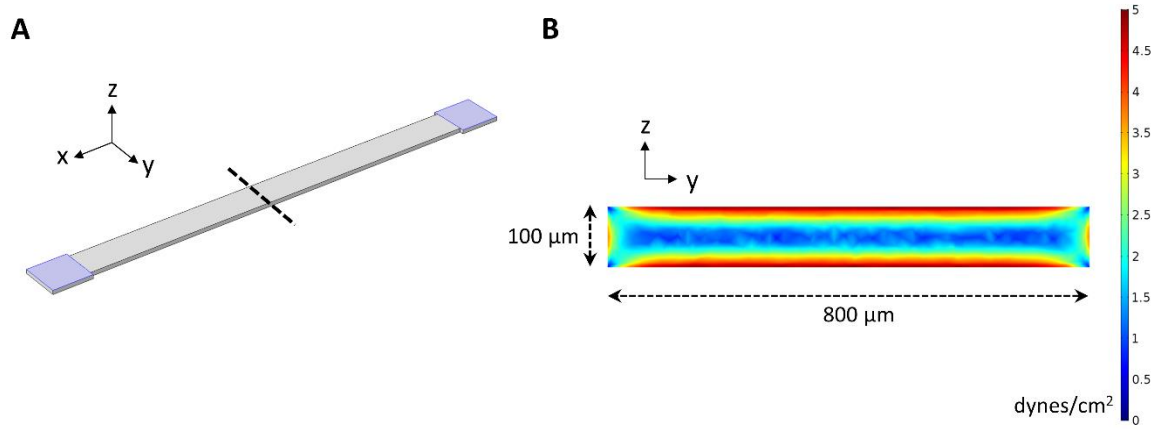

Figure A3.3: COMSOL model of the microfluidic device for the shear stress experiments. (A) The computer aided design (CAD) file used for the microfabrication of the device was imported into COMSOL as an object geometry. (B) The shear stress of the cross-sectional region of the microfluidic device. A near-constant shear stress is experienced across the bottom surface of the device.

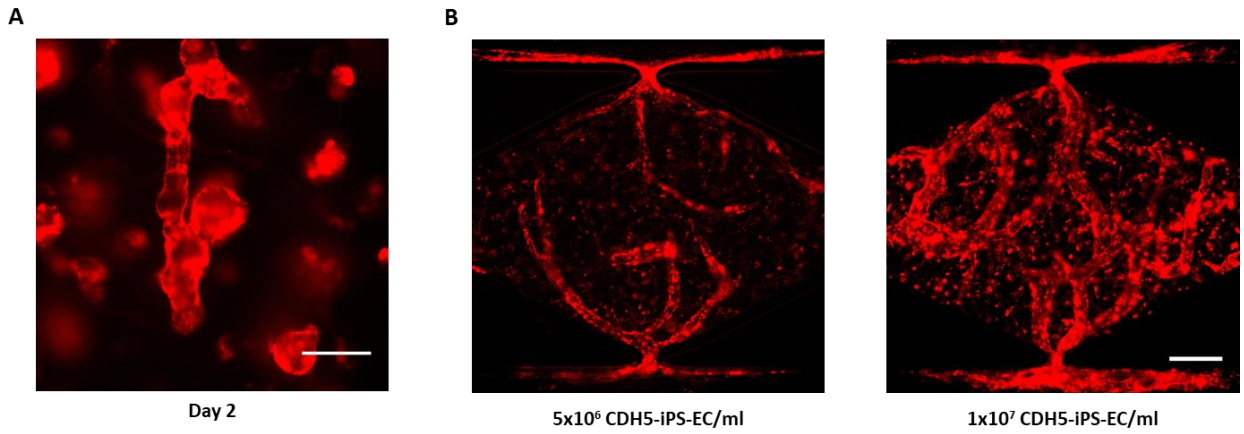

Figure A3.4: CDH5-iPS-EC vasculature formation in the microfluidic platform. (A) Within 48 hours after loading the cells, the iPS-ECs undergo vacuole formation and aggregation into vessel-like structures. (B) At Day 14, the lower cell density ($5x10^6$ cells/ml) loading results in fragmented vessels that do not form a continuous vessel network across the fluidic lines.

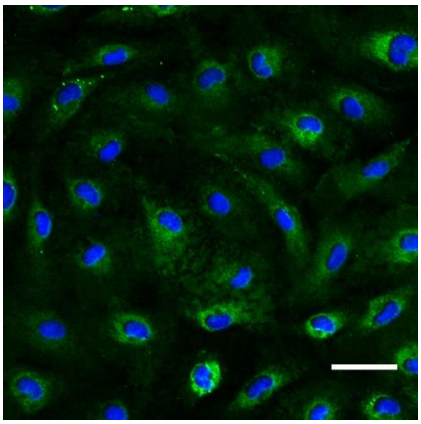

Figure A3.5: Laminin staining of an iPS-EC monolayer. Blue = DAPI. Scale bar: 50 µm.